This is to certify that the

thesis entitled

THE ELECTROMAGNETIC EVALUATION OF A COMPACT
ECR MICROWAVE PLASMA SOURCE

presented by

Mark Alan Perrin

has been accepted towards fulfillment
of the requirements for

M.S. degree in Electrical Engineering

Major professor

Date 8/23/96

THE ELECTROMAGNETIC EVALUATION OF A COMPACT ECR MICROWAVE PLASMA SOURCE

By

Mark Alan Perrin

A THESIS

Submitted to
Michigan State University
in partial fulfillment of the requirements
for the degree of

MASTER OF SCIENCE

Department of Electrical Engineering

1996

ABSTRACT

THE ELECTROMAGNETIC EVALUATION OF A COMPACT ECR MICROWAVE PLASMA SOURCE

By

Mark Alan Perrin

This thesis is a preliminary study of the electromagnetic coupling behavior of a compact cavity coupled ECR plasma source. The plasma source studied in this investigation consists of: a 9.8 cm diameter microwave cavity applicator, a 70 mm diameter quartz discharge chamber, and an eight pole ECR magnet array. The cavity is internally tuned by the adjustment of: 1) a sliding short used to vary cavity length from 4 cm to 12 cm, and 2) an adjustable end feed loop variable from 1.5 cm to 5.5 cm. This source was evaluated with argon at pressures from 0.75 mtorr to 100 mtorr with corresponding flow rates of 20 sccm to 120 sccm. Incident power from a 2.45 GHz magnetron was held constant at 150 Watts.

Reflected power was measured vs. cavity length, loop length, discharge pressure, discharge chamber height and magnetic field in order to construct a parameter map of the electromagnetic modes present in this source and to make observations on mode behavior. Measurements of the impressed relative electric fields at the walls are made to determine the spatial internal electric field patterns and identify each resonant mode. Correlated measurements of absorbed power, ion saturation current, and relative electric field strength are made to determine the relationship between absorbed power and produced charge density.

ACKNOWLEDGEMENTS

The author would like to thank Dr. Jes Asmussen for his direction, instruction, and support throughout the development and execution of this research. Special thanks to Dr. Marvin Siegel for his support and instruction during the early stages of this work. I would also like to thank Dr. D. Reinhard and Dr. T. Grotjohn for their valuable assistance. My colleagues Dr. A. Srivastava, P. Mak, Dr. G. King, and Dr. B. Manring deserve a great deal of thanks for their hours of discussion and training.

This research was supported in part by grants from International Business Machines and the Michigan State University Research Excellence Fund.

TABLE OF CONTENTS

Chapter 4
Electromagnetic Matching Behavior of the Microwave Plasma Source

Chapter 5
Electromagnetic Evaluation of the ECR Microwave Plasma Cavity

Chapter 6
Conclusions and Recommendations

LIST OF TABLES

LIST OF FIGURES

Chapter 2

Chapter 3

Chapter 4

Chapter 5

Chapter 6

Chapter 1

Introduction

1.1 A Brief History of the Microwave ECR Cavity Source:

Although the phenomenon of electron cyclotron resonance in plasmas was utilized as early as the late 1940's [1,2], ECR plasma sources were not widely investigated until the mid 1970's. Early microwave ECR plasma sources [3,4] delivered power to their discharges via rectangular waveguides. A vacuum sealed quartz window separated the waveguide from the discharge. Triple stub tuners were used to match the plasma load and minimize reflected power. Large electromagnet coils were used to produce the ECR regions necessary to couple power into the discharge.

In the early 1980's an ECR plasma source design was developed (by Asmussen, et al.) at Michigan State University [5,6,7,8]. This source, designated as the Microwave Plasma Disk Reactor (MPDR), contained numerous innovations [9,10,11,12,13,14,15] that improved the performance and versatility of the ECR plasma source. Rectangular wave guide, triple stub tuned, microwave excitation was replaced by a resonant cylindrical cavity, tunable with sliding short and coupling probe antenna. This reduced tuning complexity, improved coupling efficiency, and allowed more control over the electromagnetic fields exciting the plasma. The quartz window was replaced by a vacuum fitted quartz dome placed at the bottom of the cylindrical cavity. This quartz dome contained the plasma and improved the coupling of microwave power into the plasma volume. Rare earth permanent magnets were introduced to generate the ECR zone and confine the plasma. This eliminated the need for large, heavy, and power intensive electromagnet coils. What resulted from these innovations was a very efficient, light weight, and controllable ECR source concept that was also versatile in its scaleability and applicability.

Since the mid 1980's the MPDR ECR plasma source has evolved to fit the varied requirements of several specific applications. A few examples are: large diameter wafer etching [16,17], low pressure thin film deposition, molecular beam epitaxy [18], experimental spacecraft propulsion [19], ion sources for low energy materials processing [20], ion implantation, and high energy accelerator physics [21].

1.2 Motivation for Research:

Despite all the applications and uses described above there are still things that are not fully understood about these plasma sources, such as electromagnetic mode behavior and power coupling vs. the experimental variables of tuning, pressure, and input power. The overall motivation for this research is to work toward the answers to some of these questions.

In any careful scientific investigation it is usually best to begin by observing the input/output behavior of the simplest systems possible. The cavity used in this research was designed to excite only the TE_{11} or TM_{01} electromagnetic modes, thus reducing the confusing interactions between many modes that may exist in larger cavities. Knowledge of small diameter source behavior can eventually lead to a greater understanding of the electromagnetics of large diameter microwave discharges.

1.3 Research Goals:

The primary objective of this thesis and the research presented herein is to record and analyze the internal and output behavior of a compact microwave ECR plasma source vs. the many experimental inputs. Input variables varied in these experiments were:

1. Cavity Length, L_s
2. Loop Antenna Length, L_p
3. Discharge Pressure (coupled to Flow Rate), $P / \dot{r}$
4. Input Power (held constant at 150 W), P_{inc}
5. Discharge Chamber Height, h
6. Magnetic Field (presence or absence of Multipole Magnet Ring)

Internal and Output variables investigated and recorded were:

1. Reflected Power, P_{ref}
2. Spatial Variation of Electric Field Strength
3. Relative Electric Field Strength (measured vs. L_s), E_{rel}
4. Ion Saturation Current (used to measure Relative Plasma Density), I_{sat}

One goal in this research was to find the location of the resonant modes vs. the input variables. To this end reflected power was recorded as the experimental input parameters were varied. From this reflected power data a map of the locations of resonant modes was constructed and hence mode behavior vs. the variation of input parameters could be studied. A second goal was to use electric field probe measurements to identify the spatial variation of the impressed electric field and then use electromagnetic theory to identify the resonant modes. The final goal was to investigate the relationship between power absorbed by the plasma source and output charge density produced by the discharge. Overall, the experiments performed in this thesis were intended to contribute to the wider goal common to all those investigating MPDR sources at Michigan State University: a better understanding of the physical mechanisms responsible for the operation of microwave plasma sources and to develop an improved model of source behavior.

1.4 Thesis Outline:

The main parts of this thesis include: a description of the experimental system, a basic theory of operation, a presentation of experimental data, and the conclusions drawn from this research. In Chapter 2 the description of the experimental system is given. This includes a description of the microwave network, the vacuum system, and the plasma source. In Chapter 3 the theoretical background necessary in understanding the basic operation of the plasma source is outlined. Presentation of experimental results begins with Chapter 4 where electromagnetic matching behavior is investigated vs. cavity length, short length, discharge pressure, discharge chamber height, and magnetic field. This data is then used to map the parameter location of matched resonant modes and study their behavior as each of the inputs are varied. In Chapter 5 electric field patterns are measured and used to identify, wherever possible, each of the resonant modes found in Chapter 4. Chapter 5 also includes experimental measurements that relate the power absorbed by the plasma source to relative measurements of plasma charge density and internal electric field strength. In Chapter 6 the conclusions drawn from the experimental data are summarized and suggestions for future research are presented.

Chapter 2

Description of the Experimental System

2.1 Introduction:

The plasma source described in this work is considered a compact plasma source of the type specifically designed for ion beam generation or molecular beam epitaxy applications. It has a 9.8 cm diameter cavity and 7 cm diameter discharge.

This thesis is a continuation of work done in part by L. Mahoney [20] in characterizing the performance of a small ECR plasma source. This design differs from that used by Mahoney in that the cavity is excited by an end feed loop antenna instead of a side feed probe. The microwave cavity end feed component of this source was originally designed by L. Mahoney while he was employed at IBM Watson Research Center. It was then donated to MSU for this research by Dr. S. J. Whitehair from IBM Watson Research Center. The other working components including ECR magnets and baseplate were designed and built by the author combining the best features of existing base plate designs.

The experimental system (see Figure 2.1) used in this research is described in the sections below. First in sections 2.2 and 2.3 the support systems including the microwave delivery system (1) and the gas/vacuum system (2) are described. Then the ECR microwave plasma source (3) and its components are described in detail in section 2.4.

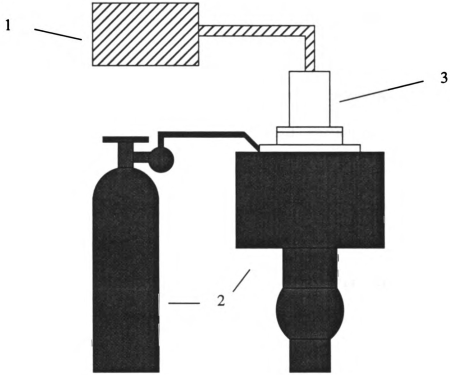

1) Microwave Delivery System
2) Gas/Vacuum System
3) ECR Microwave Plasma Source

Figure 2.1 - Block Diagram of The Experimental System

2.2 The Microwave Delivery System:

The microwave power supply for this system is a 2.45 GHz magnetron source (see Figure 2.2) made by MicroNow, Inc. (1) with a maximum CW power output of 300 Watts. Attached to the power supply is a coaxial microwave circuit that is used to: deliver power to the plasma source, allow power measurement, and to protect the MicroNow source from power reflected back into the magnetron.

Forward traveling microwave power is guided from the magnetron source through ports A and B of the circulator (2) and on through a 30 dB directional coupler (3) that samples forward power for measurement. Power is then guided through a coaxial cable (4) to the cavity applicator (5). The cavity applicator applies microwave power to the plasma load. When the cavity applicator is perfectly matched to the transmission circuit all forward power is absorbed in the cavity and plasma. If the cavity applicator is not matched, some microwave power is reflected back through the coaxial cable and directional coupler to the circulator. Reflected power will then flow from port B to C of the circulator and on through a 20 dB directional coupler (6) that samples reflected power. Power then travels through a second coaxial cable (7) and is dissipated in a matched 50 Ω, 500 Watt dummy-load (8). Since the dummy load is matched to the transmission system only a small and harmless amount of power is reflected back through ports C to A of the circulator and back into the power source.

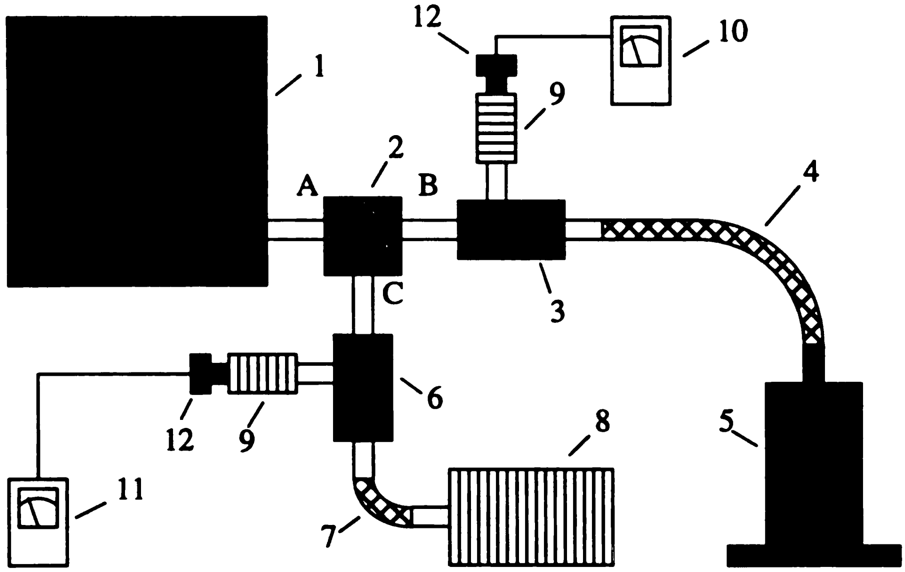

1) 2.45 GHz Microwave Power Supply
2) Three Port Circulator
3) 30 dB Directional Coupler
4) 50 Ω Coaxial Cable
5) Cavity Applicator
6) 20 dB Directional Coupler
7) 50 Ω Coaxial Cable
8) 500 Watt Dummy Load
9) 20 dB Attenuator
10) HP Power Meter (Forward Power)
11) HP Power Meter (Reflected Power)
12) Thermistor Power Detectors

Figure 2.2 - Block Diagram of Microwave Circuit

Each directional coupler is fitted with a 20 dB attenuator (9) giving a total attenuation of 50 dB for sampled forward power (30 dB directional coupler + 20 dB attenuator) and a 40 dB attenuation for sampled reflected power. Forward and reflected power measurements are made by two analog Hewlett-Packard power meters (10 & 11) fitted with thermistor power detectors(12).

2.3 Gas Flow and Vacuum System:

Argon gas used in the vacuum system (Figure 2.3) flows from a pressurized tank (1) through a polyvinyl tube (2) to an MKS digital flow controller (3). This controller regulates the flow of Argon and has a maximum flow rate of 120 sccm. Argon flows from here through a stainless steel tube (4) to the baseplate of the plasma source (5). There it flows into an annular channel and escapes into the discharge zone through eight 1/64" diameter gas inlets that are equally spaced around the circular opening at the bottom of the baseplate.

The plasma source sits on top of a 100 liter stainless steel vacuum chamber (6). Pressures in the chamber are measured by three different pressure gauges: a thermocouple gauge (7) which measures pressures above 100 mtorr, an MKS 1 Torr rated baratron gauge (8) which measures pressures from 0.1 mtorr to 100 mtorr, and an ion gauge (9) which measures pressures from 0.001 mtorr to 1 mtorr.

Gas is removed from the system by a 10 inch diameter diffusion pump (10) with a rating of 2500 l/s. The diffusion pump is aided by a 33 m^3/hr roughing pump (11). Both the roughing pump and the diffusion pump are water cooled.

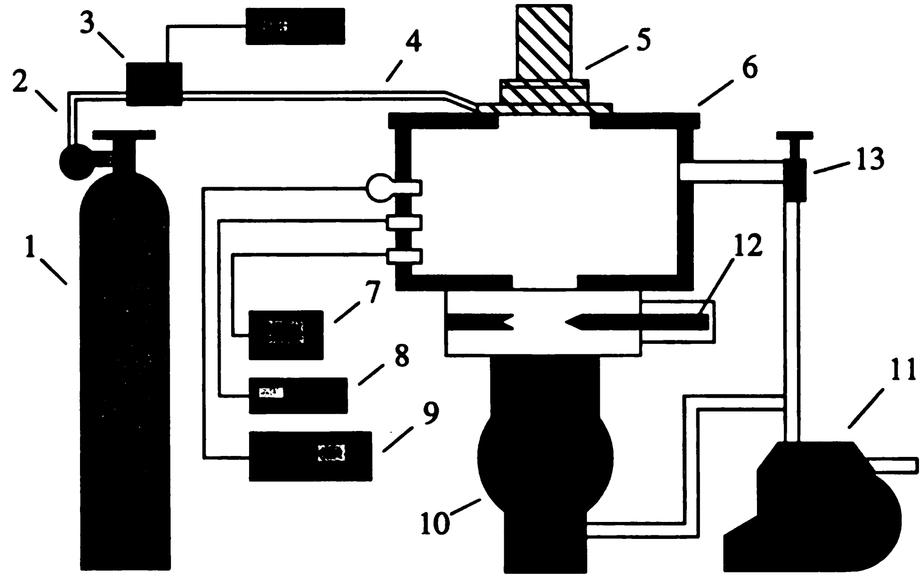

1) Argon Tank
2) Polyvinyl Tube
3) MKS Digital Flow Controller
4) Stainless Steel Tubing
5) Plasma Source
6) Stainless Steel Vacuum Chamber
7) Thermocouple Guage
8) Baratron Guage
9) Ion Guage
10) Diffusion Pump
11) Roughing Pump
12) Pneumatic Shutter Valve
13) Manual Flow Valve

Figure 2.3 - Block Diagram of Gas Flow and Vacuum System

A high vacuum pneumatic shutter valve (12) is installed over the diffusion pump. This valve is closed when the system is exposed to pressures above 100 mtorr. A manual flow valve (13) is located between the roughing pump and the chamber. This valve is open while the roughing pump is the primary pump evacuating the chamber from pressures of 1 atmosphere to 50 mtorr, and then it is closed while the diffusion pump is in operation.

When the system is initially evacuated the roughing pump is used to pump the system down to 50 mtorr. At that pressure the manual flow valve (13) is closed and the pneumatic gate valve (12) is opened to allow the diffusion pump to evacuate gas from the chamber. The diffusion pump then takes the system down to a base pressure of 10^{-6} Torr. Experimental pressures in the system range from 10^{-4} to 10^{-1} Torr. This corresponds to argon gas flow rates of 27.5 sccm to 120 sccm. Since there is no throttle valve in this system the pressure and flow rates are interdependent.

2.4 The Microwave Plasma Source:

The plasma source consists of: a microwave cavity applicator, a discharge chamber, a base plate, and a set of ECR permanent magnets. A complete diagram of the assembled source is shown in Figure 2.4. Photographs of the assembled source and disassembled source are shown in Figures 2.5, 2.6, and 2.7. Sections 2.4.1, 2.4.2, and 2.4.3 describe the components of the source in detail.

There are certain features shown in the photographs that must be identified here. In Figure 2.5 the curved tube attached to the stainless steel base plate is the input inlet for the discharge gas. The curved brass tube attached to the brass cooling stage is one of the inlets for compressed air. The other air inlet can be partially seen on the other side of the brass stage near the ruler. The barbed inlet and outlet tubes for cooling water are seen near the curved air inlet tube on the brass cooling stage. Note the holes machined vertically and horizontally on the stainless steel cavity for electric field measurement. A disassembled view of the source is shown in Figure 2.6 including: stainless steel base plate, cavity, quartz discharge chamber, and brass cooling stage. In Figure 2.7 the brass end plate is shown along with a bottom view of the cavity exposing the loop antenna. A view of the stainless steel base plate showing guide bolts and discharge chamber is also seen.

1) Stainless Steel Cylindrical Shell
2) Sliding Short
3) Contact Fingers
4) Brass End Plate
5) End Feed Loop Antenna
6) Coaxial Cable
7) Outer Coaxial Conductor
8) Outer Coaxial Contact Fingers
9) Coaxial Center Conductor
10) Plate to Antenna Contact Fingers
11) Screened Window
12) E-Field Measurement Holes
13) Brass Water/Air Cooling Stage
14) Water Channel
15) ECR Magnet Ring
16) Air Channel
17) Air Cooling Holes
18) Stainless Steel Base Plate
19) 8cm Vitan O-Ring
20) 20cm Vitan O-Ring
21) Discharge Gas Channel
22) Gas Inlet Holes
23) Quartz Discharge Chamber
24) Plasma Discharge
25) ECR Zone (shown in fig. 2.10)
26) Outer Soft Iron Keeper
27) Bottom Soft Iron Keeper

Figure 2.4 - Cross-Section of the ECR Plasma Source (# Key)

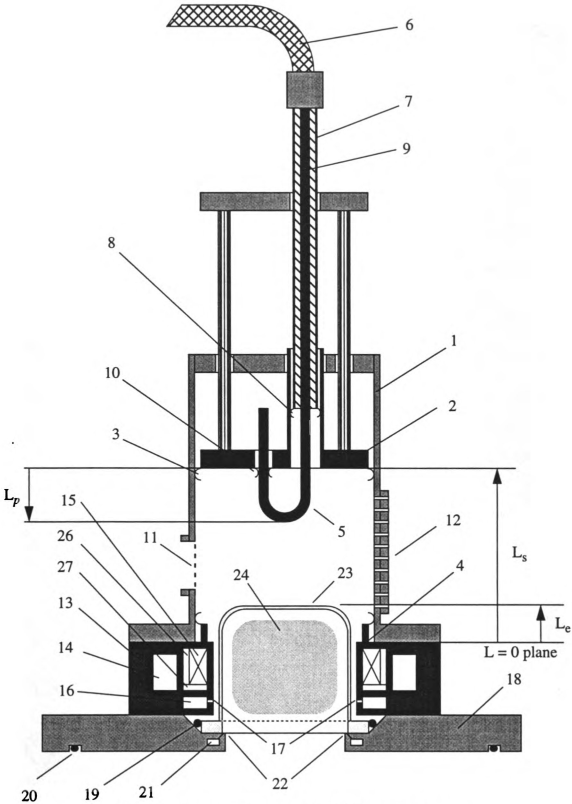

Figure 2.4 - Cross-Section of the ECR Plasma Source

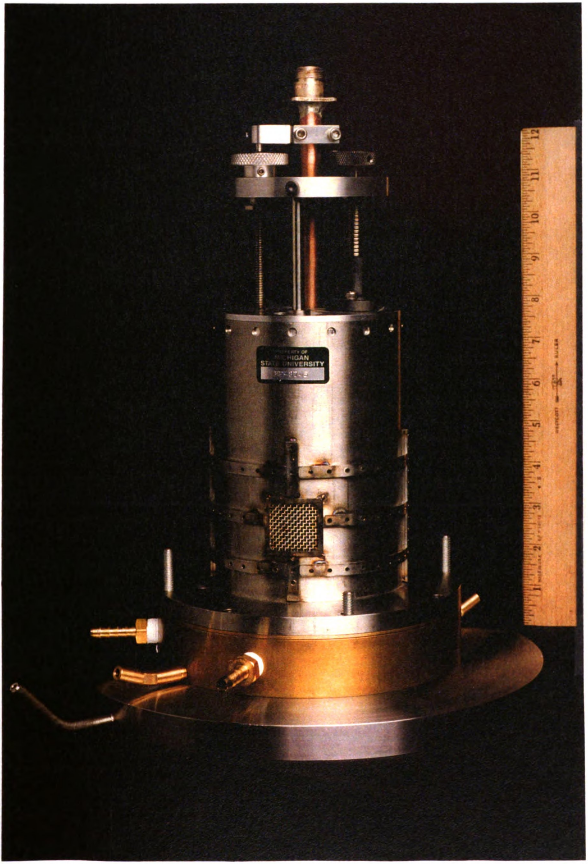

Figure 2.5 - Assembled Microwave ECR Plasma Source

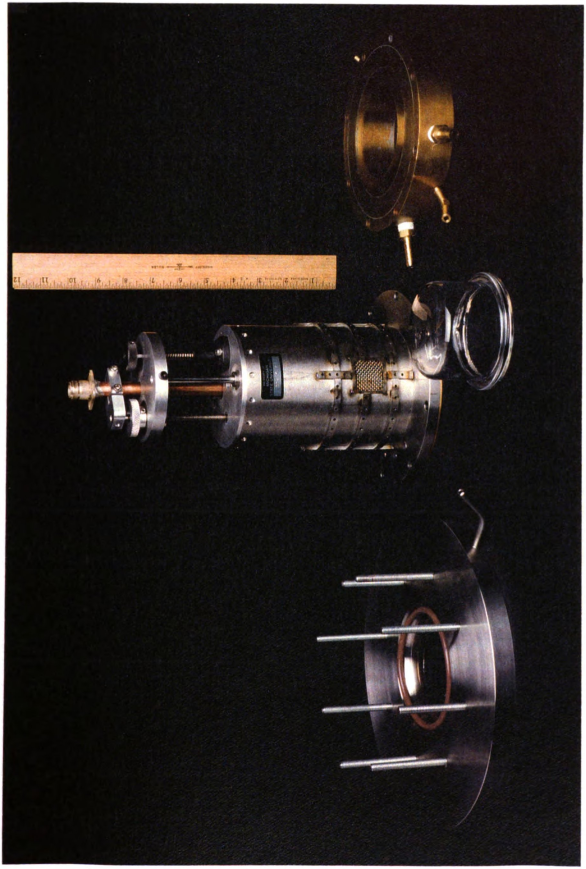

Figure 2.6 - Disassembled Microwave ECR Plasma Source

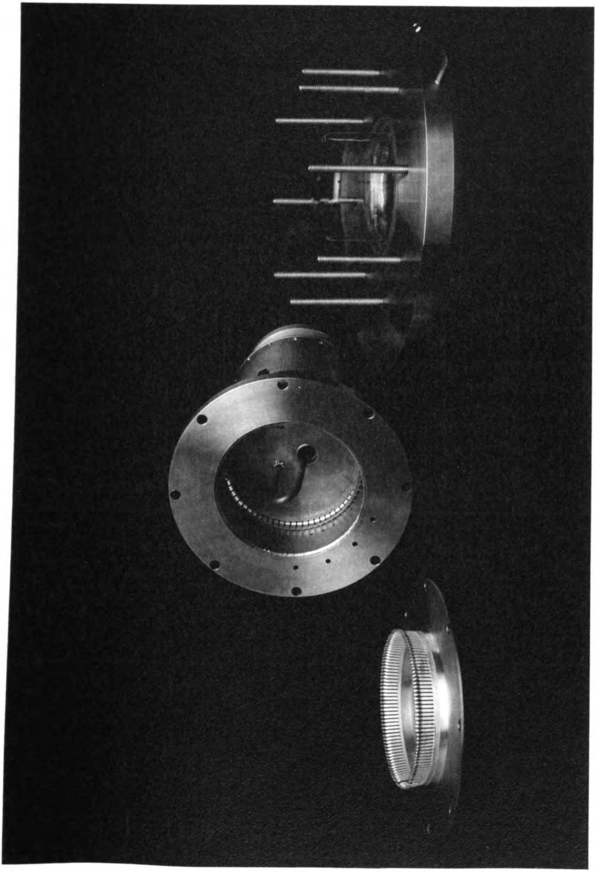

Figure 2.7 - Veiw of brass end plate, Loop antenna, and guide bolts

2.4.1 The Microwave Cavity Applicator:

The microwave applicator (Figure 2.8) consists of a stainless steel cylindrical shell (1) 9.8 cm in diameter. It is bounded at the top by a sliding short (2) with flexible contact fingers (3) that maintain constant electrical contact with the cavity wall. At the bottom it is bounded by a stationary brass end plate (4) with contact fingers. The bottom end plate has a 3 inch diameter hole in it's center where the quartz bell jar (23) extends up into the cavity (see Figure 2.4). The length, L_s, of the cylindrical cavity can be varied from 5 cm to 13 cm by adjusting the movable sliding short (2).

Power is delivered to the cavity with an adjustable length end feed loop antenna (5) that extends through the sliding short. The loop is adjustable, in that, the height of the loop antenna (L_p) can be varied from 1.5 cm to 5.5 cm. The loop is made from 3/16 inch copper rod bent to form a loop with a 0.5 inch radius. Electromagnetic power is delivered to the antenna through a coaxial cable (6). The outer coaxial conductor (7) maintains electrical contact with the sliding short through a set of contact fingers (8), and the center conductor (9) extends out into the cavity and loops back to make contact with the sliding short through another set of contact fingers (10), thus forming the loop antenna (5).

An adjustable sliding short and a moveable loop provide two degrees of freedom to tune the cavity to a specific resonant mode and minimize reflected power.

The cylindrical shell has a one square inch screened window (11) near the bottom of the cavity for viewing of the plasma and to allow for ventilation of the compressed air that cools the quartz bell jar. There are 148 holes each 3mm in diameter (12) drilled into the wall of the cavity in a grid like pattern to allow measurement of the internal electric fields.

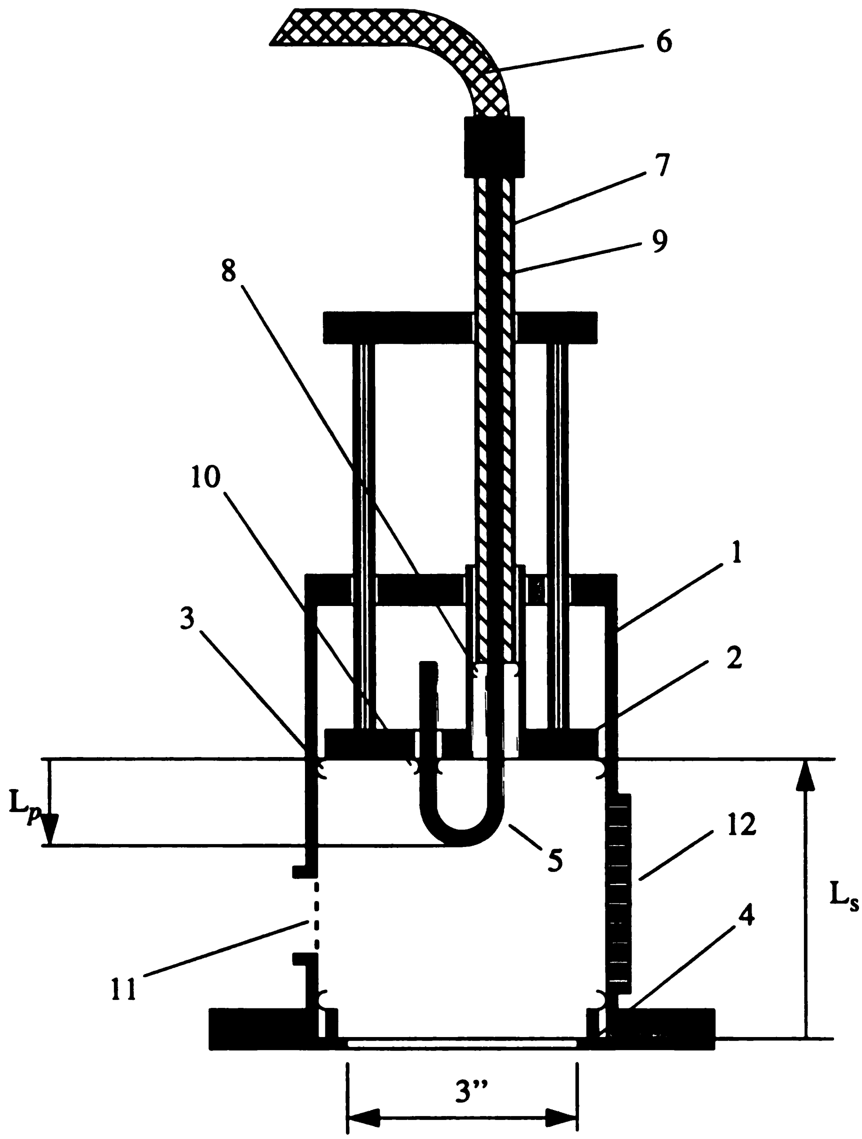

1) Stainless Steel Cylindrical Shell
2) Sliding Short
3) Contact Fingers
4) Stationary Brass End Plate
5) End Feed Loop Antenna
6) Coaxial Cable
7) Outer Coaxial Conductor
8) Outer Coaxial Contact Fingers
9) Center Conductor
10) Plate to Antenna Contact Fingers
11) Screened Window
12) E-Field Sampling Holes

Figure 2.8 - Cross Section of Microwave Cavity Applicator

It is important to note that neither the screened window nor the holes permit microwaves to leak from the cavity, primarily because their dimension is much smaller than the 12.24 cm wavelength of the 2.45 GHz radiation.

2.4.2 Two Stage Base Plate and Quartz Discharge Chamber:

The microwave cavity sits on top of a 6.5" diameter 1.25" tall brass stage (Figure 2.9) (13) responsible for air and water cooling. This stage also contains the ECR magnets(15).

Cold water circulates through an annular ring channel (14) and conducts away heat generated by the discharge. The water channel surrounds the compartment that contains

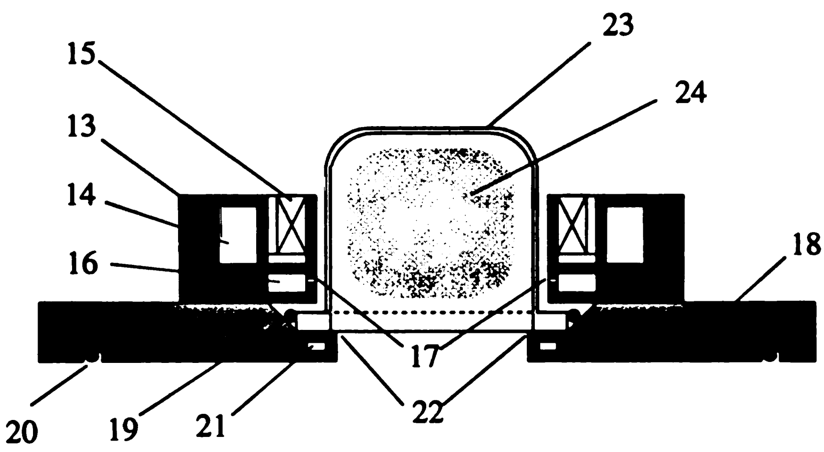

13) Brass Water/Air Cooling Stage	19) 8cm Vitan O-Ring
14) Water Channel	20) 20cm Vitan O-Ring
15) ECR Magnet Ring	21) Discharge Gas Channel
16) Air Channel	22) Gas Inlet Holes
17) Air Cooling Holes	23) Quartz Discharge Chamber
18) Stainless Steel Base Plate	24) Plasma Discharge

Figure 2.9 - Cross Section of Base Plate and Discharge Chamber

the ECR magnets (15). It is necessary to keep excessive heat from the magnets which must not be exposed to temperatures above 100 degrees C.

Compressed air is delivered through two brass pipes on opposite sides of the stage (See Figure 2.5, air pipe is shown below and in the center of two water barbs). Air flows through two radial channels to an annular ring channel (16) near the bottom of the brass stage. Air is forced across the outer surface of the bell jar through eight 1/64" diameter holes (17) that are evenly spaced at 45 degree angles around the inner wall of the brass stage. This compressed air cools the bell jar by convection and is then forced out of the system through the screen window of the microwave cavity (11).

Below the brass air/water cooling stage sits a stainless steel base plate (18) that supports the quartz bell jar (23). Eight 1/4" bolts are attached to, and extend up from the base plate (See Figure 2.7). These bolts serve as guideposts for the microwave cavity and brass cooling stage, allowing the system to be assembled or disassembled quickly. The base plate contains two vacuum sealing groves that contain o-rings. The first grove surrounds the bell jar flange where an 8 cm diameter Vitan o-ring (19) is wedged between the diagonal grove and the outer diameter of the flange. The second grove is on the bottom of the plate and contains a 19 cm diameter Vitan o-ring (20) that forms a seal between the base plate and the processing chamber.

Argon gas is delivered through a radial channel to an annular ring (21) near the bottom of the base plate and then escapes into the discharge through eight 1/64" diameter holes (22). These holes are angled so that the incoming gas is directed toward the center of the bell jar.

A quartz bell jar (23), that contains the plasma discharge (24), is attached to the center of the base plate. The bell jar sits above a 2.5 inch diameter hole in the center of base plate (18) that allows the plasma to diffuse into the processing chamber below. Two bell jars of different height 2.2 inch (5.6 cm) and 2.7 inch (6.9 cm), were used in the experimental evaluation of this system. The distance denoted by L_e in Figure 2.4 is the distance the bell jar extends into the microwave cavity above the $L_s = 0$ plane. The 5.6 cm quartz bell jar has $L_e = 1.4$ cm, and the 6.9 cm bell jar has an $L_e = 2.7$ cm. The distance between the bell jar and the loop antenna can be calculated by subtracting L_e and L_p from L_s.

2.4.3 The ECR Magnet Configuration:

Powerful rare earth permanent magnets (Figure 2.10) (15) are placed around the discharge to facilitate electron cyclotron resonance in the plasma. Eight alternating pole arc-magnets are assembled in a solid ring around the midsection of the discharge chamber (23). The magnets are made of a Neodymium-Iron-Boron alloy and exhibit a magnetic energy product of 42 Mega Gauss-Oersted. Measured with a Gaussmeter the pole face strength of these magnets is 4 KiloGauss (when placed in the soft iron keeper) and the 875 Gauss ECR zone (25) lies approximately 1 cm away from the face of the magnets. The magnets are glued together with metal bonding epoxy (loctite 324) and also glued to a soft iron keeper (26) that surrounds the ring magnet structure. The soft iron keeper confines the stray magnetic fields on the outside of the arc-magnet ring. This serves to increase the field strength and pushes the ECR zone farther away from the quartz walls and into the discharge. The magnets also sit on a second soft iron keeper (27) that prevents excessive magnetic flux from extending into to processing chamber below the discharge.

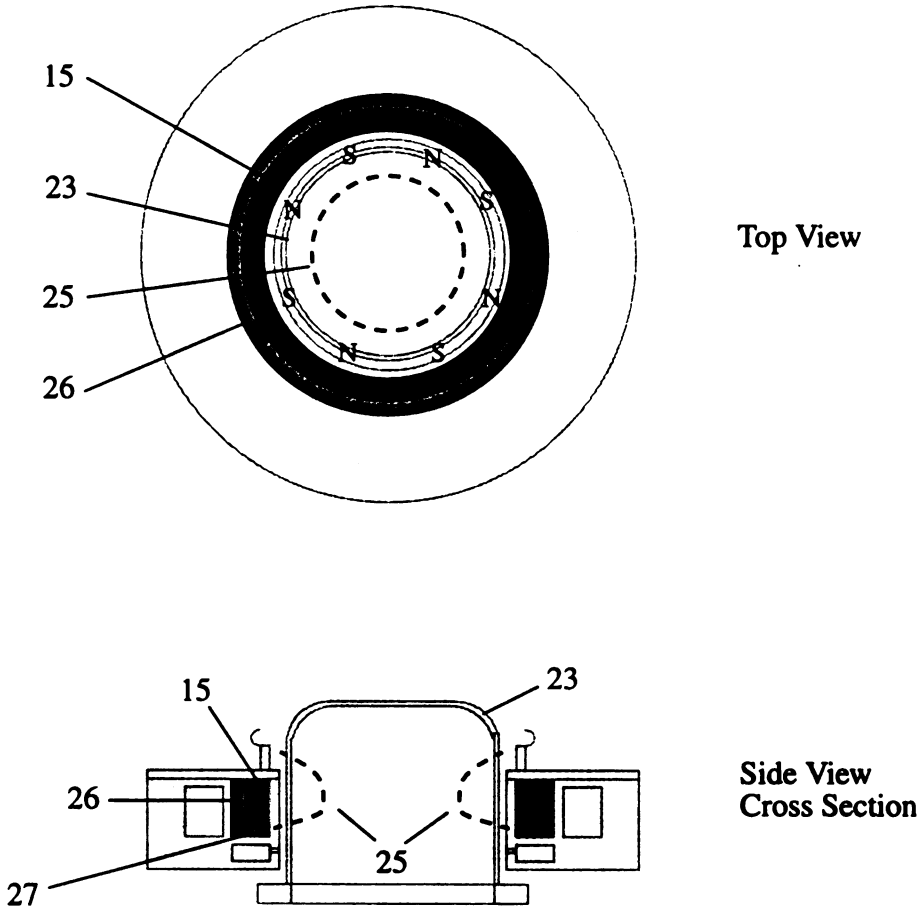

15) ECR Magnet Ring
23) Quartz Discharge Chamber
25) ECR Zone
26) Outer Soft Iron Keeper
27) Bottom Soft Iron Keeper

Figure 2.10 - ECR Magnet Configuration

Chapter 3

Theory of Operation For A Microwave Excited Cavity Plasma Source

3.1 Introduction:

The use of a single mode resonant microwave cavity to focus microwaves into a plasma discharge has many advantages.

1) The input impedance of the plasma cavity system can be matched to the microwave delivery circuit by tuning the cavity. When the cavity is matched all power incident to the cavity is absorbed and no power is reflected back into the delivery circuit.

2) The tuning of a resonant cavity with a movable sliding short and coupling probe or loop requires the optimization of only two variables. Other methods such as triple stub tuning require the optimization of three variables.

3) Coaxial loop or probe coupling allows the use of coaxial transmission line as a method of power delivery reducing the system size and cost and increasing flexibility of placement.

4) In other methods of load matching tuning elements may be many half wavelengths away from the plasma load. In contrast, the resonant mode field structure in a microwave cavity is usually only one half wavelength long: reducing wall losses, concentrating stored energy, and reducing the size of the reactor.

5) The quality factor Q of a microwave cavity can be very high, making possible very large internal field magnitudes capable of maintaining high density plasmas at very low discharge pressures even though the input power may be modest.

6) The use of single-mode excitation instead of multi-mode excitation allows spatial control of the electric fields exciting a plasma load.

7) It is possible to create cavities with a variety of tunable resonant modes each having different spatial field structures.

This Chapter includes a theoretical development of: transmission line load matching, electromagnetic propagation in waveguides, eigenlengths and field structures of standing wave cavity modes.

3.2 Transmission Line Load Matching:

A transmission line section with length l and characteristic impedance Z_0, shown in Figure 3.1, is terminated by a complex load impedance $Z_{in} = R + jX$. This load impedance can be representative of any lumped circuit of complex impedance, a microwave cavity, or the characteristic impedance of another attached transmission line section of infinite

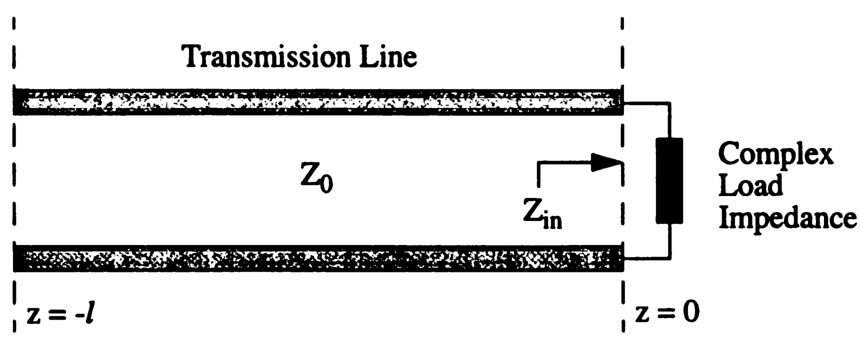

Figure 3.1 - Transmission line section with complex load

length. The time average power delivered to the this complex load is given by:

$$P_t = P_i\left(\frac{Z_0}{Z_{in}}\right)\left(\frac{2Z_{in}}{Z_{in}+Z_0}\right)^2 \qquad \text{Eq. 3.1}$$

where P_t is the power transmitted to the load, P_i is the power incident on the z = 0 plane interface, Z_{in} is the input impedance at z = 0, and Z_0 is the characteristic impedance of the transmission line. Similarly, the time average reflected power is given by:

$$P_r = P_i\left(\frac{Z_{in}-Z_0}{Z_{in}+Z_0}\right)^2 \qquad \text{Eq. 3.2}$$

where P_r is power reflected from the z = 0 plane interface. It can be seen that if $Z_{in} = Z_0$ then $P_t = P_i$ and $P_r = 0$. Therefore, if the cavity applicator shown in Figure 3.2(a) has an input impedance Z_{in} that is matched to the transmission line characteristic impedance Z_0 all power incident on this interface will be absorbed by the cavity and no power will be reflected back through the transmission line toward the microwave generator.

3.3 Complex input impedance and equivalent lumped parameter circuit:

The complex input impedance of the plasma loaded cavity system can be given as:

$$Z_{in} = \frac{P_t + j2\omega(W_m - W_e)}{\frac{1}{2}|I_0|^2} = R_{in} + jX_{in} \qquad \text{Eq. 3.3}$$

where P_t is total time average power coupled into the cavity, ω is the radian microwave excitation frequency, W_m and W_e are time average stored magnetic and electric energy, and $|I_0|$ is the magnitude of the current on the coupling loop. Since Z_{in} is complex it can be resolved into a real resistive part R_{in} and an imaginary reactive part jX_{in}. The complex impedance of the plasma cavity system can be varied by the movement of the sliding short or coupling loop, both shown in Figure 3.2(a). Generally, movement of the sliding short will change the imaginary or reactive part of the complex impedance and moving the coupling loop will change the real or resistive value. Under resonant conditions W_m and W_e will be equal, making $X_{in} = 0$. Yet, the cavity will not be matched unless the value of I_0, controlled by the position of the coupling loop, is such that it produces an R_{in} equal to Z_0.

Another way to understand the concept of cavity matching is by physical analogy with a parallel RLC circuit. If only one resonant cavity mode is considered it is then possible to model the plasma cavity system as a parallel RLC circuit shown in Figure 3.2(b). All elements drawn with a diagonal arrow indicate that they are variable. The complex phasor impedance of this circuit is given in terms of it's lumped component values as:

$$Z_{in} = Z_0 m^2 \left(jX + \frac{1}{\frac{1}{j\omega L_c} + j\omega C_c + G_c + jB_P + G_P} \right) \qquad \text{Eq. 3.4}$$

where Z_0 is the characteristic impedance of input transmission line, m is the number of turns on the generator side of the ideal transformer, jX is the equivalent reactance of the coupling loop, L_c and C_c are the equivalent inductance and capacitance of the microwave cavity, G_c is an equivalent conductance arising from ohmic losses in the metallic cavity walls, jB_p is the equivalent admittance of the plasma load, and G_P is an equivalent conductance arising from losses in the plasma load.

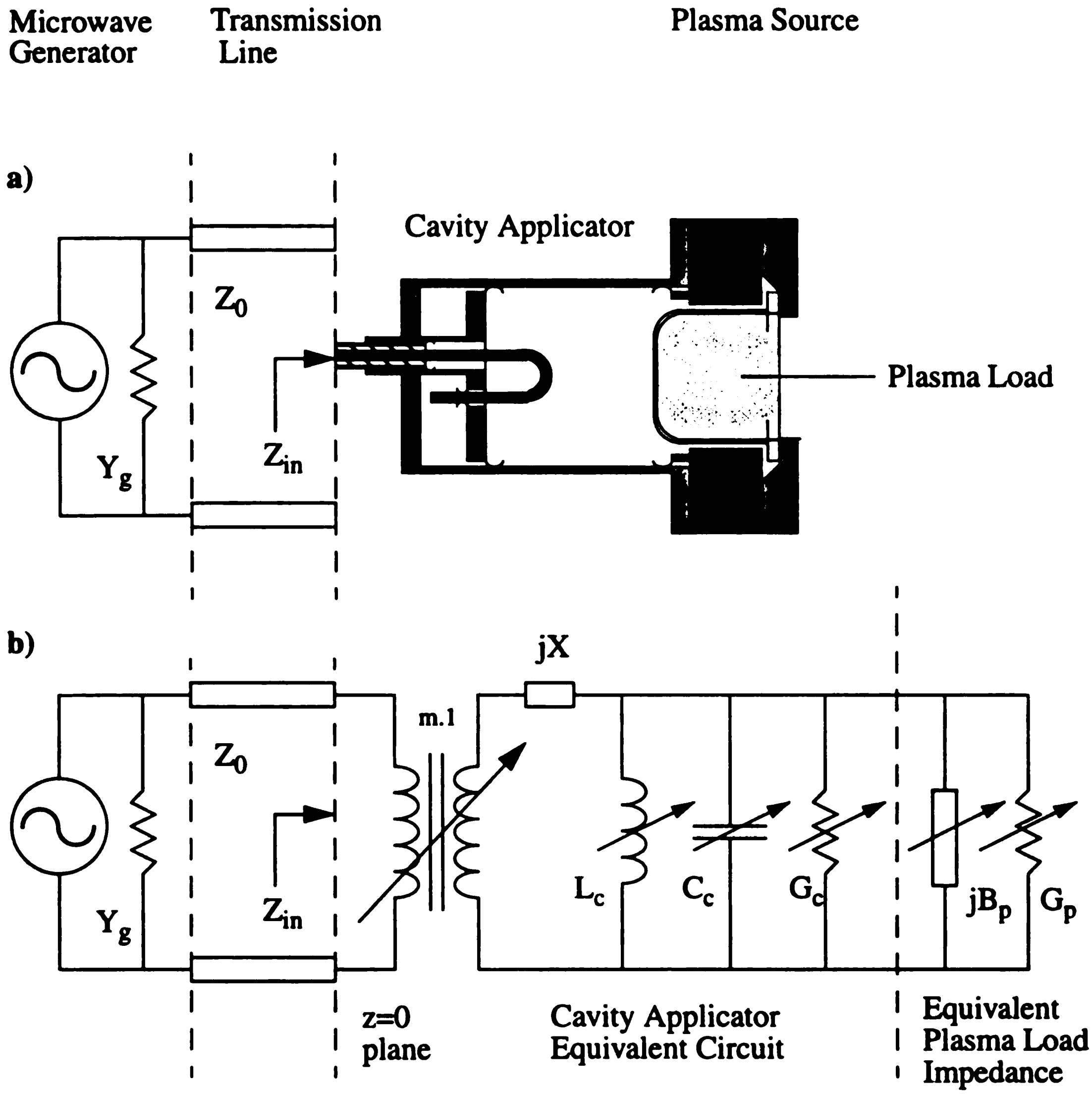

Y_g - Microwave Generator Source Admittance

Z_0 - Intrinsic impedance of the transmission line

Z_{in} - Input impedance to the microwave cavity at the z=0 plane

jX - Reactance of coupling element (loop antenna or transformer)

L_c, C_c, G_c - Lumped parameter elements of the microwave cavity

jB_p, G_p - Lumped parameter elements of the plasma load

Figure 3.2 - (a) Plasma loaded microwave cavity with transmission circuit, (b)Lumped parameter equivalent circuit of the cavity for a single resonant mode.

3.4 Frequency Response and Length Tuning:

RLC circuits and microwave cavities are examples of resonant systems analogous to spring-mass oscillators. All resonant systems have: a natural oscillatory frequency or frequencies, the ability to absorb and store energy, an energy damping mechanism, and a quality factor Q. When excited by a driving force that oscillates near it's resonant frequency, a resonant system absorbs energy. A curve plotting power transferred to the resonant system as a function of driving frequency is shown in figure 3.3(a). Note that when the resonant system is driven at exactly the resonant frequency ω_0 the power transferred to the system is equal to P_{inc} the total incident power. All power in the driving force is then absorbed by the resonant system. This corresponds to the situation where a microwave cavity is matched to its transmission system. Alternately, if the driving frequency is held constant and the parameters of the system are varied, i.e. short length for a microwave cavity or LC for an RLC circuit, there is an optimum parameter point (short length) where the power transferred to the system is equal to P_{inc}. This is shown in Figure 3.3(b).

3.5 Transient Response and Quality Factor Q:

Even when the power delivered by the driving force is small, if the driving force is at or near the resonant frequency, a very large amount of energy can accumulate in the resonant system until a steady state equilibrium is reached with the damping mechanism. This can be shown in the transient response of a parallel RLC circuit, shown in Figure 3.4. At time t_0 the sinusoidal current source with magnitude I_0 begins delivering power to the

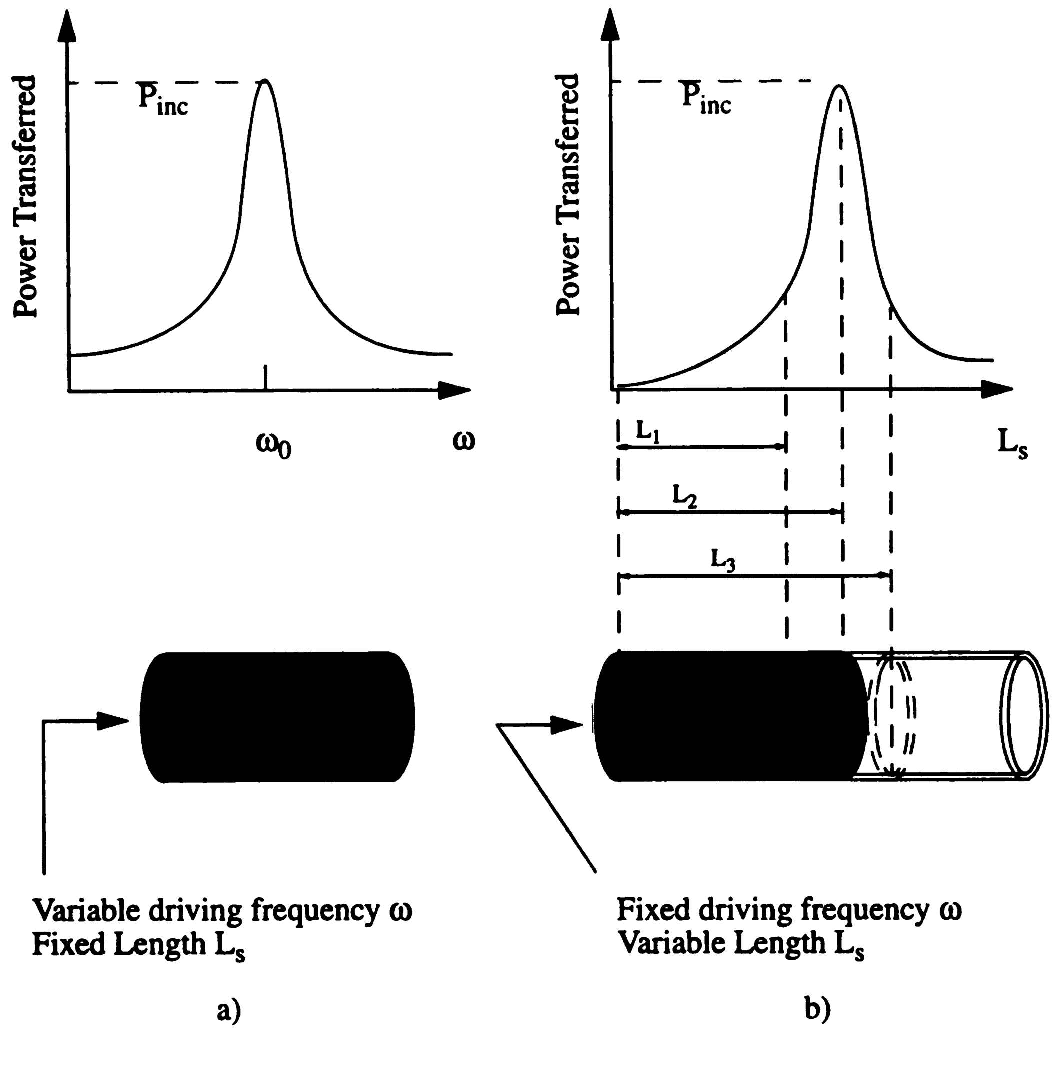

Figure 3.3 - (a) power absorbed vs. driving frequency ω, (b) power absorbed vs. cavity length L_s (Variation in L_s is exaggerated for clarity)

RLC circuit. Between time t_0 and t_1 energy is absorbed by the inductor capacitor system and the amplitude of current flowing in the LC subcircuit increases, shown as I_L in Figure 3.4. As time progresses the magnitude of current oscillating in the LC subcircuit approaches a steady state equilibrium where the power dissipated in the resistor equals the time average power delivered to the circuit by the current source. The magnitude of the steady state current in the inductor is a factor Q times the magnitude of current from the current source I_0. Therefore if the quality factor Q of the circuit is large then the magnitude of inductor current and stored energy will also be large. (In a microwave cavity this high stored energy translates to large internal electric and magnetic fields.) If at time t_2 the current source is shut off then no further power is delivered to the circuit. The stored energy is then dissipated in the resistor and exponentially decays to zero. The transient response of a microwave cavity or any resonant system is physically analogous to the transient response of the parallel RLC circuit just described. The plasma cavity differs from a spring-mass oscillator or an RLC circuit in that it has many degrees of freedom and therefore many possible resonances.

Note that the rise time and decay time of stored energy in the circuit, a microwave cavity, or any resonant system is also related to the quality factor Q. A time constant for the decay of stored energy can be given as:

$$\tau = \frac{2}{\omega_0 Q} \qquad \text{Eq. 3.5}$$

where ω_0 is the resonant frequency of the resonant system. Two important relations defining the quality factor of a resonant system are given as:

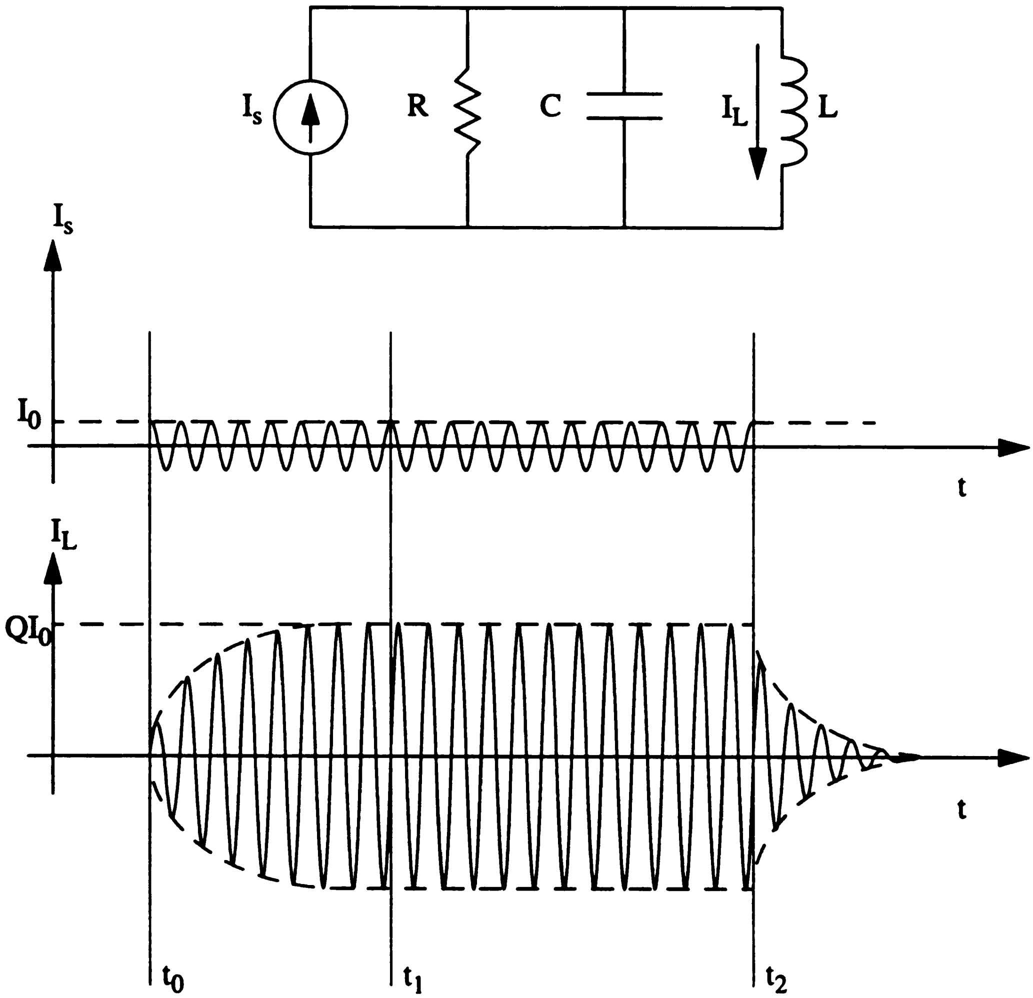

$$I_s = I_0 \cos(\omega_0 t) \qquad \text{for} \quad t_0 \le t < t_2$$

$$I_L = QI_0\left(1 - \exp\left(-\frac{1}{2}\omega_0 Q t\right)\right)\sin(\omega t) \qquad \text{for} \quad t_0 \le t < t_1 \quad \text{where} \quad t_1 \gg \frac{2}{\omega_0 Q}$$

$$I_L = QI_0 \sin(\omega_0 t) \qquad \text{for} \quad t_1 \le t < t_2$$

$$I_L = QI_0 \exp\left(-\frac{1}{2}\omega_0 Q t\right)\sin(\omega t) \qquad \text{for} \quad t_2 \le t < \infty$$

$Q = \dfrac{R}{\omega_0 L}$ where Q is the quality factor of the RLC circuit

Figure 3.4 - Transient Response of a Parallel RLC Circuit

$$Q = \frac{\omega_0 W_s}{P_{lost}} = \frac{\omega_0}{\Delta\omega} \qquad \text{Eq. 3.6}$$

where W_s is the time-average energy stored in the resonator at resonance, P_{lost} is the time-average power loss, and $\Delta\omega$ is the half power bandwidth of the resonant system.

3.6 Electromagnetic Wave Behavior:

3.6.1 Electromagnetic Wave Propagation in Cylindrical Waveguides:

Electromagnetic waves propagate within enclosed conducting waveguide structures with one of three mechanisms: 1) transverse electromagnetic, 2) transverse electric, and 3) transverse magnetic.

3.6.1.1 TEM propagation in coaxial waveguide sections:

Enclosed cylindrical waveguides with a coaxial center conductor, like regions I and II of the plasma source, support transverse electromagnetic (TEM) waves as their fundamental mode of propagation. TEM waves are so named because both the electric and magnetic fields are both transverse to the direction of propagation. TEM waves propagate along air filled coaxial waveguides with the same wavelength and velocity as free space TEM plane waves. Therefore, the wavelength of radiation in coaxial waveguide sections is determined by the simple relation: $\lambda = u/f$ where u is the speed of light in the dielectric medium filling the waveguide and f is the frequency of the propagated wave. Given the 2.45 GHz excitation frequency of the plasma source the wavelength of TEM propagation in each coaxial section is 12.24 cm. The phase relationship and field pattern of a coaxial TEM wave is shown for a general coaxial waveguide in Figure 3.5a.

Transverse electric (TE) and transverse magnetic (TM) modes of propagation, discussed in the next section, may also exist in a coaxial waveguide, but only if the distance between the center and outer conductor is greater than the order of one half wavelength [22]. If this distance is less than one half wavelength the TE and TM modes are non-propagating or evanescent. TEM waves do not propagate in cylindrical waveguide sections without a center conductor.

3.6.1.2 TE and TM propagation in hollow cylindrical waveguide sections:

In waveguides without a center conductor, such as section III of the plasma source, the only electromagnetic modes of propagation are Transverse Electric (TE) or Transverse Magnetic (TM). TE waves have no electric field components in the direction of propagation (i.e. electric fields are confined to the transverse plane) while TM waves have no magnetic field components in the direction of propagation.

Propagation of a TE or TM wave mode in a waveguide is only possible if the frequency of electromagnetic excitation exceeds the cutoff frequency associated with that mode at the given waveguide radius. The cutoff frequencies [23] for given TM and TE modes in a waveguide with radius *a* are given:

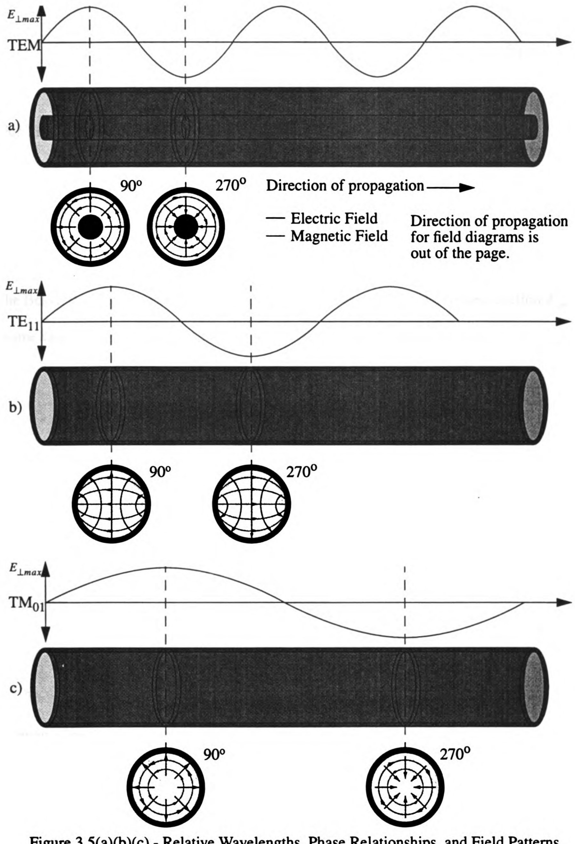

Figure 3.5(a)(b)(c) - Relative Wavelengths, Phase Relationships, and Field Patterns

For TM_{nm} modes:

$$f_c = \frac{x_{nm}}{a2\pi\sqrt{\mu\varepsilon}} \qquad \text{Eq. 3.7}$$

For TE_{nm} modes:

$$f_c = \frac{x'_{nm}}{a2\pi\sqrt{\mu\varepsilon}} \qquad \text{Eq. 3.8}$$

where μ and ε are the permeability and permittivity of free space, x_{nm} is the *m*th root of the Bessel function J_n, and x'_{nm} is the *m*th root of the derivative of the Bessel function J'_n. Some values of the Bessel function are given below:

Table 3.1 - Selected roots of the Bessel Funciton

Roots of $J_n(x)$	Roots of $J'_n(x)$
$x_{01} = 2.405$	$x'_{01} = 3.832$
$x_{02} = 5.520$	$x'_{02} = 7.016$
$x_{11} = 3.832$	$x'_{11} = 1.814$
$x_{12} = 7.016$	$x'_{12} = 5.331$

The waveguide in section III of the plasma source had a radius *a* of 4.9 cm and the frequency of excitation was 2.45 GHz. Therefore, the only modes that may propagate in this waveguide are the TE_{11} with a cutoff frequency of 1.794 GHz and the TM_{01} with a cutoff frequency of 2.343 GHz. All other roots of the Bessel function except x_{01} and x'_{11} give cutoff frequencies that exceed 2.45 GHz and hence do not propagate in this waveguide.

The guide wavelength λ_g is given as:

$$\lambda_g = \frac{\left(\frac{c}{f}\right)}{\sqrt{1 - \left(\frac{f_c}{f}\right)^2}} \qquad \text{Eq. 3.9}$$

where f_c is the cutoff frequency of the TE or TM waveguide mode, f is the excitation frequency, and c is the free space velocity of light. Note that the guided wavelength for any excitation frequency is longer than the free space wavelength at that frequency.

For the TE_{11} mode in section III of the plasma source the guided wavelength is 17.98 cm. Similarly, the guided wavelength for a TM_{01} mode is 41.89 cm. The field patterns and relative wavelengths of the TE_{11} and TM_{01} guided modes for a general waveguide of radius of 4.9 cm and 2.45 GHz excitation are shown in Figure 3.5(b) and (c).

3.6.2 Abrupt Waveguide Discontinuities:

It is important to consider abrupt discontinuities in transmission systems, because they have a significant effect on wave propagation where they occur. Wave propagation across a discontinuity may result in: 1) the wave being split into forward and reflected components, 2) the generation of higher order propagating modes that may be reflected and transmitted from the discontinuity, 3) the generation of higher order evanescent modes that reactively store energy in the vicinity of the discontinuity, or 4) the change in mode of waveguide propagation (i.e. from TEM to TE or TM).

In such a case where the geometry of the waveguide has changed, but the dielectric medium filling both waveguides is the same, we can assume that there is a change in the geometry of the electric and magnetic fields from one section of waveguide to the next. However, the field magnitudes must not change abruptly (discontinuously) at a point in space, so even though there may be an abrupt discontinuity in the geometry of the waveguide the total modal field geometry must make a smooth transition from one waveguide section to the next. This is made possible by the Fourier summation of higher order evanescent (non-propagating) modes in the vicinity of the discontinuity.

Therefore, the electric field in the region of waveguide just before the discontinuity arises from the summation of fields from: 1) the propagating forward wave(s), 2) propagating reflected waves, and 3) reflected evanescent modes.

Similarly, the electric field in the region of waveguide just following the discontinuity arises from the summation of: 1) propagating transmitted waves, and 2) transmitted evanescent modes. The generation of, reflected or transmitted, propagating or evanescent, modes is determined by the geometry of the discontinuity. The magnitudes of these generated modes are determined by the boundary conditions at the discontinuity.

A diagram illustrating a waveguide discontinuity is shown in Figure 3.6. In the coaxial waveguide section the mode of propagation is assumed to be TEM with all coaxial TE or TM modes assumed to be in cutoff. In the hollow waveguide section TE_{11} and TM_{01} modes are assumed to propagate while all higher order TE and TM modes are assumed to be in cutoff. Figure 3.6(a) depicts propagating wave modes while Figure 3.6(b) depicts the spatially decaying evanescent modes in the vicinity of the discontinuity. Physically evanescent modes act as reactive energy storage elements such as capacitors or inductors.

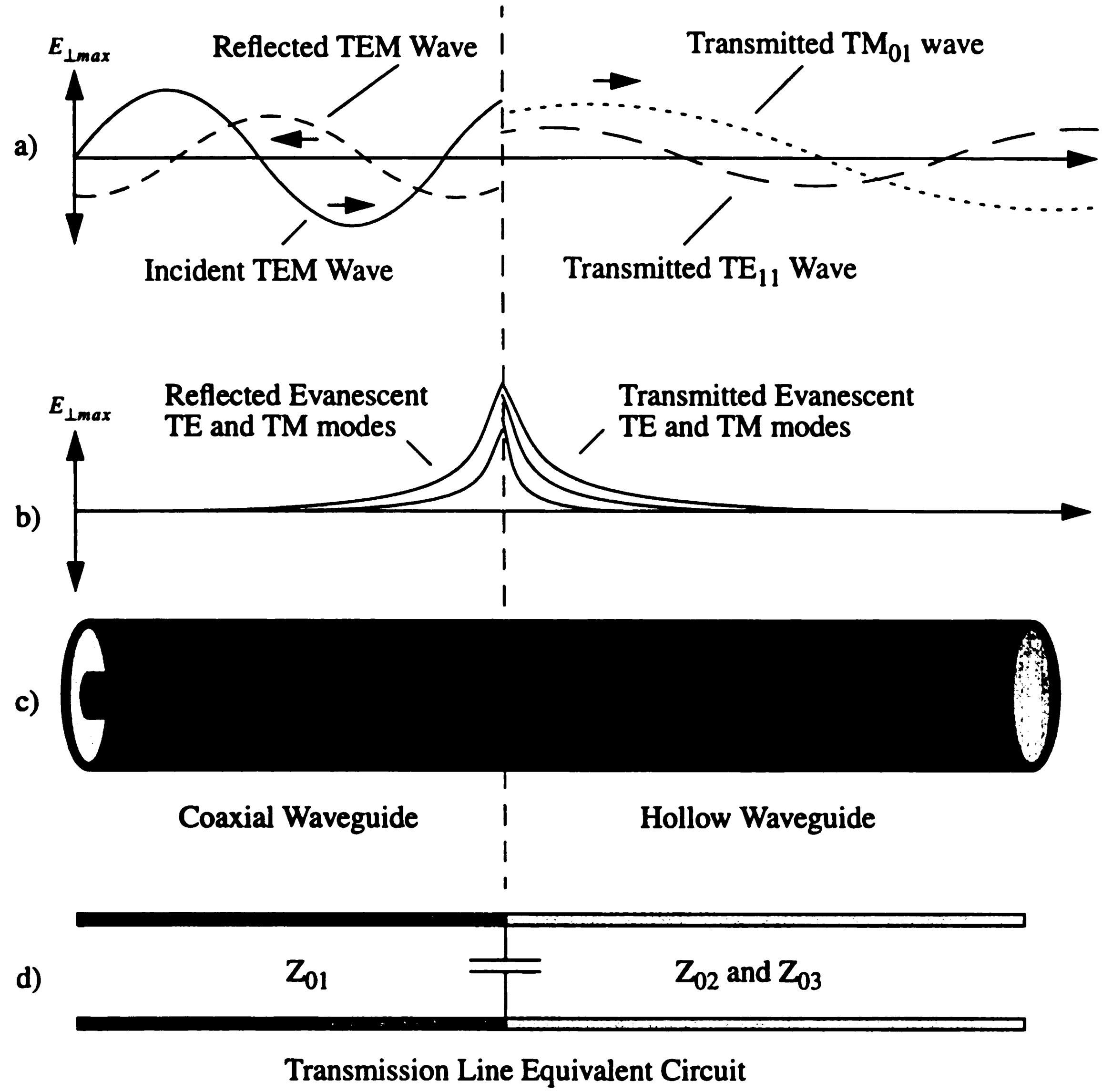

Z_{01} - characteristic impedance of TEM propagation in the coaxial waveguide

Z_{02} - characteristic impedance of TE_{11} propagation in the hollow waveguide

Z_{03} - characteristic impedance of TM_{01} propagation in the hollow waveguide

Figure 3.6 - Wave behavior at an abrupt waveguide discontinuity

Thus, a transmission line equivalent circuit, shown in Figure 3.6(d), can be defined for this waveguide system, where the capacitor represents the effect of evanescent modes.

3.7 Standing Wave Cavities and Cavity Modes:

With the information provided in the previous section it is now possible to introduce the concept of a standing wave cavity. If one end of the waveguide is covered with a conducting end plate then the incident wave, shown traveling to the right in Figure 3.7, is reflected producing a reflected wave that travels in the opposite direction. A standing wave is produced in front of the conducting end plate by the interference of incident and reflected waves. If both ends of the waveguide are covered with a conducting end plate and he length of the waveguide is some integer multiple of $\lambda_g/2$, where λ_g is the guide wavelength, then a standing wave can be maintained in this section of waveguide as shown in figure 3.7. This is commonly called a standing wave cavity.

To obtain a set of vector equations describing the time harmonic electric and magnetic fields inside the cavity volume it is standard procedure to use the Helmholtz equation and solve the boundary value problem for the boundary conditions. For a perfectly conducting cylindrical cavity with radius a, length L_s the parallel component of the electric field must be zero at the boundary. From the separation constant equations for TM and TE modes we can determine the resonant frequency for any mode given any cavity length L_s.

For TM_{nml} modes:

$$(f)_{nml} = \frac{1}{2\pi a\sqrt{\mu\varepsilon}}\sqrt{x_{nm}^2 + \left(\frac{l\pi a}{L_s}\right)^2} \qquad \text{Eq. 3.10}$$

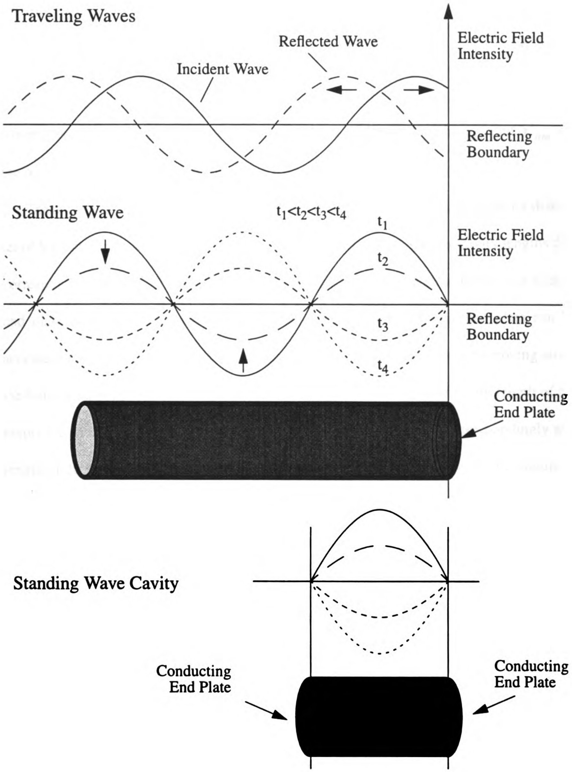

Figure 3.7 Standing Waves and Standing Wave Cavity

For TE_{nml} modes:

$$(f)_{nml} = \frac{1}{2\pi a\sqrt{\mu\varepsilon}}\sqrt{(x'_{nm})^2 + \left(\frac{l\pi a}{L_s}\right)^2} \qquad \text{Eq. 3.11}$$

where a is the radius of the circular waveguide, L_s is the cavity length, x_{nm}, and x'_{nm} are the roots of the Bessel function (see Table 3.1).

These frequency vs. cavity length curves are plotted, in Figure 3.8, for a cavity diameter of 9.8 cm. For a cavity excited at a fixed frequency there are specific cavity lengths that correspond to specific TE and TM resonant modes. If a cavity with a movable or sliding end plate is used then all modes within the maximum length of the end plate can be accessed. For a fixed excitation frequency of 2.45 GHz. this corresponds to moving along the horizontal constant frequency line shown in Figure 3.8. When the cavity length of the empty cavity is tuned to 8.99 cm the TE_{111} mode can be accessed, correspondingly at a length of 20.95 cm the TM_{011} mode can be accessed. Note however that, the maximum of length for the cavity applicator of the plasma source is 14 cm, so the TM_{011} resonant mode is not accessible.

Waveguides with larger diameter can propagate many more than two modes at a frequency of 2.45 GHz and therefore a larger diameter cavity can support a larger number of resonant modes. A mode chart for a cavity with 6 in. diameter is shown in figure 3.9. Different modes can be accessed with a constant cavity length if the frequency is changed, as shown on the vertical constant length line (10 cm) in Figure 3.9. In order to use this type of mode selection a variable frequency microwave source must be used.

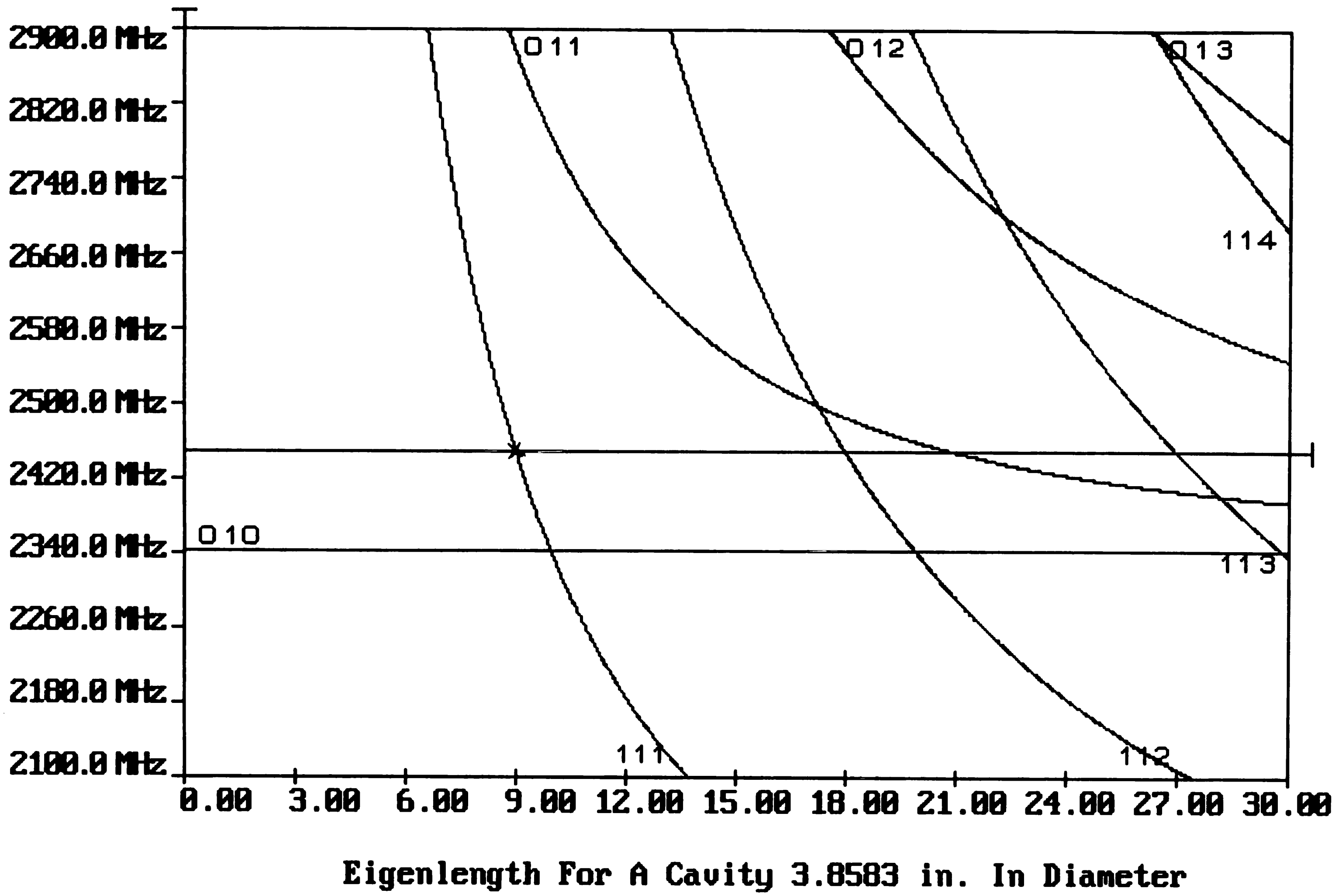

Figure 3.8 - Mode Chart for Standing Wave Cavity with 9.8 cm Diameter

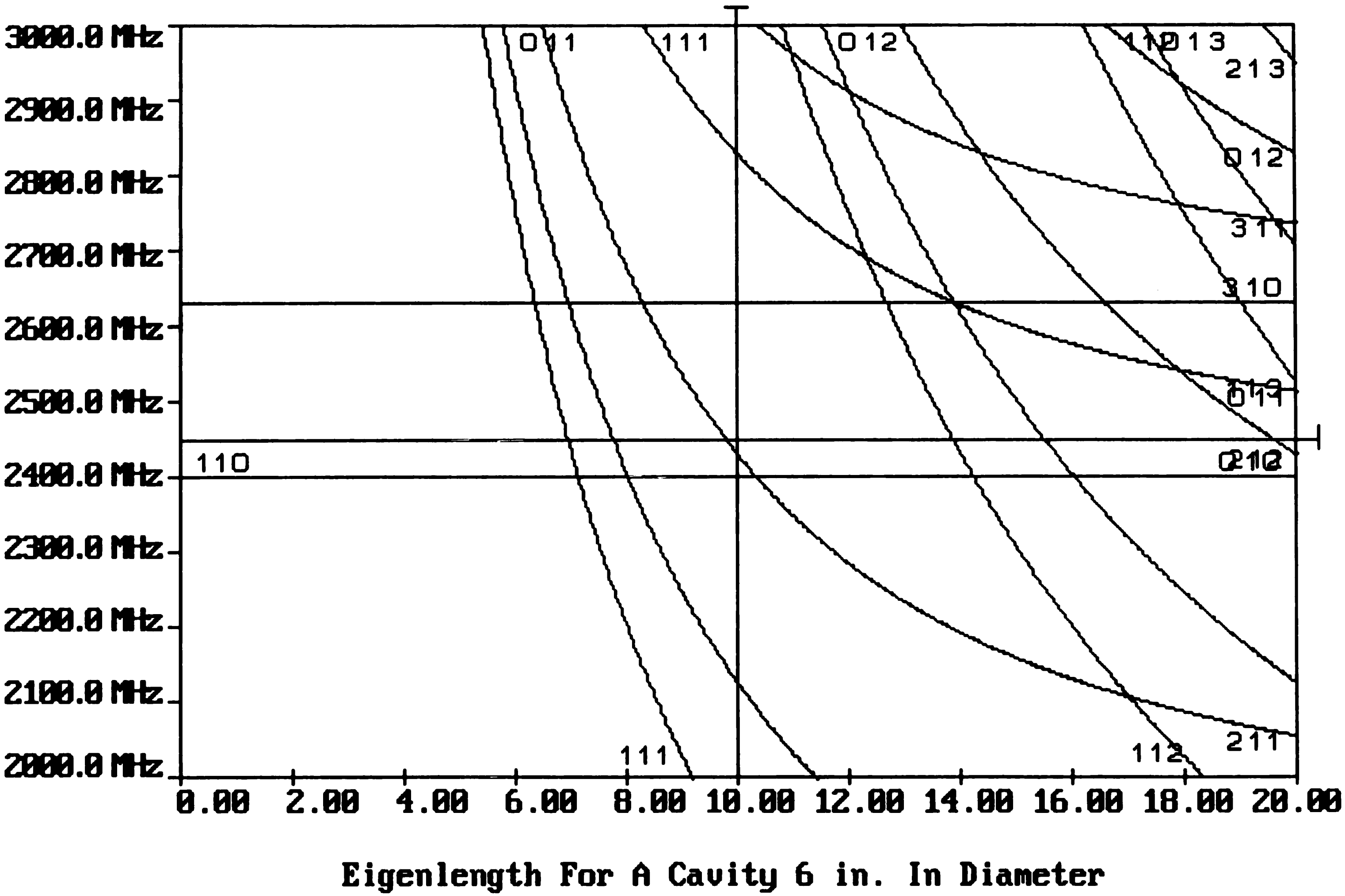

Figure 3.9 - Mode Chart for Standing Wave Cavity with 6 in. Diameter

From the solution of the Helmholtz equation the phasor magnitudes for fields in the cylindrical cavity can be given:

TE_{nml} Field Solutions for a Cylindrical Cavity:

$$E_r = j\omega\mu A\left[\frac{n}{r}\right]J_n\left(\frac{x'_{nm}}{a}r\right)\sin(n\theta)\sin\left(\frac{l\pi}{L_s}z\right) \quad \text{Eq. 3.12}$$

$$E_\theta = j\omega\mu A\left[\frac{x'_{nm}}{a}\right]J'_n\left(\frac{x'_{nm}}{a}r\right)\cos(n\theta)\sin\left(\frac{l\pi}{L_s}z\right) \quad \text{Eq. 3.13}$$

$$H_r = A\left[\frac{l\pi}{L_s}\right]\left[\frac{x'_{nm}}{a}\right]J'_n\left(\frac{x'_{nm}}{a}r\right)\cos(n\theta)\cos\left(\frac{l\pi}{L_s}z\right) \quad \text{Eq. 3.14}$$

$$H_\theta = (-A)\left[\frac{l\pi}{L_s}\right]\left[\frac{n}{r}\right]J_n\left(\frac{x'_{nm}}{a}r\right)\sin(n\theta)\cos\left(\frac{l\pi}{L_s}z\right) \quad \text{Eq. 3.15}$$

$$H_z = A\left[k^2-\left(\frac{l\pi}{L_s}\right)^2\right]J_n\left(\frac{x'_{nm}}{a}r\right)\cos(n\theta)\sin\left(\frac{l\pi}{L_s}z\right) \quad \text{Eq. 3.16}$$

TM_{nml} Field Solutions for a Cylindrical Cavity:

$$E_r = (-B)\left[\frac{l\pi}{L_s}\right]\left[\frac{x_{nm}}{a}\right]J'_n\left(\frac{x_{nm}}{a}r\right)\cos(n\theta)\sin\left(\frac{l\pi}{L_s}z\right) \quad \text{Eq. 3.17}$$

$$E_\theta = B\left[\frac{l\pi}{L_s}\right]\left[\frac{n}{r}\right]J_n\left(\frac{x_{nm}}{a}r\right)\sin(n\theta)\sin\left(\frac{l\pi}{L_s}z\right) \quad \text{Eq. 3.18}$$

$$E_z = B\left[k^2-\left(\frac{l\pi}{L_s}\right)^2\right]J_n\left(\frac{x_{nm}}{a}r\right)\cos(n\theta)\cos\left(\frac{l\pi}{L_s}z\right) \quad \text{Eq. 3.19}$$

$$H_r = -j\omega\varepsilon B\left[\frac{n}{r}\right]J_n\left(\frac{x_{nm}}{a}r\right)\sin(n\theta)\cos\left(\frac{l\pi}{L_s}z\right) \quad \text{Eq. 3.20}$$

$$H_\theta = -j\omega\varepsilon B\left[\frac{x_{nm}}{a}\right]J'_n\left(\frac{x_{nm}}{a}r\right)\cos(n\theta)\cos\left(\frac{l\pi}{L_s}z\right) \quad \text{Eq. 3.21}$$

where A and B are constants, r is the distance from the central axis, z is longitudinal distance, and k is the wavenumber. The spacial pattern of fields for the TE_{111} and TM_{011} modes are illustrated in Figure 3.10 (a) and (b).

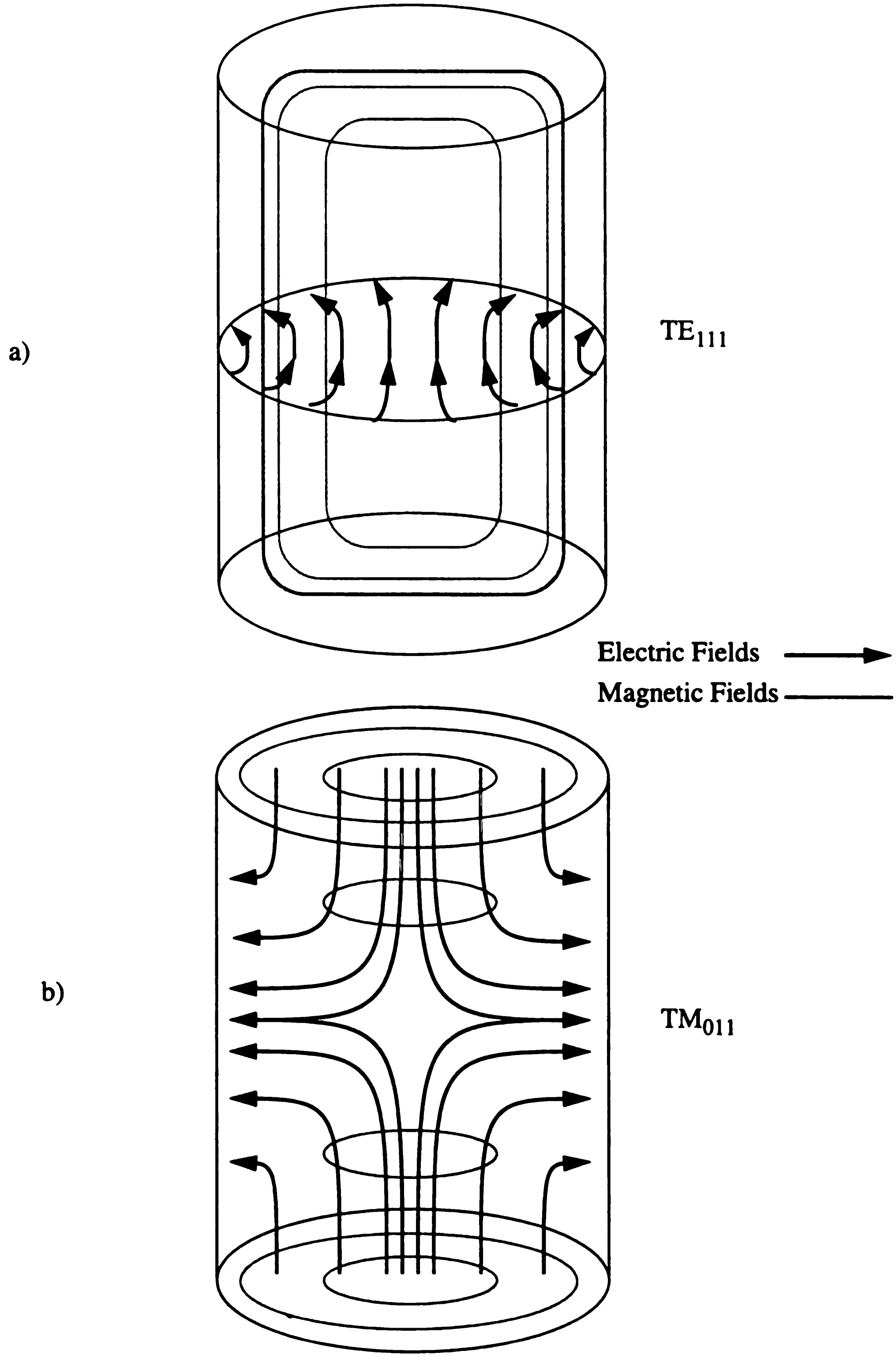

Figure 3.10 - Field Patterns for TE_{111} and TM_{011} Resonant Modes (at 90° of Cycle)

3.9 Conclusion:

The main advantages of cavity coupled plasma sources are that they are: 1) easily matched to the microwave network, 2) capable of concentrating stored energy and maintaining high internal fields, 3) capable of minimizing wall losses, and 4) tunable to a variety of different resonant modes with different spatial field characteristics. At the beginning of this chapter the importance of matching the complex load of the plasma source to the microwave network was explained. Then the frequency response, quality factor, and transient response of resonant systems was illustrated. Finally, the electromagnetic wave behavior of cylindrical waveguides and standing wave cavities was explained in detail in order to provide an understanding of internal electromagnetic behavior of the plasma source and to lay the ground work for a transmission line model that will be presented in Chapter 6.

Chapter 4

Electromagnetic Matching Behavior of the Microwave Plasma Source

4.1 Introduction:

The experimental investigation presented in this Chapter has two purposes: 1) provide an operational guide or parameter map that shows where to tune the source for best microwave match given parameters such as discharge gas, pressure, and forward input power, and 2) to develop a physical understanding of the plasma cavity system by correlating observed source behavior with electromagnetic and plasma theory.

In order to investigate the electromagnetic tuning behavior of the plasma source and determine the best cavity length and loop antenna positions for matched operation the first experimental investigation performed was a survey of microwave matching. A general overview of matching behavior was obtained by recording power reflected from the plasma cavity system as a function of cavity length, L_s, and coupling antenna length, L_p, for fixed input power and discharge pressure. The numerical value of reflected power verses these two independent variables was plotted as a set of curves. Regions of low reflected power were then identified and investigated.

Absorbed power vs. sliding short position and coupling antenna length has been plotted by other investigators: for empty and dielectric loaded cavities by M. Siegel [24], and for large diameter plasma loaded cavities by P. Mak [25].

4.2. Parameter Space:

Experimental variables influencing the plasma source were classified as: macroscopic controllable input variables U_1, reactor geometry variables U_2, process variables U_3,internal variables X, and output variables Y. A block diagram of the experimental variables is shown in Fig. 4.1.

The macroscopic controllable variables were: 1) discharge pressure/flow rate, 2) loop antenna length, 3) cavity length, and 4) incident power. This system did not have a throttle valve, thus discharge pressure, p, and flow rate, $\dot{r}$, were interdependent and thus were considered a single variable, $p/\dot{r}$. Discharge pressures investigated were 0.75, 40, 70, and 100 mtorr and the corresponding argon flow rates were 20, 80, 100, and 120 sccm, respectively. The loop length, L_p, was varied in half centimeter intervals from 1.5 cm to 5.5 cm. The cavity length, L_s, was varied from 4.5 cm to 13.35 cm. Input power, P_{inc}, in all experiments described in this thesis was held constant at 150 Watts.

The reactor geometry variables were: 1) discharge height, *h,* and 2) magnet geometry. Two 7 cm diameter quartz discharge chambers, one 5.6 cm tall and another 6.9 cm tall, were used to vary discharge height. Note that the 5.6 cm discharge extends a distance of 1.4 cm into the microwave cavity and the 6.9 cm discharge extends a distance of 2.7 cm. A multipolar ECR magnet ring (see Section 2.4.3) was used to provide a magnetic field when needed. The plasma source behavior was investigated with both discharge chambers

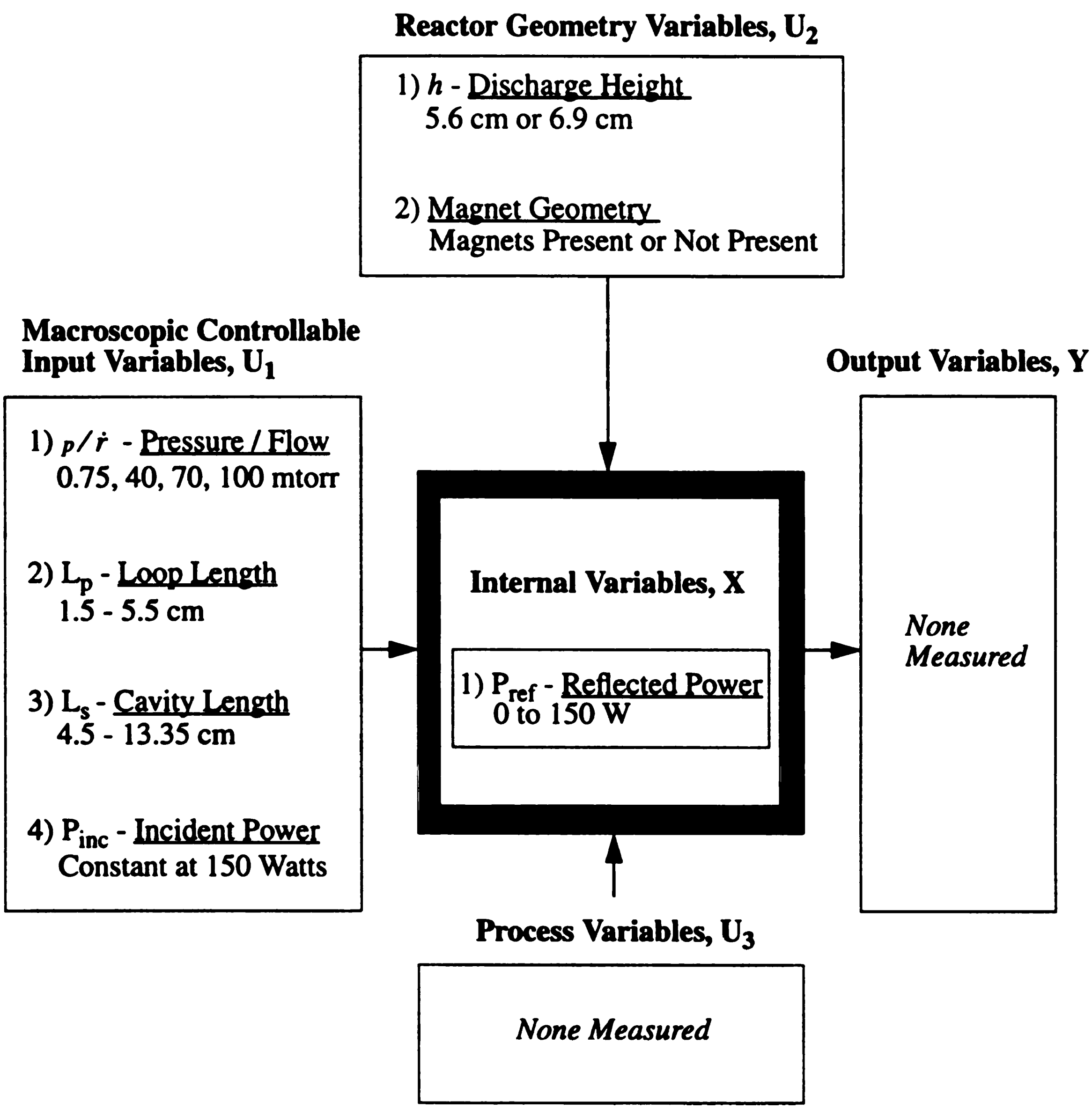

Figure 4.1 - Block diagram of experimental variables

and both with and without the ECR magnets. Thus the four discharge geometry configurations investigated are:

1.) a 5.6 cm tall discharge chamber with multipolar ECR magnet ring

2.) a 6.9 cm tall discharge chamber with multipolar ECR magnet ring

3.) a 5.6 cm tall discharge chamber without magnets

4.) a 6.9 cm tall discharge chamber without magnets

The only internal variable measured in this experiment was reflected power, P_{ref}. Reflected power ranged from less than one Watt to complete reflection of 150 Watts. Process variables and output variables were not measured in this experimental investigation.

4.3 Experimental Setup and Start-up Procedure:

The plasma source was mounted on the vacuum chamber (1) and connected via a coaxial cable (2) to the microwave network as shown in Figure 4.2. The reflected power was measured from a Hewlet Packard analog power meter (3) and the forward power was measured similarly (4).

In preparation for each set of experiments the appropriate discharge chamber (5) was installed and the magnet array (6) was installed or removed. The vacuum chamber (1) was then pumped down to approximately 50 to 100 mtorr with the mechanical pump (7). The diffusion pump (8) was allowed to warm up with the pneumatic gate valve (9) closed. After approximately 1 hour the gate valve (9) was opened and the system was allowed to

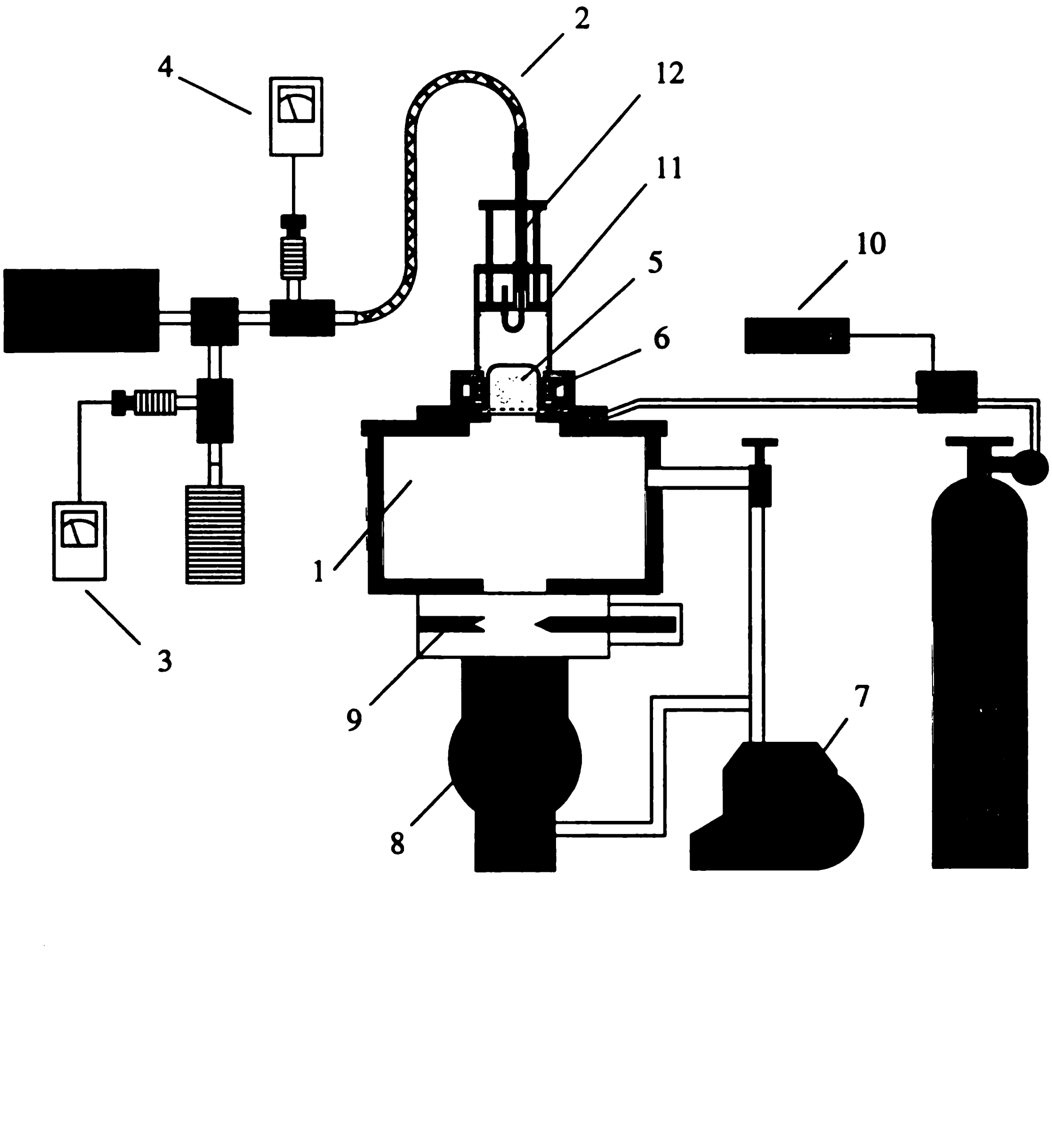

Figure 4.2 - Experimental setup for reflected power measurements

pump down to 10^{-5} Torr. The Argon flow rate was initiated and set with the flow rate controller (10) to a value consistent with the requirements of the experiment. In order to strike the discharge the pneumatic gate valve (9) was closed and pressure was allowed to rise to 100 mTorr or more. The sliding short (11) was set at $L_s = 13.35$ cm with loop antenna (12) position $L_p = 3.5$ cm. Note that $L_s = 13.35$ cm is the highest experimental cavity length. Then microwave power was switched on and increased usually to about 100 to 200 Watts forward power until a discharge glow was seen through the screened window. Forward power was then set to 150 Watts and the gate valve (9) opened. As the pressure of the system was allowed to stabilize the plasma cavity was tuned to minimize reflected power. The pressure was then fine tuned by changing the argon flow rate to the pressure required by the experiment. Approximate flow rates of 20, 80, 100, 120 sccm generated pressures of 0.75, 40, 70 and 100 mtorr, respectively.

4.4 Experimental Procedure for Reflected Power Measurements:

In order to record and plot reflected power as a function of short length, L_s, and loop length, L_p, a set of nine reflected power curves were recorded for each fixed discharge pressure and input power. Each reflected power vs. L_s curve was taken by measuring the reflected power level from the power meter (item 3 in Figure 4.2) as the sliding short of the cavity was varied from its highest position, L_s max, to it's lowest position, L_s min., or vice versa. The loop length was kept constant for each curve and an independent curve was taken for nine separate L_p values at 0.5 cm intervals from $L_p = 1.5$ cm to $L_p = 5.5$ cm. Forward power and discharge pressure were kept constant as each set of nine curves were taken. These nine curves can be thought of as tracing the reflected power contour surface over the L_sL_p plane. An example of such a set of reflected power contour surfaces is shown in Figure 4.3b.

Note that the variable L_{sm} is used to represent the cavity length position of a reflected power minima. In Figure 4.3b L_{sm} vs. L_p curves are plotted in the L_s L_p plane below the nine reflected power trace curves.

Data points for each reflected power vs. L_s curve, such as shown in Figure 4.3a, were not taken at fixed intervals. More data points were taken where the reflected power showed a large change vs. cavity length, such as near reflected power minima. Fewer points were taken where little change was observed. This method was used to avoid missing important maximum and minimum data points that might otherwise be omitted in taking data at standard 0.5 cm intervals. Note, for all data points taken there was always a discharge present.

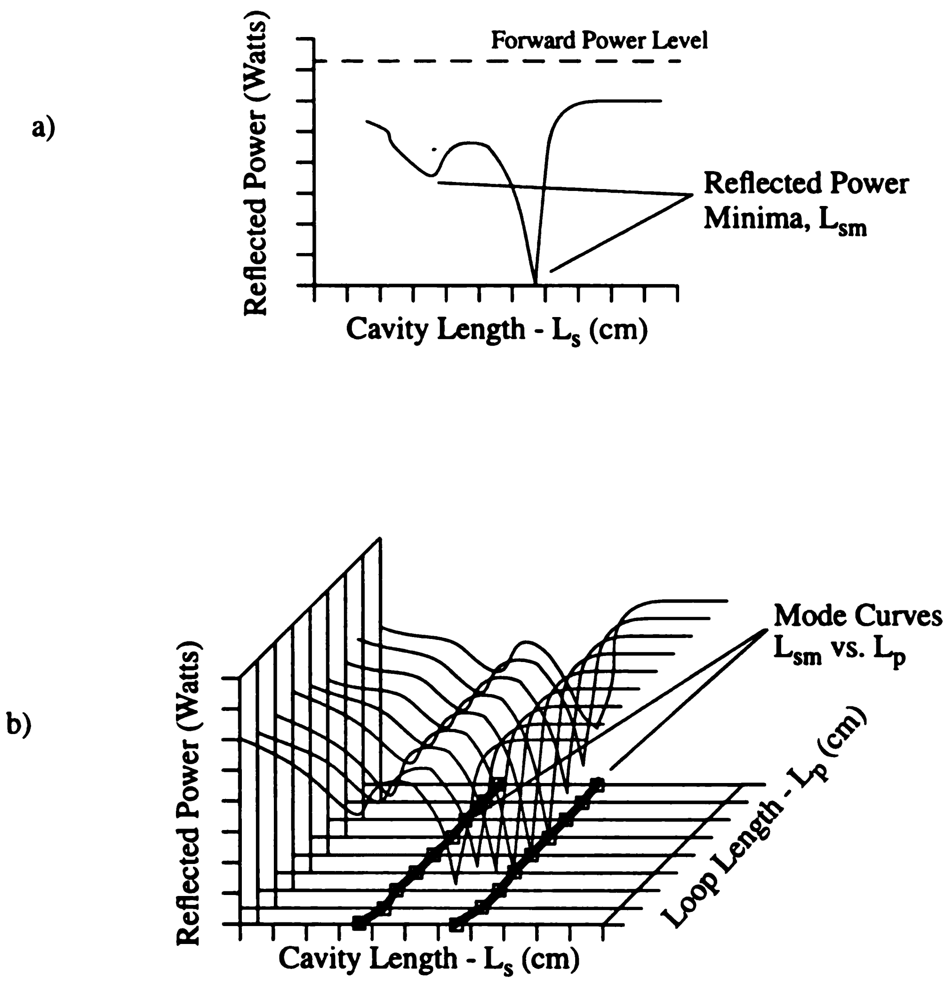

Figure 4.3 - a) An example single reflected power curve for one loop length L_p, b) An example set of nine curves tracing out a reflected power contour surface.

The range of movement of the sliding short was limited by the contact of the loop with the quartz discharge chamber. See Figure 4.4. When the loop was made shorter the range of the sliding short was increased. For example when the 6.9 cm tall discharge was used and the loop was set to a length of L_p = 5.5 cm the range of the sliding short was L_s = 8.2 cm to 13.35 cm. When the loop was set to L_p = 1.5 cm the range of the sliding short was L_s = 4.2 cm to 13.35 cm. The shortest L_s point of each reflected power curve was measured when the loop was in contact with the discharge chamber.

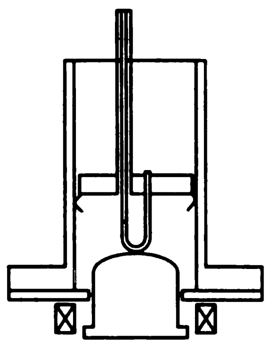

Figure 4.4 - Loop in contact with discharge chamber

The measured reflected power curves, as seen in Figures 4.5 through 4.8, reveal values of L_s and L_p where reflected power is minimized at a specific discharge pressure and reactor configuration. For example, in Figure 4.5a for a pressure of 40 mtorr and loop length of 2.5 cm there are two well matched regions or local reflected power minima at sliding short positions of 8 cm and 9.4 cm. These minima of reflected power are the regions of greatest absorbed power or best electromagnetic match. These regions correspond to conditions when electromagnetic input energy is coupled and matched efficiently to the discharge.

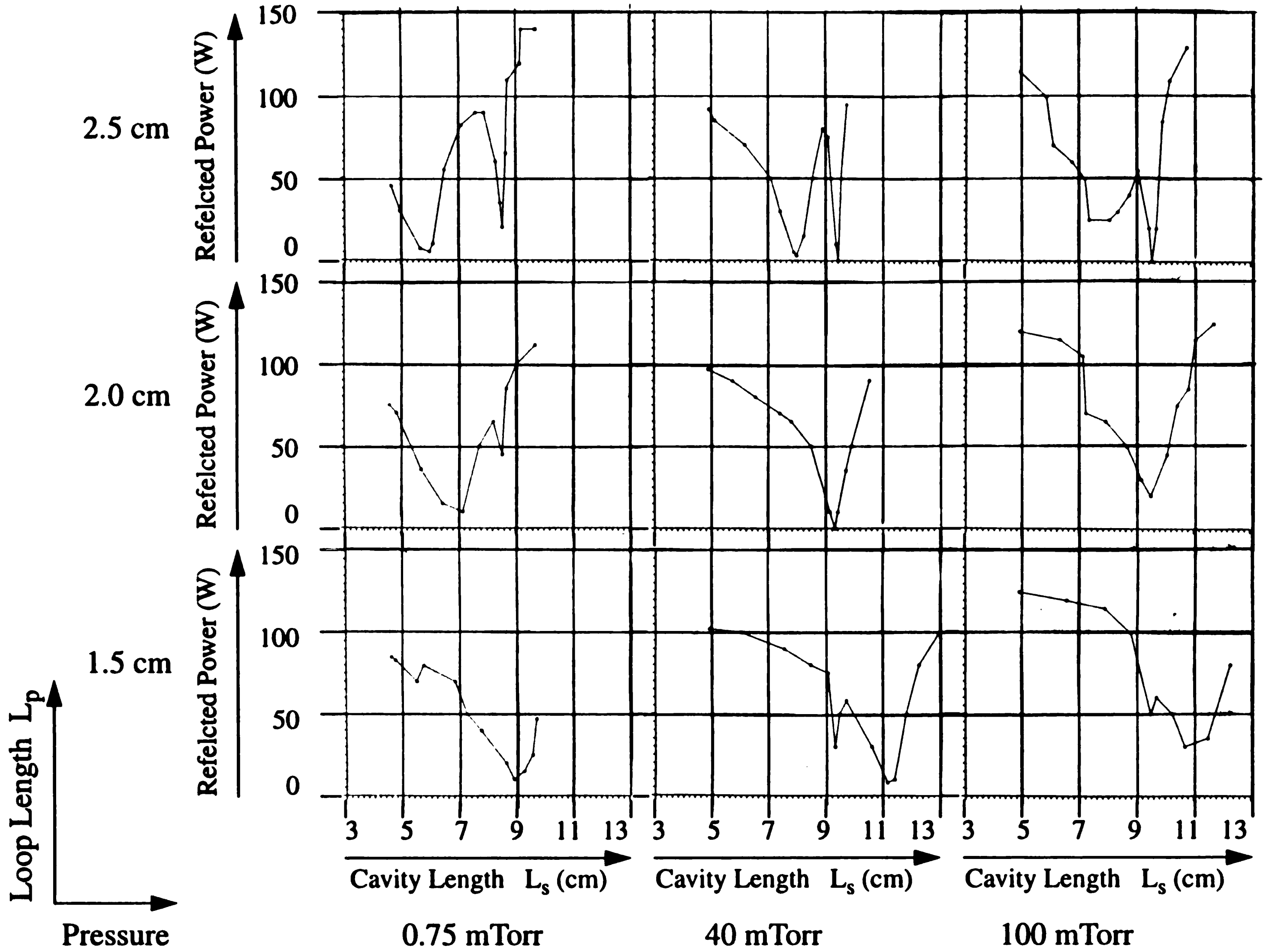

Figure 4.5a - Reflected Power vs. Cavity Length, Loop Length and Pressure for a 5.6 cm tall discharge with ECR magnets.

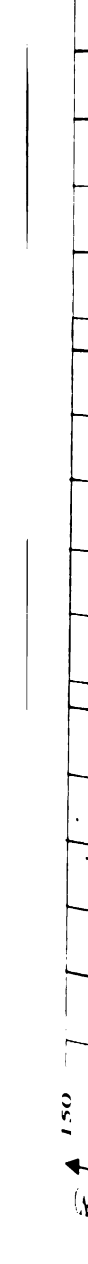
150

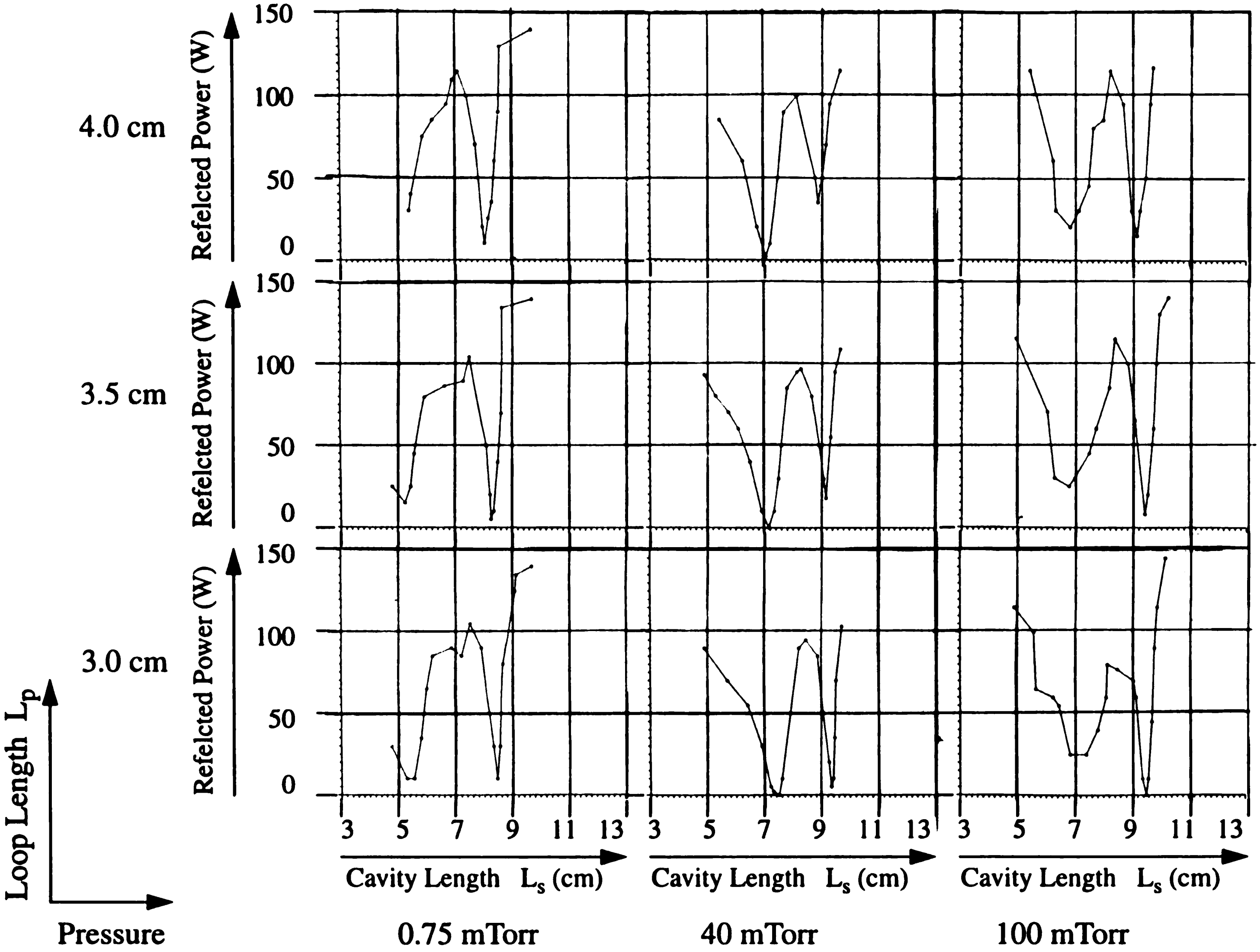

Figure 4.5b - Reflected Power vs. Cavity Length, Loop Length and Pressure for a 5.6 cm tall discharge with ECR magnets.


150

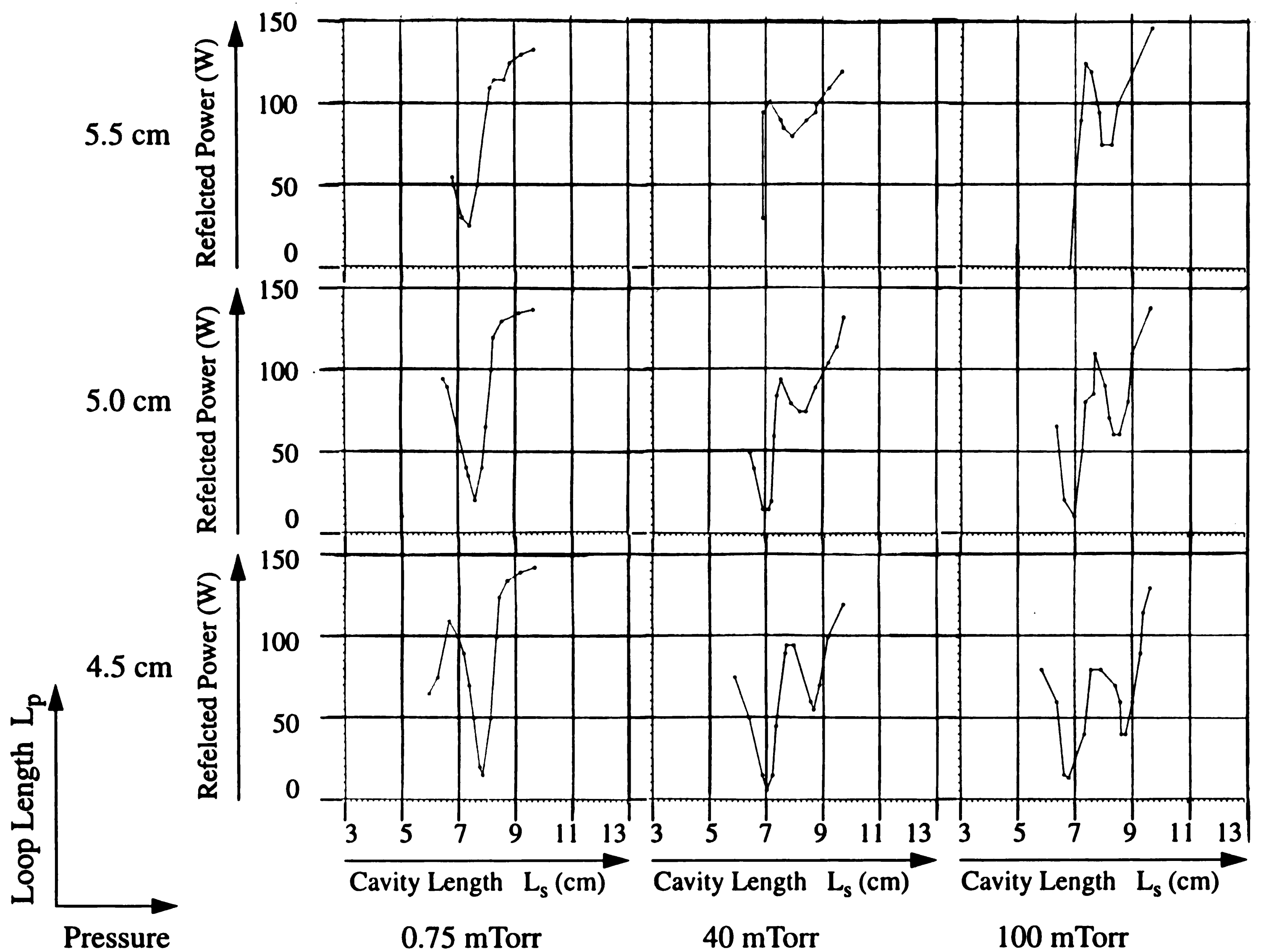

Figure 4.5c - Reflected Power vs. Cavity Length, Loop Length and Pressure for a 5.6 cm tall discharge with ECR magnets.

cu

an

to

se

inv

cm

de

inc

pov

cav

rea

ura

40.

70.

For some conditions of pressure and discharge height one repeatable reflected power curve could be obtained when the cavity length was varied from low to high values of L_S and another different curve could be obtained when the cavity length was varied from high to low L_S. Making a record of this hysteresis phenomenon required the recording of two separate curves, one for increasing L_S and one for decreasing L_S, for every loop length investigated. This is seen in Figure 4.6b for a pressure of 0.75 mtorr and loop length of 3.0 cm where the direction of hysteresis is shown with arrows. Note in this example that the decreasing L_S curve passes over the sharp reflected power minimum achieved by the increasing L_S curve. When no significant hysteresis effect was observed only one reflected power vs. cavity length curve was taken as cavity length was decreased from high to low cavity length, L_S, as shown in all the curves in Figures 4.5a-c.

In the following section (Section 4.5) reflected power curves are presented for the four reactor geometry configurations. Three pressure ranges were investigated for each configuration. In those configurations with ECR magnets the pressures investigated were 0.75, 40, and 100 mTorr. In the configurations without magnets pressures investigated were 40, 70, and 100 mTorr.

4.5 Reflected Power Measurements:

4.5.1 Reflected Power vs. L_s Curves for a 5.6 cm tall Discharge with ECR Magnets:

This experimental configuration used a 5.6 cm discharge chamber, that extends 1.4 cm into the microwave cavity. An eight pole magnet array (see Figure 2.10) was used to create an 875 Gauss ECR zone approximately 0.5 to 1 cm from the quartz walls of the discharge chamber. The pressures investigated in this group were: 0.75 mtorr, 40 mtorr, and 100 mtorr. For each pressure nine loop lengths (L_p) were investigated: 5.5 cm, 5.0 cm, 4.5 cm, 4.0 cm, 3.5 cm, 3.0 cm, 2.5 cm, 2.0 cm, and 1.5 cm. The reflected power vs. cavity length L_s curves are shown in Figures 4.5a-c where pressure increases from 0.75 to 40 to 100 mtorr from left to right and loop length L_p increases from 1.5 cm at the bottom of Figure 4.5a to 5.5 cm at the top of Figure 4.5c. Very little hysteresis was observed for this configuration. Thus, only one curve was plotted for each pressure and loop length.

It can be observed from the plots in Figures 4.5a-c that there are two distinct and well matched cavity length positions for most loop lengths and pressures. For example, in Figure 4.5b at a pressure of 40 mtorr and a loop length of 3.0 cm two minima of reflected power are shown with one minima at a cavity length of 7.6 cm and a second more narrow minima at a cavity length of 9.3 cm. In Chapter 5 these two well matched positions are identified as two different electromagnetic modes of operation. Field pattern measurements for the higher cavity length mode (around L_s = 9 cm) demonstrate that it has a TE_{11} electric field mode pattern. Field pattern measurements for the lower cavity length mode (around L_s = 7 cm) show a circumferentially constant E-field pattern indicative of a ϕ

symmetric excited waveguide mode. It is noted here that this Low L_s mode is wider in its L_s profile for many reflected power curves, shown in Figures 4.5a-c, than the TE_{11} like mode. In most cases the Low L_s mode appears to be approximately 1 cm wide at the 50 Watt level, whereas the TE11 mode is around 0.5 cm wide at the 50 Watt level.

4.5.2 Reflected Power vs. L_s Curves for a 6.9 cm tall Discharge with ECR Magnets:

This experimental configuration used a 6.9 cm discharge chamber, that extends 2.7 cm into the microwave cavity. A multipolar magnet ring (see Figure 2.10) was used to create an 875 Gauss ECR zone approximately 0.5 to 1 cm from the quartz wall of the discharge chamber. The pressures investigated in this group were: 0.75 mtorr, 40 mtorr, and 100 mtorr. For each pressure nine loop lengths (L_p) were investigated: 5.5 cm, 5.0 cm, 4.5 cm, 4.0 cm, 3.5 cm, 3.0 cm, 2.5 cm, 2.0 cm, and 1.5 cm. The reflected power vs. cavity length L_s curves are shown in Figures 4.6a-c where pressure increases from 0.75 to 40 to 100 mtorr from left to right and loop length L_p increases from 1.5 cm at the bottom of Figure 4.6a to 5.5 cm at the top of Figure 4.6c. Considerable hysteresis was observed for this configuration so two curves were plotted, one for decreasing L_s and another for increasing L_s, for each pressure and loop length.

For most reflected power curves only one mode is observed. For example in Figure 4.6b at a pressure of 40 mtorr and a loop length of 3.0 cm a single minima is observed at a short length of 10.9 cm. Electric field pattern measurements presented in Chapter 5 indicate that this mode has TE_{11} electromagnetic excitation. Near zero reflected power can be achieved for this mode for all three pressures investigated.

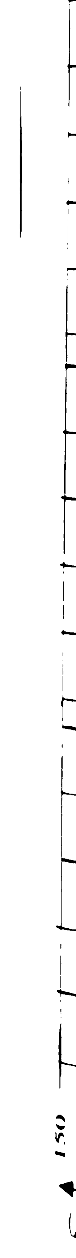
150

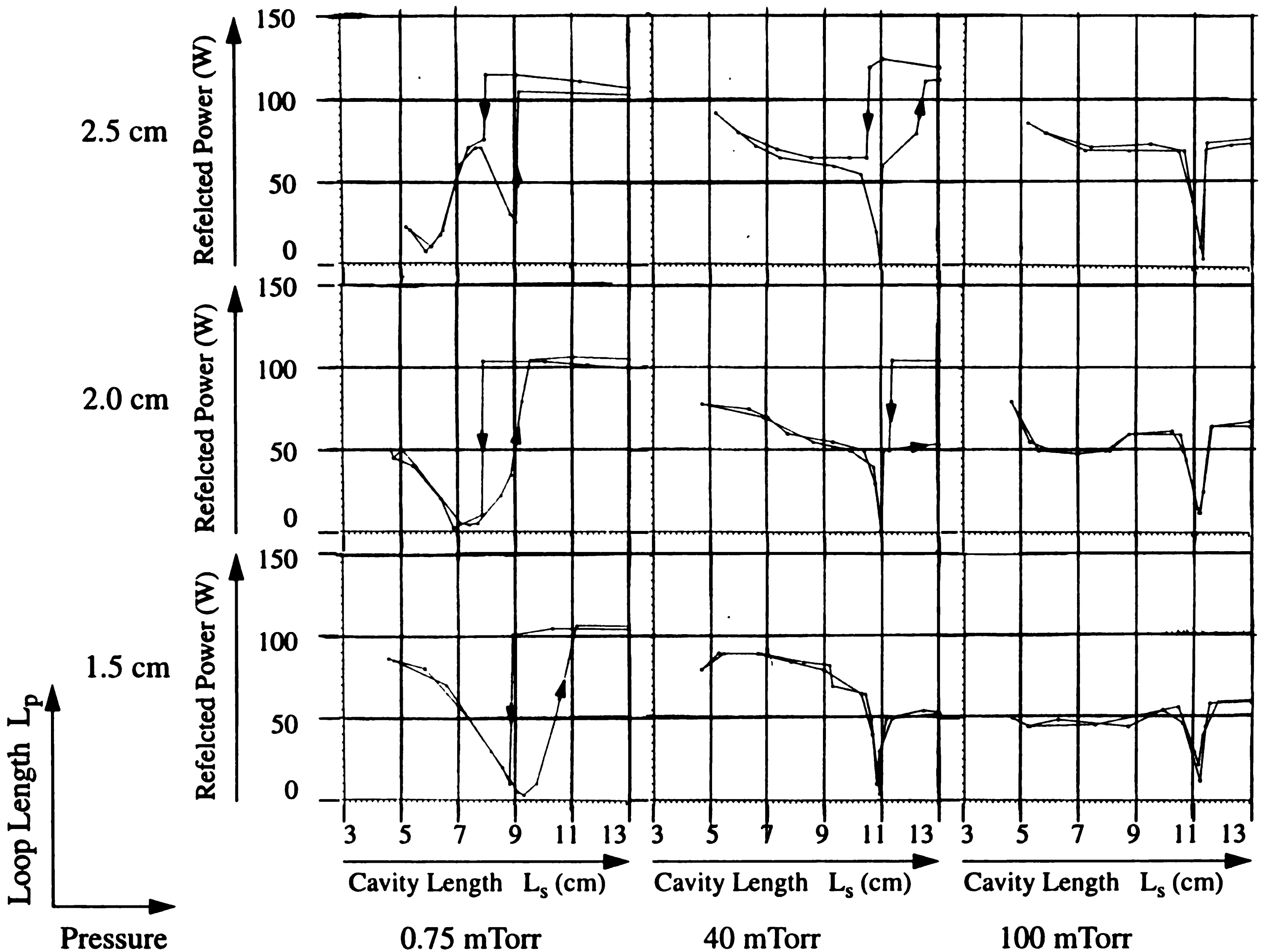

Figure 4.6a - Reflected Power vs. Cavity Length, Loop Length and Pressure for a 6.9 cm tall discharge with ECR magnets.

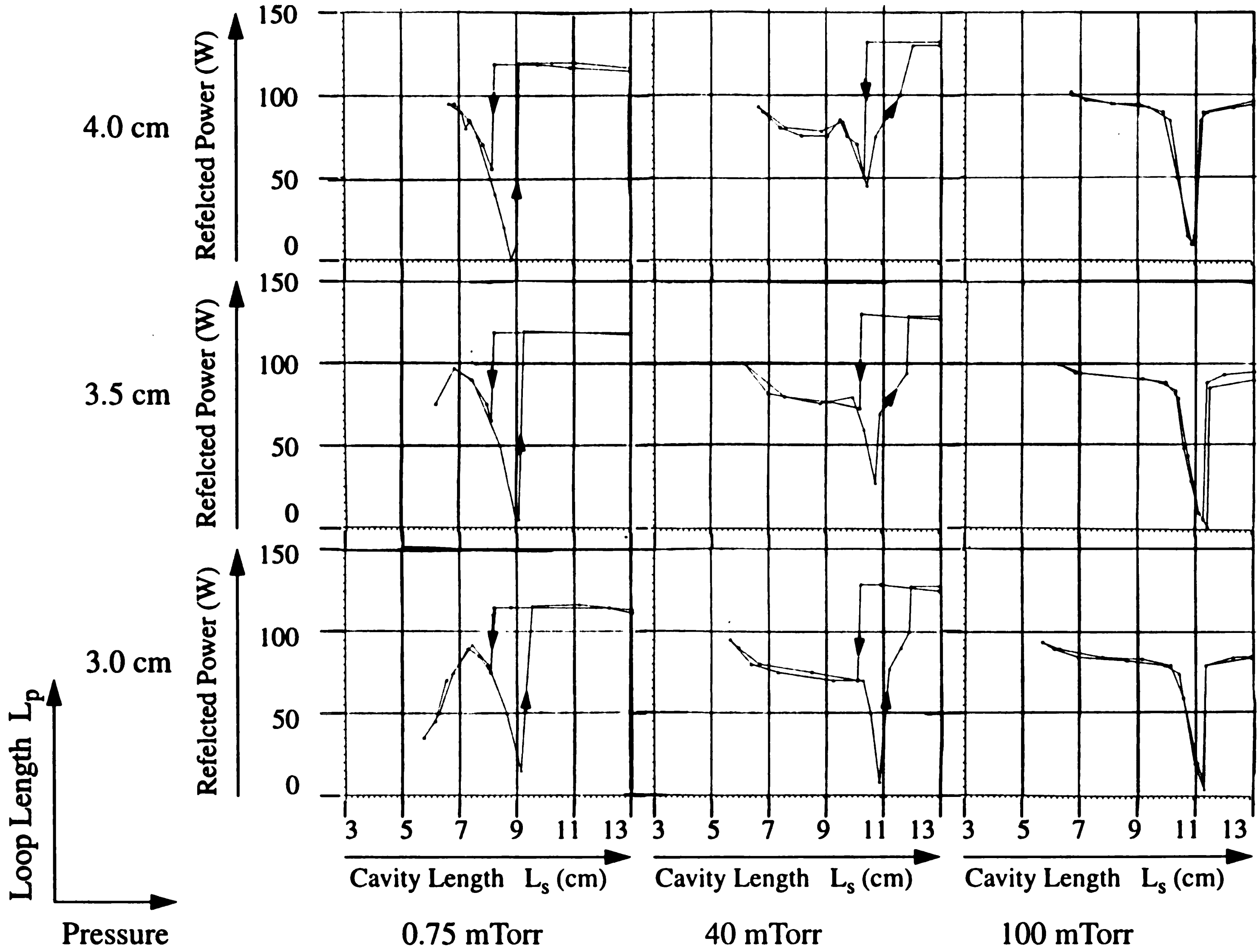

Figure 4.6b - Reflected Power vs. Cavity Length, Loop Length and Pressure for a 6.9 cm tall discharge with ECR magnets.

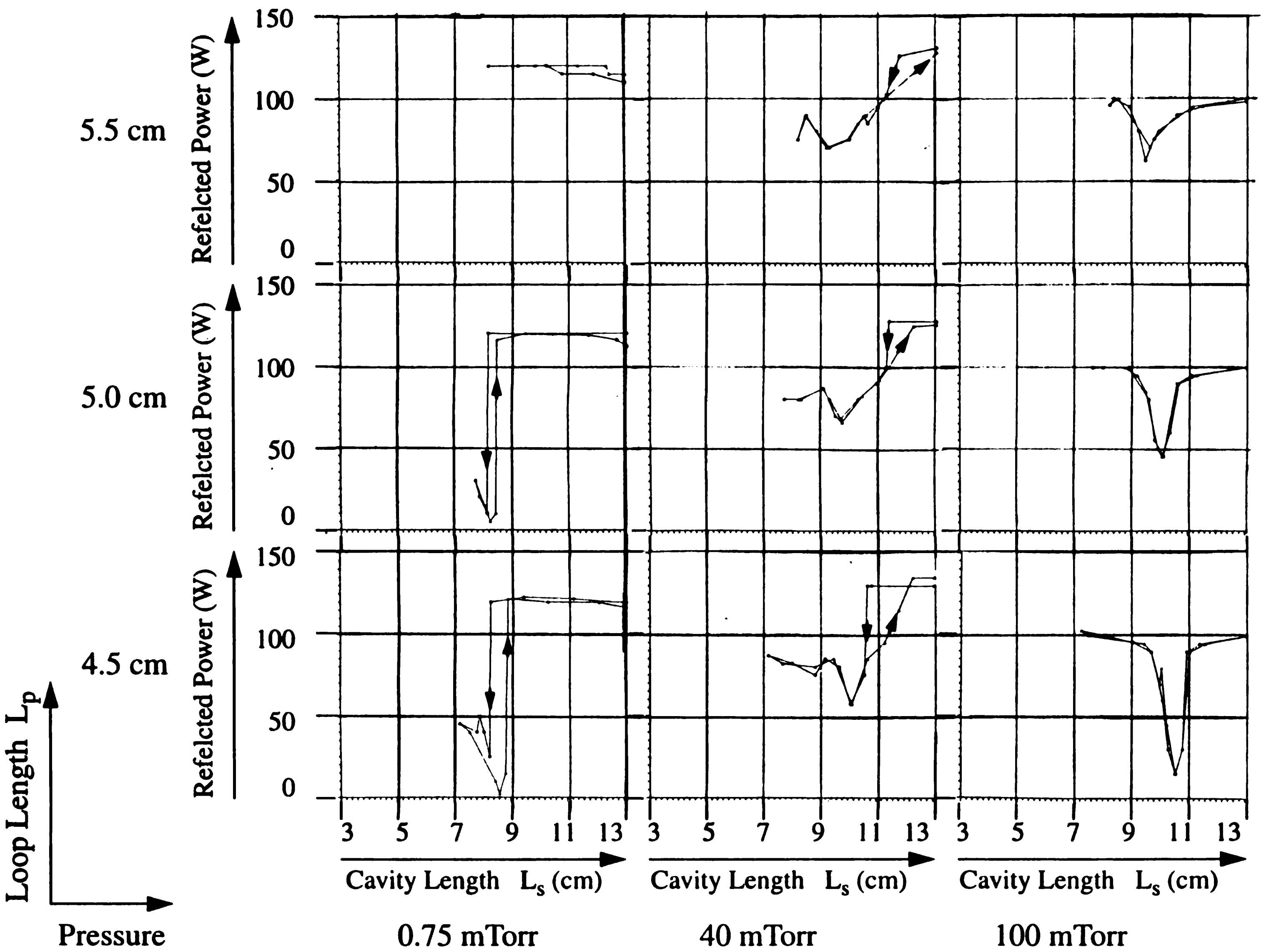

Figure 4.6c - Reflected Power vs. Cavity Length, Loop Length and Pressure for a 6.9 cm tall discharge with ECR magnets.

0.

a

9.

cr

th

2.

ca

ar

sh

pa

is

re

m

re

m

o

le

W

m

Evidence of a second reflected power minima is seen in Figure 4.6a at a pressure of 0.75 mtorr and a loop length of 2.5 cm. Here the second mode or Low L_s mode appears at a cavity length L_s = 5.9 cm. The TE_{11} mode is seen in this reflected power curve at L_s = 9.1 cm. The Low L_s mode is observed for this configuration in five cases: from L_p = 3.5 cm to L_p = 1.5 cm at a pressure of 0.75 mtorr.

Hysteresis is observed in reflected power as the cavity length is first decreased and then increased. This is shown in Figure 4.6a at a pressure of 40 mtorr and loop length of 2.5 cm. In this plot the reflected power curve follows one path for decreasing L_s (as indicated by the arrows) and another path for increasing L_s. As can be seen at other pressures and loop lengths the best matched operating conditions were only achieved as the sliding short increased toward the mode from the low L_s side. Note that, hysteresis is found at pressures of 0.75 and 40 mtorr while very little is found at 100 mtorr.

At a pressure of 100 mtorr and loop lengths between L_p = 3.0 and 1.5 cm more power is absorbed for values of L_s off resonance than at any other pressure or loop length. Off resonance regions are defined as those regions where no minima of reflected power or mode exist. For example in Figure 4.6a at 100 mtorr and L_p = 2.5 cm the off resonance L_s regions are those where the reflected power curve is almost horizontal, whereas the TE_{11} mode region is identified by the steep slope of the curve in the vicinity of L_s = 11.4 cm.

At 100 mtorr and loop lengths from 3.0 cm to 5.5 cm, in Figures 4.6b-c, the average off resonance reflected power was approximately 100 Watts. For the same pressure at loop lengths of 2.5 cm, 2.0 cm, and 1.5 cm the average off resonance reflected power was 90 Watts, 80 Watts, and 65 Watts, respectively. For lower pressures of 0.75 mtorr and 40 mtorr, in Figures 4.6a-c, the off resonance reflected power is generally over 100 Watts.

4

i

b

n

b

s

c

in

a

of

th

w

It

cu

2.

ch

cu

reg

ref

tinu

4.5.3 Reflected Power vs. L_s Curves for a 5.6 cm Tall Discharge Without Magnets:

This experimental configuration used a 5.6 cm discharge chamber, that extends 1.4 cm into the microwave cavity. The ECR magnets were removed in order to investigate the behavior of a non-magnetized discharge. The pressures investigated in this group were: 40 mtorr, 70 mtorr, and 100 mtorr. Note that higher pressures are used in this configuration because a discharge could not be sustained at 0.75 mtorr without magnets. For each pressure nine loop lengths (L_p) were investigated: 5.5 cm, 5.0 cm, 4.5 cm, 4.0 cm, 3.5 cm, 3.0 cm, 2.5 cm, 2.0 cm, and 1.5 cm. The reflected power vs. cavity length L_s curves are shown in Figures 4.7a-c where pressure increases from 40 to 70 to 100 mtorr from left to right and loop length L_p increases from 1.5 cm at the bottom of Figure 4.7a to 5.5 cm at the top of Figure 4.7c.

The absence of a multipolar ECR magnet ring in this configuration appears to restrict the range of L_s, L_p and $p/\dot{r}$ where the discharge is sustainable and also reduces the range where the discharge is well matched (as compared to the 5.6 cm discharge with magnets). It was very difficult to sustain a plasma at 40 and 70 mtorr, consequently reflected power curves were only taken at a loop length L_p = 3.5 cm for 40 mtorr and from L_p = 4.5 to L_p = 2.5 cm at 70 mtorr. The blank areas of Figures 4.7a-c represent conditions where the discharge could not be sustained. For example, in Figure 4.7a there is no reflected power curve at 70 mtorr for loop lengths of L_p = 2.0 and 1.5 cm. Discharges struck in these regions were easily extinguished by slight movements of the sliding short or loop. A reflected power curve was only taken if a discharge could be maintained over a large continuous region of L_s.

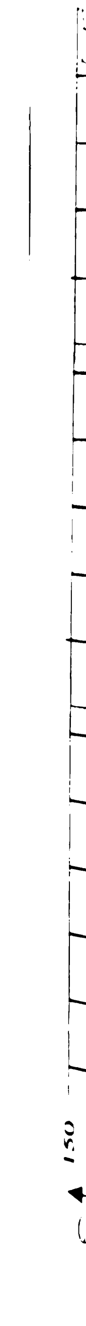
150

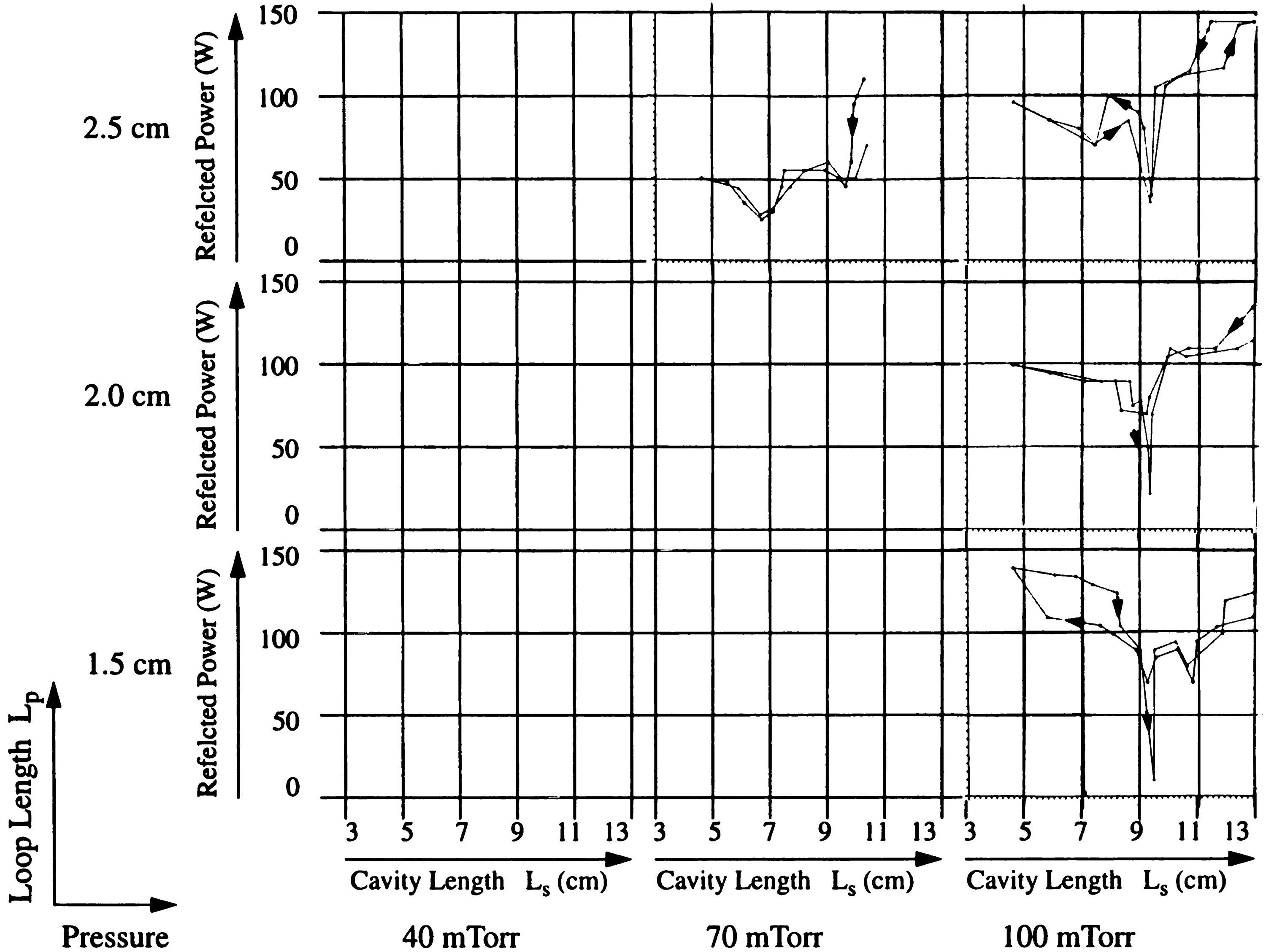

Figure 4.7a - Reflected Power vs. Cavity Length, Loop Length and Pressure for a 5.6 cm tall discharge without magnets.

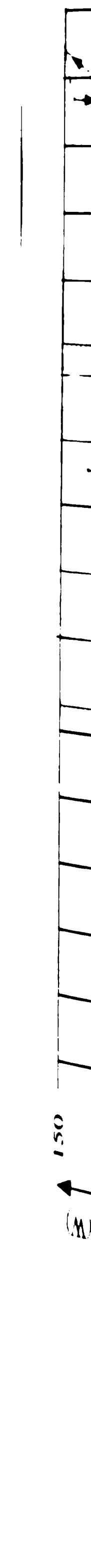
150

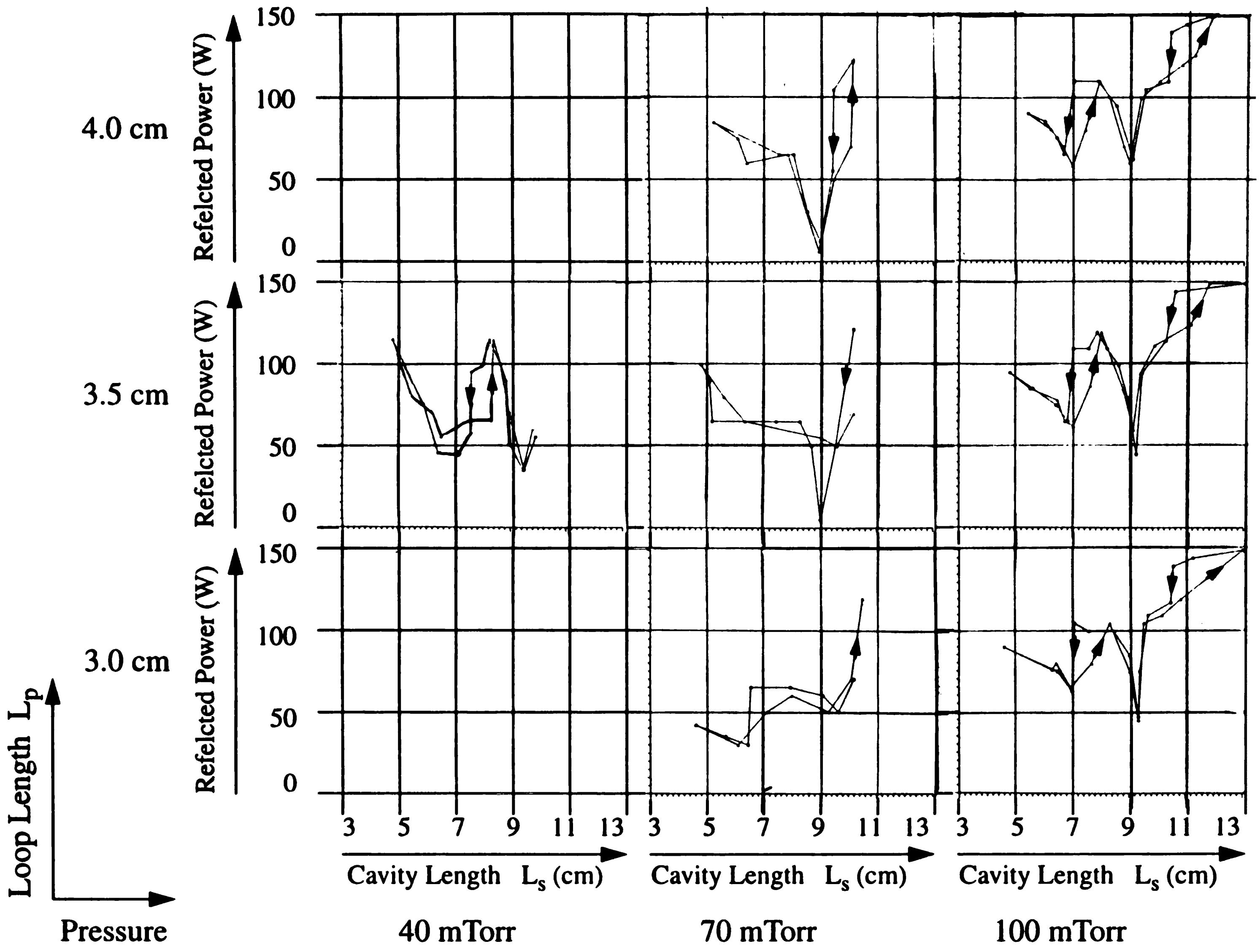

Figure 4.7b - Reflected Power vs. Cavity Length, Loop Length and Pressure for a 5.6 cm tall discharge without magnets.

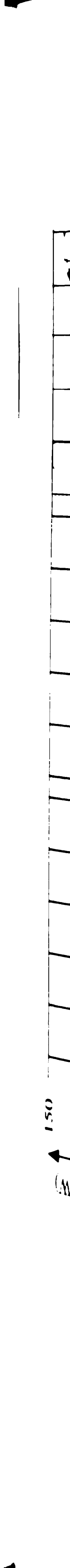
1.50

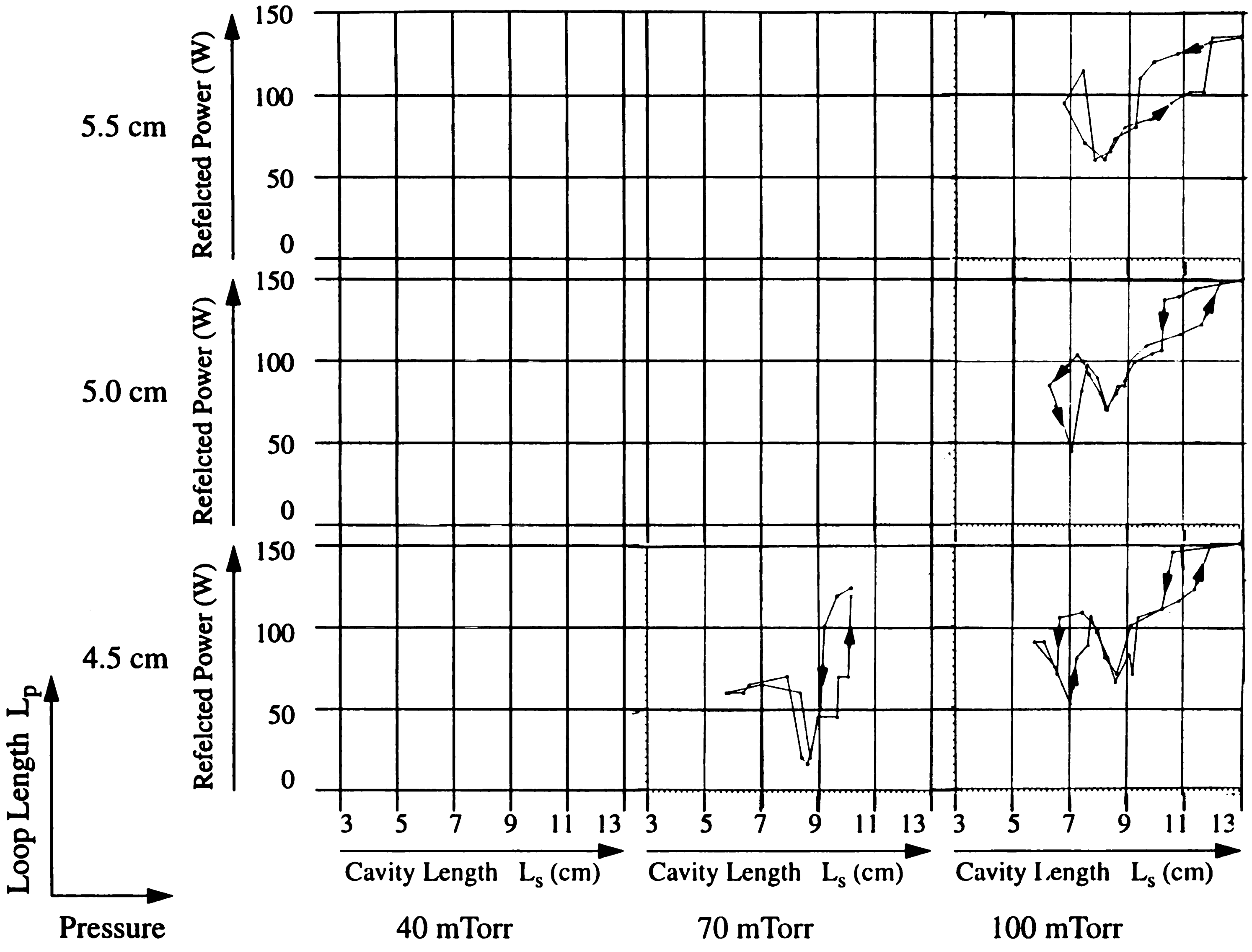

Figure 4.7c - Reflected Power vs. Cavity Length, Loop Length and Pressure for a 5.6 cm tall discharge without magnets.

pr

in

3.

tw

cr

th

le

a

to

co

1

pr

4.

in

in

th

thi

ne

In most reflected power curves in Figures 4.7a-c two reflected power minima are present. For example, in Figure 4.7b, at 40 mtorr and $L_p = 3.5$ cm one minima is observed in the area of 6.5 cm and another is observed near 9.3 cm. Also for loop lengths of 3.0 cm, 3.5 cm, and 4.0 cm, at 100 mtorr two distinct reflected power minima are present. These two minima are similar in sliding short position to the two minima observed (with the 5.6 cm discharge) with magnets present. Field patterns presented in Chapter 5 indicate that these minima are the TE_{11} mode and the circumferentially symmetric Low L_s mode.

The TE_{11} mode is well matched (with near zero reflected power) at 70 mtorr at loop lengths of 4.0 cm and 3.5 cm. Another well matched minima is observed at 100 mtorr and a loop length of $L_p = 1.5$ cm. However, as seen in Figures 4.7a-c, a reflected power of 30 to 50 Watts is the best match for most reflected power curves taken for both modes for this configuration. Note that the maximum reflected power for most curves is in the range of 110 to approximately full reflected power of 150 Watts. Hysteresis was observed in all profiles.

4.5.4 Reflected Power vs. L_s Curves for a 6.9 cm tall Discharge without Magnets:

This experimental configuration used a 6.9 cm discharge chamber, that extends 2.7 cm into the microwave cavity. No ECR magnets were used in this configuration in order to investigate the behavior of the non-magnetized discharge. The pressures investigated in this group were: 40 mtorr, 70 mtorr, and 100 mtorr. Note that higher pressures are used in this configuration because a discharge could not be sustained at 0.75 mtorr without magnets. For each pressure nine loop lengths (L_p) were investigated: 5.5 cm, 5.0 cm, 4.5 cm, 4.0 cm, 3.5 cm, 3.0 cm, 2.5 cm, 2.0 cm, and 1.5 cm. The reflected power vs. cavity length L_s curves are shown in Figures 4.8a-c where pressure increases from 40 to 70 to 100 mtorr from left to right and loop length L_p increases from 1.5 cm at the bottom of Figure 4.8a to 5.5 cm at the top of Figure 4.8c.

This 6.9 cm discharge configuration without ECR magnets demonstrates a greater ability to sustain the discharge over a large variation of L_s and L_p and match the discharge at pressures of 40 and 70 mtorr than does the 5.6 cm discharge configuration without magnets. A plasma could be sustained at all loop lengths and pressures in this investigation. Several reflected power curves that show minima with near zero reflected power are seen in Figures 4.8a-b.

For this configuration only one mode is observed for all reflected power profiles. For example, in Figure 4.8b at 70 mtorr and loop length of 3.5 cm one distinct reflected power minima is observed at 11.5 cm. In Chapter 5 this minima is shown to be the TE_{11} mode. No evidence of the Low L_s mode was observed.

Hysteresis is observed at loop lengths of 5.5 cm, 5.0 cm, 3.5 cm, 3.0 cm and 1.5 cm for 70 mtorr and between loop lengths of 1.5 cm and 3.0 cm for 100 mtorr. However, note that the hysteresis observed in Figures 4.6a-c for this discharge height with magnets is much more pronounced, i.e. the curves for increasing L_s are much different than for decreasing L_s, than the hysteresis displayed in figures 4.8a-c. Note that hysteresis is observed at 100 mtorr without magnets while very little is observed at 100 mtorr when magnets are present. At 100 mtorr the reflected power curves with (Figures 4.6a-c) and without magnets (Figures 4.8a-c) appear very similar. Even the reduction of background reflected power at shorter loop lengths is present in both configurations. In both configurations the

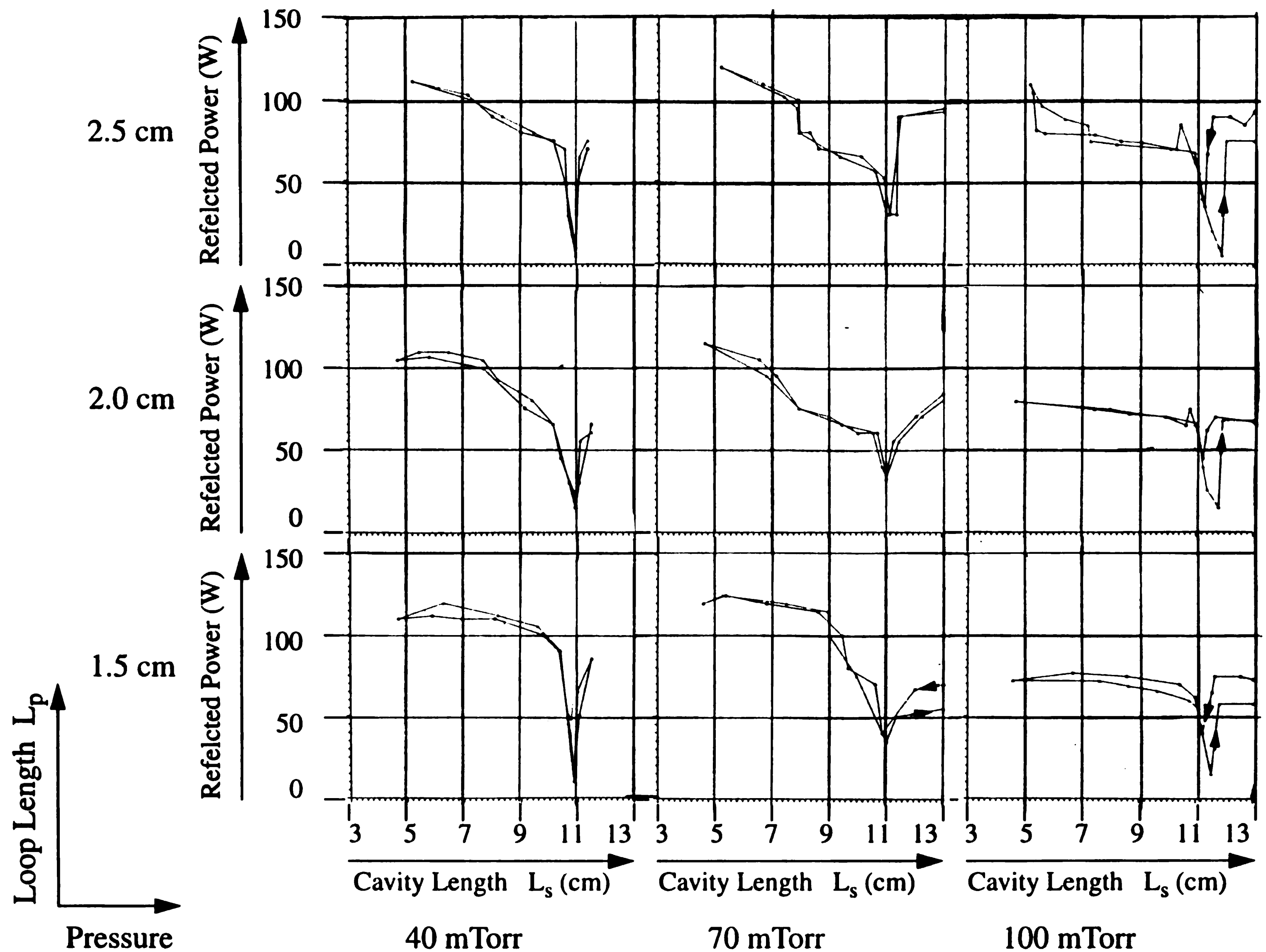

Figure 4.8a - Reflected Power vs. Cavity Length, Loop Length and Pressure for a 6.9 cm tall discharge without magnets.


150

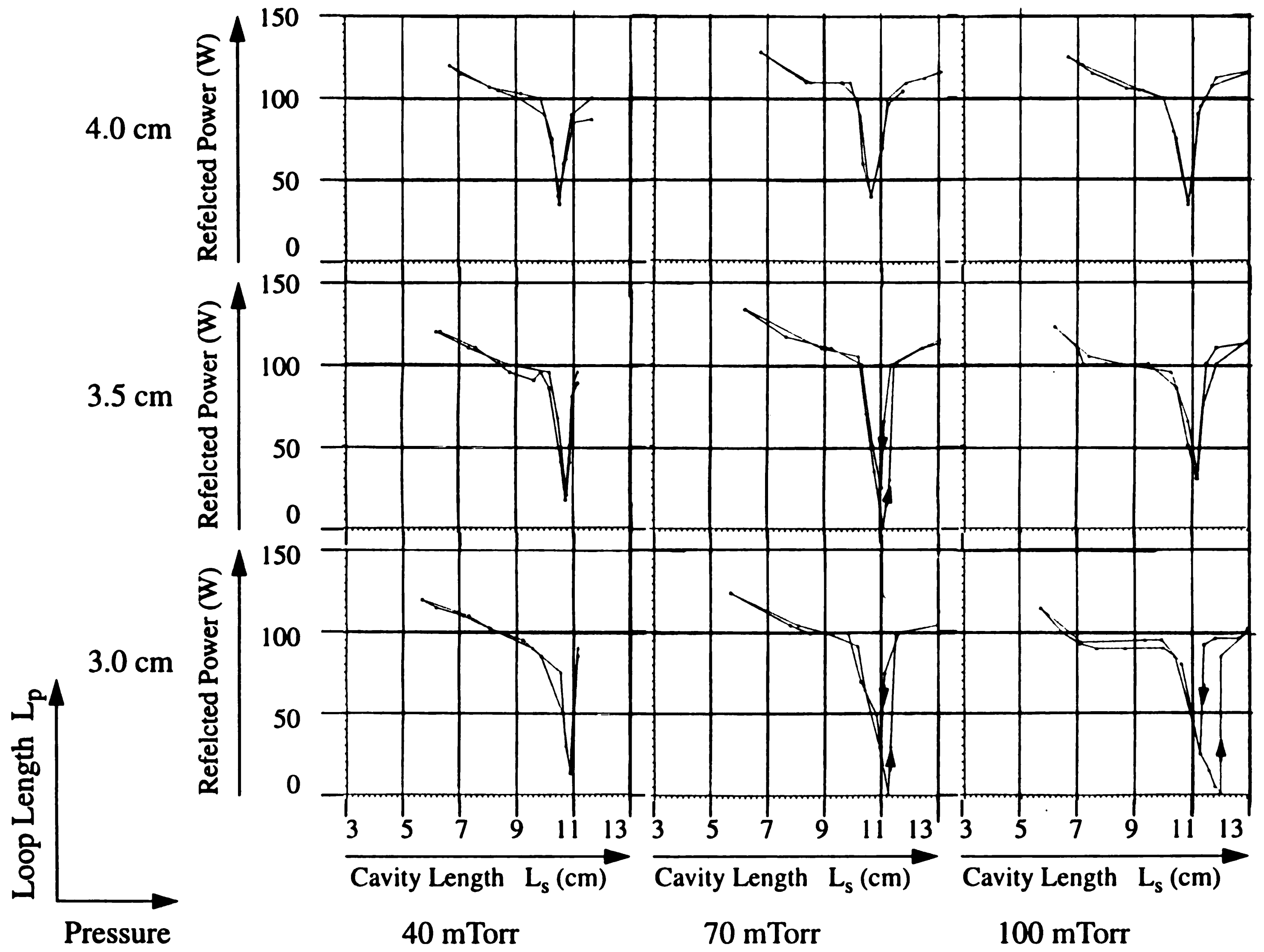

Figure 4.8b - Reflected Power vs. Cavity Length, Loop Length and Pressure for a 6.9 cm tall discharge without magnets.

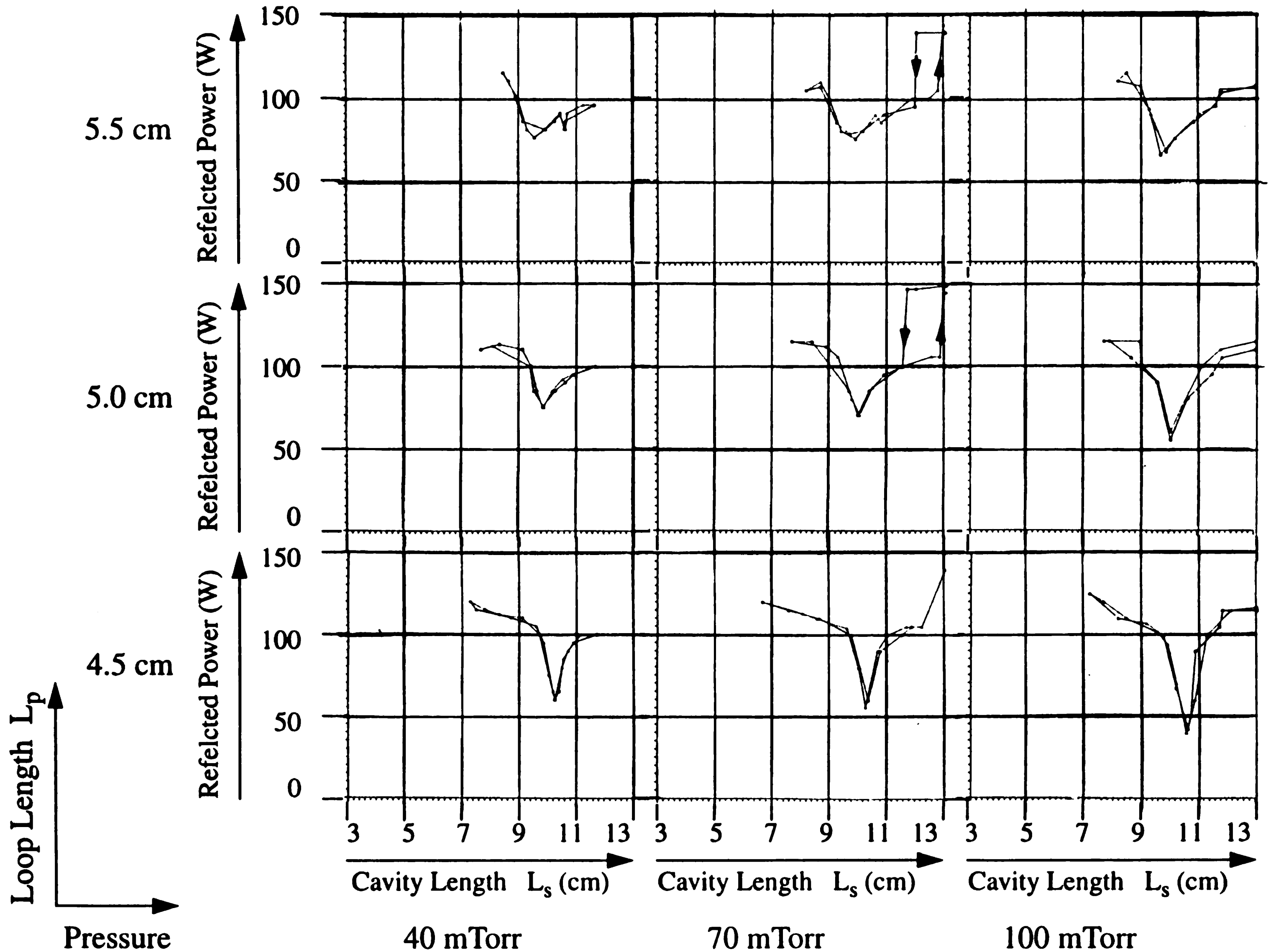

Figure 4.8c - Reflected Power vs. Cavity Length, Loop Length and Pressure for a 6.9 cm tall discharge without magnets.

p off resonance reflected power at 100 mtorr for loop lengths of L_p = 2.5 cm to 1.5 cm is generally lower than for the same loop lengths at 40 mtorr and 70 mtorr. For example, in Figure 4.8a at 100 mtorr and loop length of 1.5 cm the off resonance reflected power is approximately 80 Watts, whereas at 70 mtorr and 40 mtorr the average off resonance reflected power for L_p = 1.5 cm is approximately 125 Watts and 115 Watts, respectively.

4.6 Analysis of Electromagnetic Mode Behavior:

4.6.1 Observations of Mode Behavior for the Four Source Geometry Configurations:

In order to facilitate the comparison of the electromagnetic mode behavior of each configuration (for a constant incident power of 150 Watts) vs. variation in L_s, L_p and $p/\dot{r}$ summary graphs are shown in Figure 4.9a-d. The summary graphs plot the cavity length positions of each minima of reflected power for each loop length and pressure investigated. The points on these summary graphs are obtained by recording the reflected power minima locations on Figures 4.5 through 4.8. These summary graphs provide an overall picture of changes in position of matched conditions as the cavity length L_s, and loop length L_p, is varied. They can be thought of as the minimum points of a contour surface, as shown by Figure 4.3b. The minimum points of the trace curves in Figure 4.5a-c are plotted and connected by lines in Figure 4.9a. Note that more than one discharge pressure, and hence more than one curve for the same mode, is plotted on each summary graph.

■ Denotes that mode is well matched <10% Reflected Power
□ Denotes that mode is between 10% and 60% Reflected Power

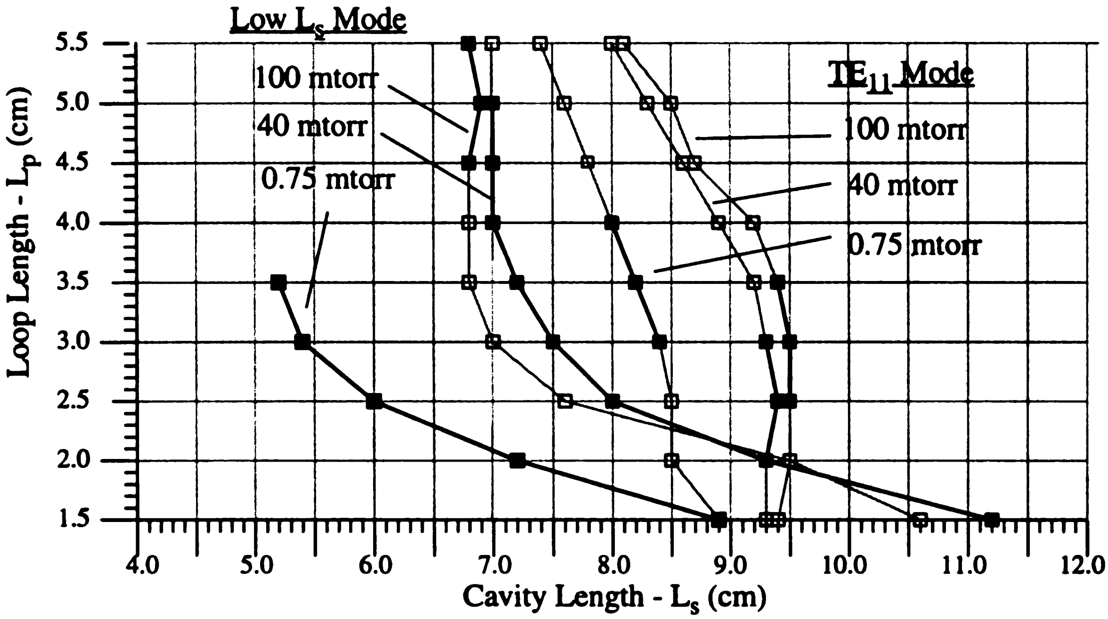

Figure 4.9a - Best matched positions for the 5.6 cm discharge with ECR magnets

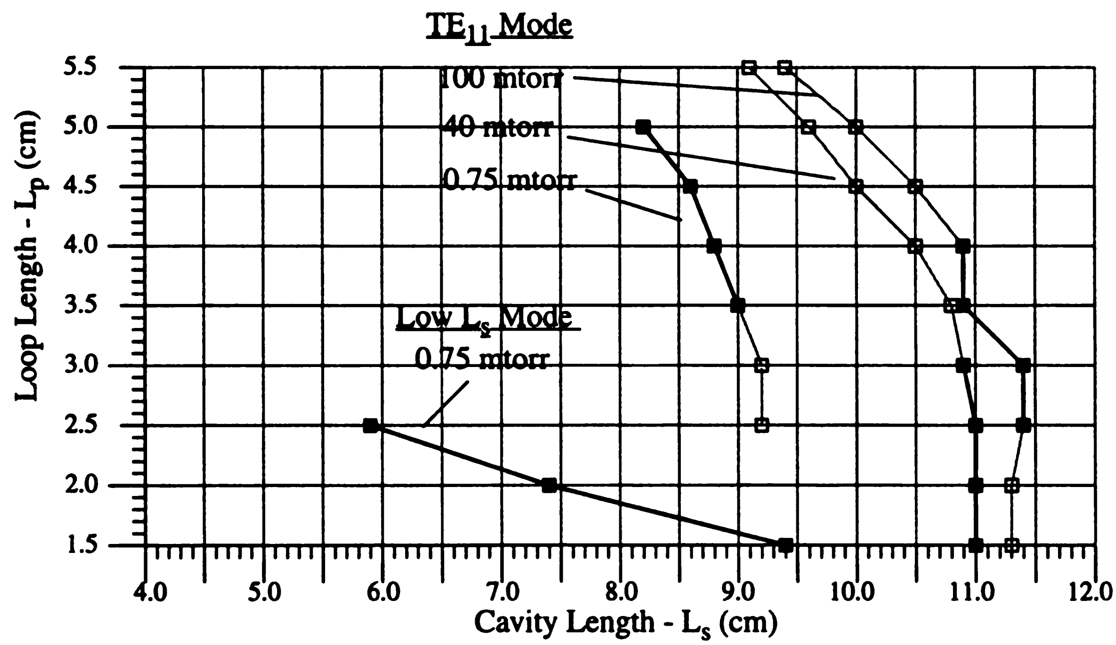

Figure 4.9b - Best matched positions for the 6.9 cm discharge with ECR magnets

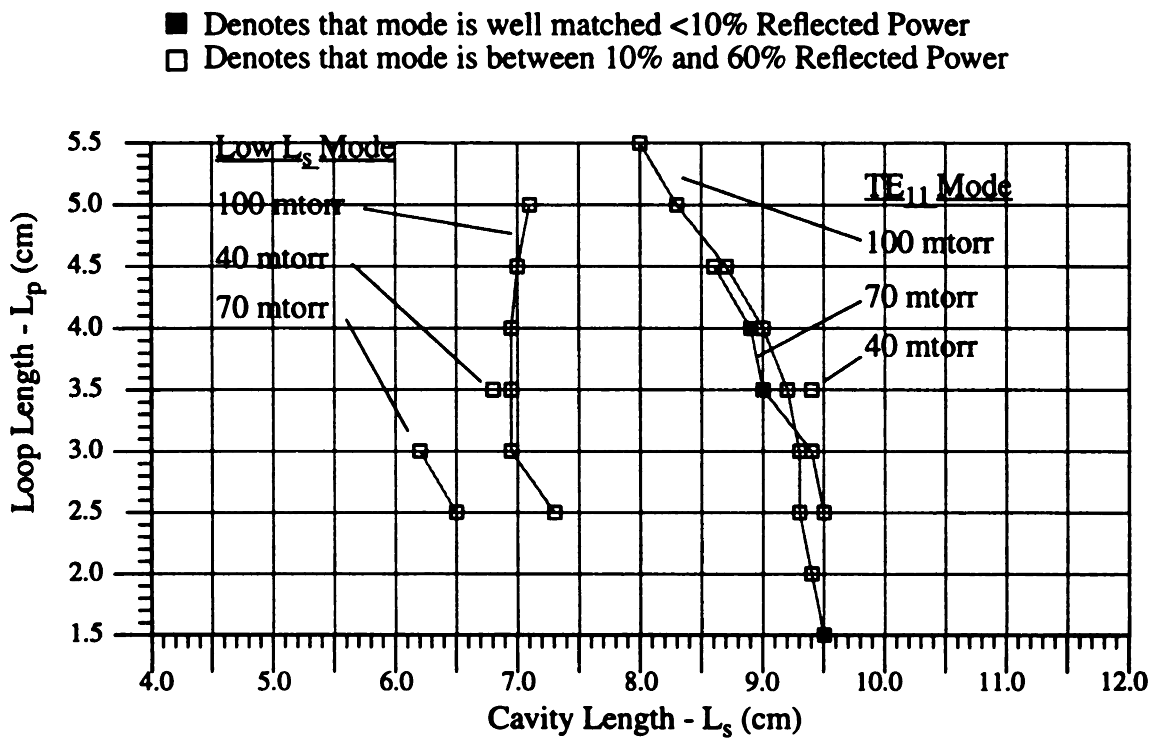

Figure 4.9c - Best matched positions for the 5.6 cm discharge without magnets

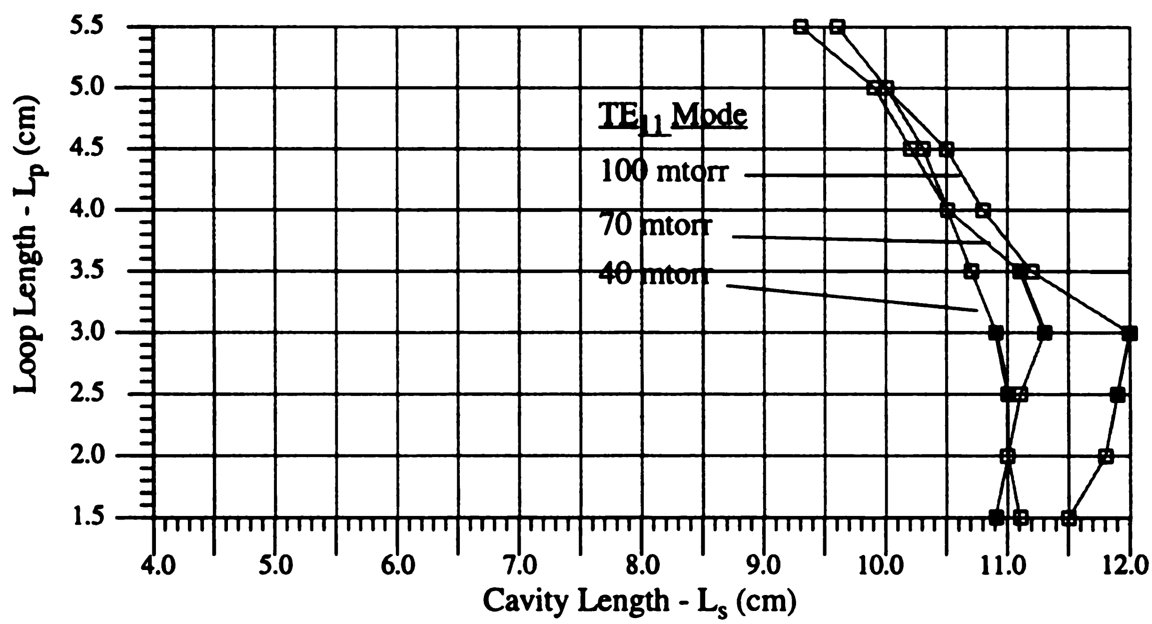

Figure 4.9d - Best matched positions for the 6.9 cm discharge without magnets

On each summary graph solid squares indicate reflected power minima where less than 10% of forward power (i.e. 15 Watts) is reflected. Empty squares indicate reflected power minima positions that have between 10% and 60% (or between 15 and 90 Watts) reflected power. No minima were defined when reflected power was greater than 60%. Collections of data points taken for a constant pressure and the same mode are connected by lines. The resulting curves are identified as L_{sm} vs. L_p mode curves or constant pressure mode curves (recall that L_{sm} is the variable representing the cavity length position for a minima of reflected power for a particular mode). For example in Figure 4.9a the TE_{11} mode has three such L_{sm} vs. L_p curves for pressures of 0.75 mtorr, 40 mtorr, and 100 mtorr. Solid black lines connect two well matched points, whereas grey lines connect all other points.

4.6.2 Pressure Dependent Changes in Mode Cavity Length:

For each mode change in mode cavity length vs. discharge pressure can be studied with the aid of Figures 4.9a-d. Significant changes in mode cavity length can be seen for changes in discharge pressure. For the 5.6 cm discharge with magnets, shown in Figure 4.9a, the average increase in mode cavity length for the TE_{11} mode is 0.825 cm from the 0.75 mtorr mode curve to the 40 mtorr curve and 0.16 cm from 40 mtorr to 100 mtorr. Note that the discharge pressure increase from 0.75 mtorr to 40 mtorr is a 50 fold increase, while the increase from 40 mtorr to 100 mtorr is only a 2.5 fold pressure increase. For the 6.9 cm discharge with magnets, shown in Figure 4.9b, the average cavity length increase is 1.63 cm from 0.75 mtorr to 40 mtorr and is 0.35 cm from 40 mtorr to 100 mtorr.

In the configurations without magnets the pressures studied were 40, 70, and 100 mtorr and therefore covered a much smaller range of discharge pressure than the configurations with ECR magnets present. The change in mode curve position from 40 mtorr to 70 mtorr or to 100 mtorr is difficult to determine, because only one point was obtained at 40 mtorr. However, one significant observation is that this single point is 0.2 cm higher in cavity length than the mode curves for 70 and 100 mtorr. The average difference between the 70 mtorr curve and the 100 mtorr curve is very small at 0.1 cm. It should be noted that the pressure of 70 mtorr provides the best matching conditions for the TE_{11} mode for this configuration. For the TE_{11} mode in the 6.9 cm discharge, see Figure 4.9d, the average increase in mode curve position from 40 to 70 mtorr is 0.18 cm. The average increase from 70 mtorr to 100 mtorr is 0.37 cm. Consequently, the total average increase from 40 mtorr to 100 mtorr is 0.55 cm. Note that as pressure is increased from 40 mtorr to 70 mtorr and from 70 to 100 mtorr a deviation or local increase in cavity length is observed for portions of the mode curves between loop lengths of $L_p = 3.5$ cm and 1.5 cm.

For the low L_s mode with ECR magnets, shown in Figure 4.9a, when there is a change in pressure from 0.75 mtorr to 40 mtorr the average change in mode cavity length is 2.1 cm. When the pressure is further increased from 40 mtorr to 100 mtorr the mode cavity length, surprisingly, decreases in length on average 0.4 cm. In the 6.9 cm discharge with magnets, shown in Figure 4.9b, the Low L_s mode is only found at 0.75 mtorr and can not be compared vs. other pressures. In the 5.6 cm discharge without magnets, shown in Figure 4.9c, when the pressure is changed from 40 mtorr to 70 mtorr the mode cavity length is seen to decrease about 0.7 cm, but then as pressure is increased to 100 mtorr the mode cavity length increases once more about 0.8 cm. For the 6.9 cm discharge without magnets, shown in Figure 4.9d, the Low L_s mode could not be found.

4.6.3 Increase in mode cavity length with decrease in loop length:

For all cases of the TE_{11} mode observed in Figures 4.9a-d the cavity length of the mode increases as the loop length is decreased. This can be seen for 0.75 mtorr with a 5.6 cm tall discharge, in Figure 4.9a, where at a loop length of 5.5 cm the mode cavity length is L_s = 7.4 cm. The cavity length steadily increases to L_s = 8.4 cm as loop length is decreased to L_p = 3.0 cm and levels off somewhat at L_s = 8.5 cm as the loop is further decreased to L_p = 2.0 cm. Other curves for the TE_{11} mode at other pressures, discharge sizes, regardless of magnetic confinement show the same type of behavior.

A large increase in cavity mode length is also observed in the Low L_s mode with decrease in loop length. However a somewhat different behavior is observed with the Low L_s mode than with the TE_{11} excited mode. The slope of all the TE_{11} L_p vs. L_s mode curves, seen in Figure 4.9a, appear to start out at some negative value and then become almost vertical as the loop length is decreased from 5.5 cm to 1.5 cm. In contrast, the Low L_s mode curves, as seen in Figure 4.9a, appear to start out with vertical slope and then level off to small negative and almost horizontal slope as the loop is decreased from 5.5 cm to 1.5 cm.

4.6.4 Change in Mode Cavity Length vs. Discharge Height:

Using the data presented in Figures 4.9a-d it is possible to compare cavity length positions of constant pressure mode curves vs. discharge chamber height. The cavity lengths and loop lengths for each specific mode at a specific pressure can be taken from separate figures and plotted on the same graph to make direct cavity length comparisons. These mode position vs. discharge height comparison graphs are shown in Figures 4.10 - 4.12.

The graph comparing cavity length of the TE_{11} excited mode in the 5.6 cm discharge (at 0.75 mtorr with ECR magnets) vs. the same mode in the 6.9 cm discharge is shown in Figure 4.10a. As can be seen from the two constant pressure mode curves there is an increase in cavity length on the order of 0.8 cm between curves from the 5.6 cm discharge to the 6.9 cm discharge. The cavity length difference of 0.8 cm is significantly smaller than the difference in discharge height which is 1.3 cm. The shape and slope of the mode lines are generally the same for both discharge chambers.

In Figure 4.10b the TE_{11} mode at 40 and 100 mtorr is compared for the two configurations with ECR magnets. At 40 mtorr the average increase in mode curve cavity length is 1.5 cm from the 5.6 cm discharge to the 6.9 cm discharge. For 100 mtorr this average increase is 1.7 cm. The general shape of the mode curves appears the same, both having a segment of steep negative slope from L_p = 5.5 cm to L_p = 3.5 cm and another segment that is almost vertical from L_p = 3.5 cm to L_p = 1.5 cm. Note that the sloped segment has a steeper (i.e. more a negative) slope in the 5.6 cm discharge than in the 6.9 cm discharge where the slope is more gradual.

A comparison of mode curve position vs. change in discharge height can also be made for the configurations without ECR magnets for pressures of 40, 70, and 100 mtorr. This comparison is displayed in Figure 4.11.

At 40 mtorr only one loop length, L_p = 3.5 cm, could sustain a discharge in the 5.6 cm discharge chamber. Thus, only one point can be compared against the full 6.9 cm discharge chamber mode curve. This is shown in figure 4.11a. As can be readily seen, the difference in cavity length is 1.3 cm from the 5.6 cm discharge to the 6.9 cm discharge.

At 70 mtorr five loop lengths could be sustained for the 5.6 cm discharge chamber. The average increase in mode curve position, as shown in Figure 4.11b, is 1.8 cm. The curves for both discharge lengths appear similar except for a noticeable deviation in the 6.9 cm discharge mode curve for loop lengths between 2.5 and 3.5 cm.

At 100 mtorr the average increase in cavity length is 2.0 cm from 5.6 cm to 6.9 cm discharge, shown in Figure 4.11c. Notice the large deviation in the mode curve in the region of L_p = 2.0 cm to L_p = 3.0 cm for the 6.9 cm discharge chamber.

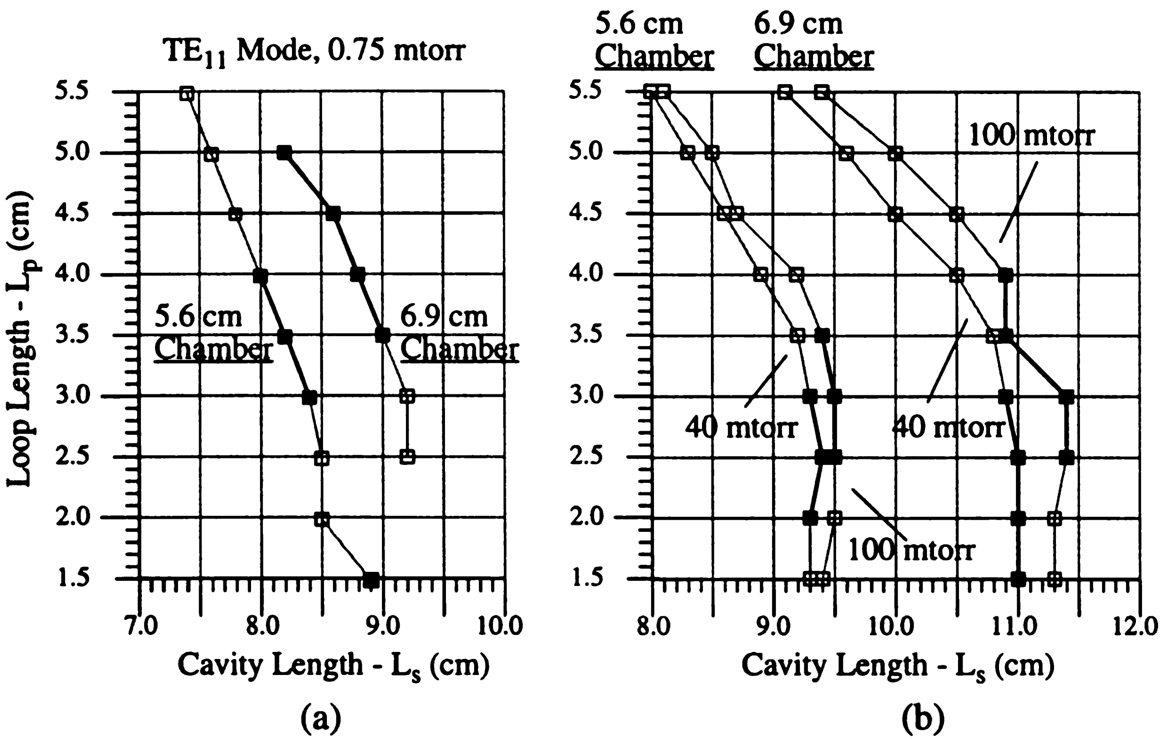

Figure 4.10 - Comparison of Cavity Lengths for the TE_{11} Mode With Magnet Ring vs. Discharge Chamber Height

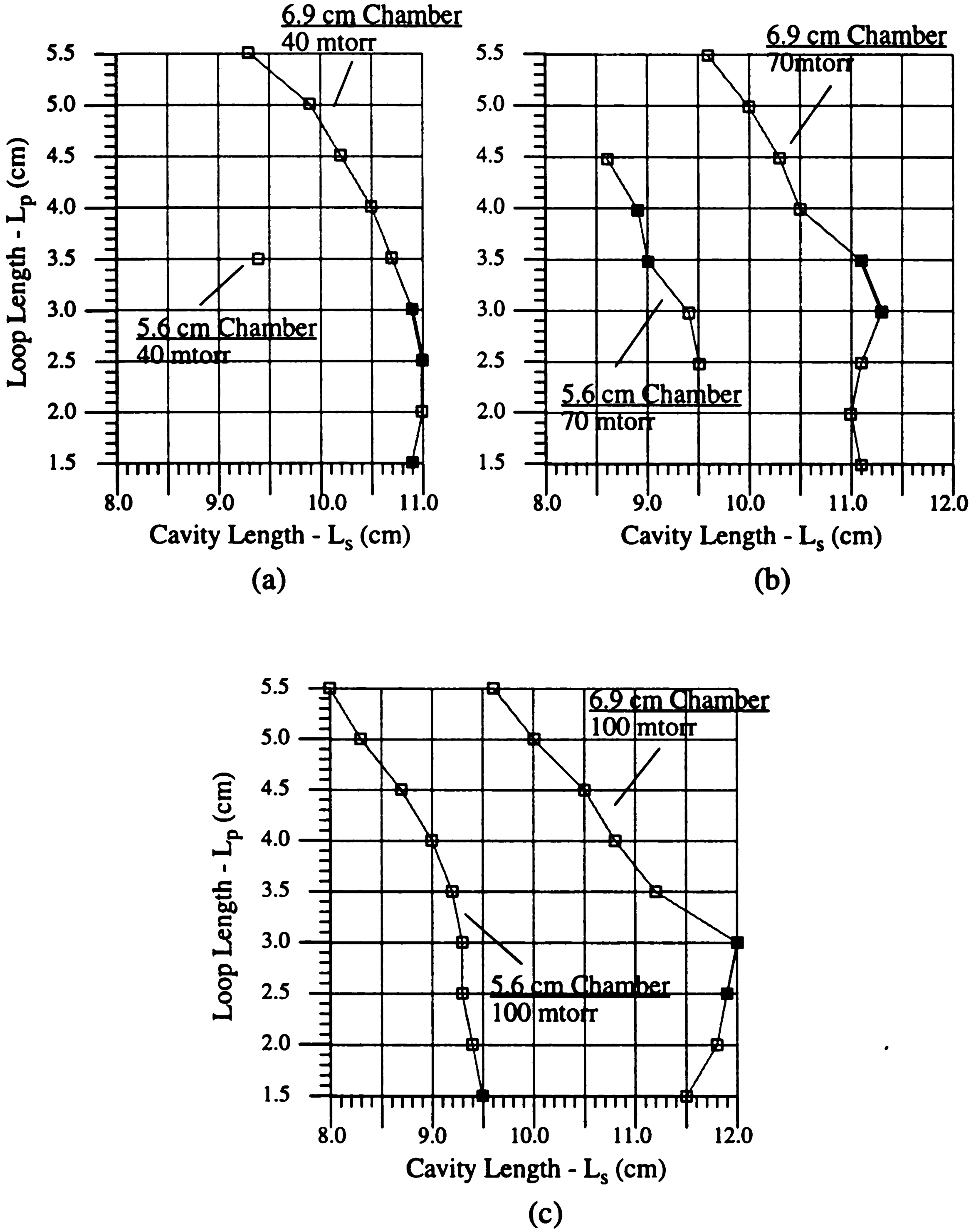

Figure 4.11 - Comparison of Cavity Lengths for the TE_{11} Mode Without Magnets vs. Discharge Chamber Height

Observation of the Low L_s mode behavior vs. change in discharge height can also be made. See Figure 4.12. At a pressure of 0.75 mtorr the Low L_s mode is observed in the 5.6 cm discharge with magnets. At a loop length of L_p = 3.5 cm the Low L_s mode cavity length is L_s = 5.2 cm. As loop length is reduced to L_p = 1.5 cm the cavity length of the Low L_s mode increases to L_s = 8.9 cm as loop length is reduced to 1.5 cm. At the same pressure in the 6.9 cm discharge (with magnets) the Low L_s mode is present at a cavity length of L_s = 5.9 cm at a loop length of L_p = 2.5 cm and moves up to a cavity length of L_s = 9.4 cm as the loop length is reduced to 1.5 cm. The average increase in mode cavity length for the Low L_s mode from the 5.6 cm discharge to the 6.9 cm discharge is approximately 0.2 cm. This is a very small change in cavity length considering that the difference in discharge chamber size is 1.3 cm. It must be noted that for the 6.9 cm tall discharge the Low L_s mode could not be observed at longer loop lengths than 5.2 cm because the discharge dome came in contact with the loop and prevented further movement of the sliding short. See Figure 4.4.

At higher pressures of 40, 70, and 100 mtorr the Low L_s mode is present in the 5.6 cm tall discharge, shown in Figure 4.9c, but it is not present in the 6.9 cm tall discharge for these pressures with or without magnets. Consequently no comparison of mode cavity length between 5.6 cm and 6.9 cm discharges can be made at these pressures.

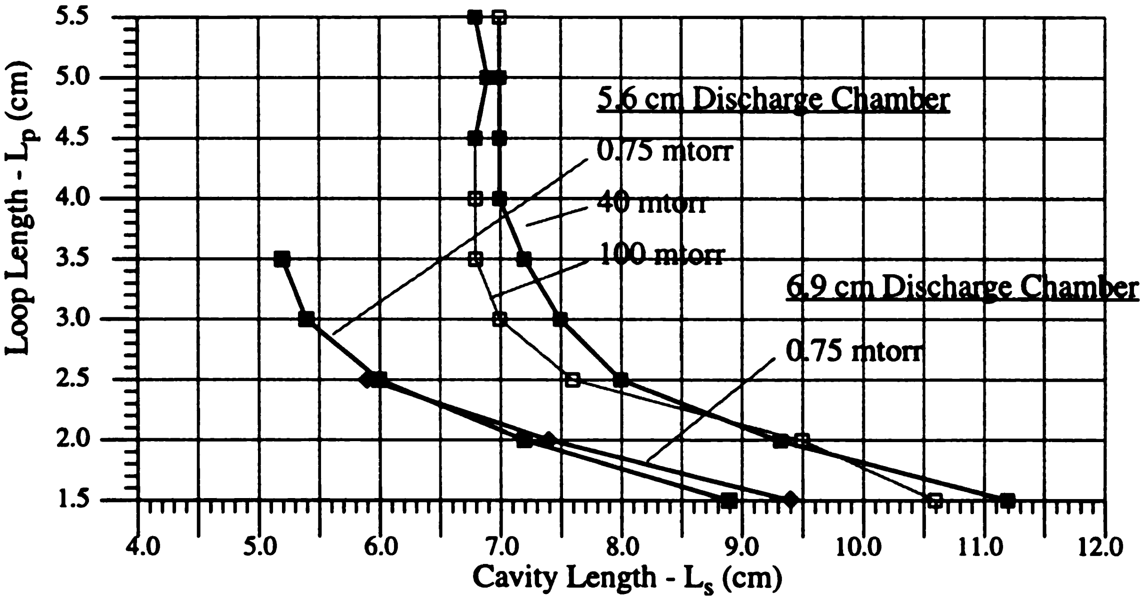

Figure 4.12 - Comparison of Cavity Lengths for the Low L_s Mode With Magnet Ring vs. Discharge Chamber Height

4.6.5 Comparison of Mode Cavity Length With and Without Magnets:

A study of the mode curve L_s position vs. the presence or absence of the multipole magnet ring can be made. Both TE_{11} and Low L_s modes were studied. Pressures of 40 mtorr and 100 mtorr were the only conditions where non-magnetized and magnetized discharges were compared, since a non-magnetized discharge could not be maintained at 0.75 mtorr.

For the TE_{11} mode at 40 mtorr in the 5.6 cm discharge, shown in Figure 4.13a, magnetic vs. non-magnetic discharges are compared. Note squares indicated magnetized mode points and triangles indicated non-magnetized mode points. Note that for this comparison only one point is available for the non-magnetized mode. Yet, it is possible to observe that this point is approximately 0.2 cm from the comparable L_p = 3.5 cm point on the magnetized mode curve. For 100 mtorr, shown in Figure 4.13b, both mode curves have very similar shape and cavity length position. For the TE_{11} mode in the 6.9 cm discharge at 40 mtorr, shown in Figure 4.13c, both magnetized and non-magnetized mode curves also show similar shape and L_s position. At 100 mtorr, shown in Figure 4.13d, both modes appear to follow the same path from loop lengths of L_p = 5.5 cm to 4.0 cm, but between L_p = 3.5 cm and 1.5 cm the non-magnetized mode curve is on average 0.4 cm higher in cavity length than the magnetized mode curve.

Magnetized vs. non-magnetized discharge comparisons can also be made with the Low L_s mode in the 5.6 cm tall discharge chamber. See Figure 4.14. At 40 mtorr only one point was observed for the non-magnetized discharge and we note that this point is 0.4 cm lower in cavity length than the comparable point on the magnetized mode curve. When

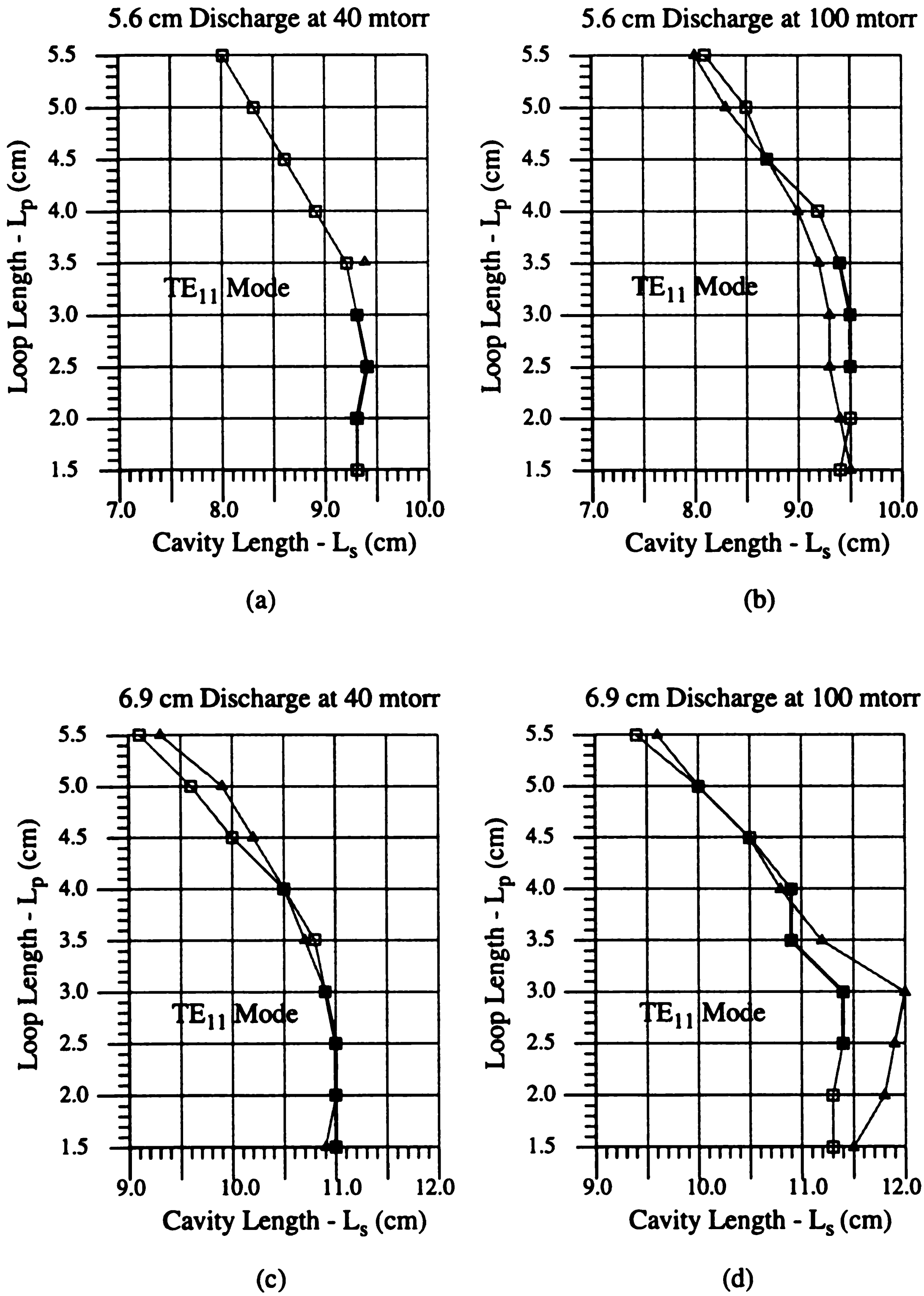

Figure 4.13 - Plots Comparing Magnetized and Non-magnetized TE_{11} Mode Curves

□ With Magnets   △ Without Magnets

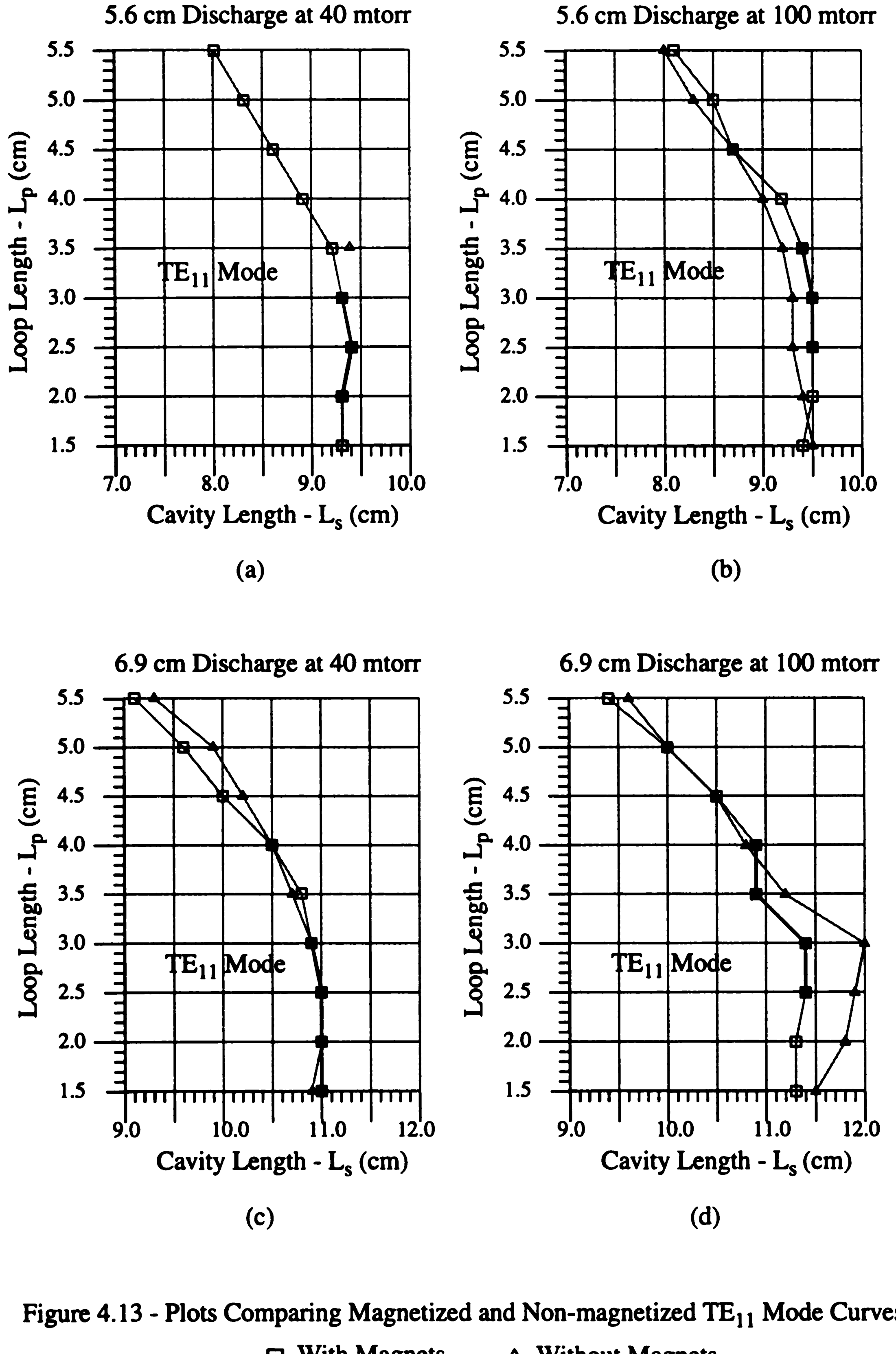

Figure 4.13 - Plots Comparing Magnetized and Non-magnetized TE_{11} Mode Curves

□ With Magnets △ Without Magnets

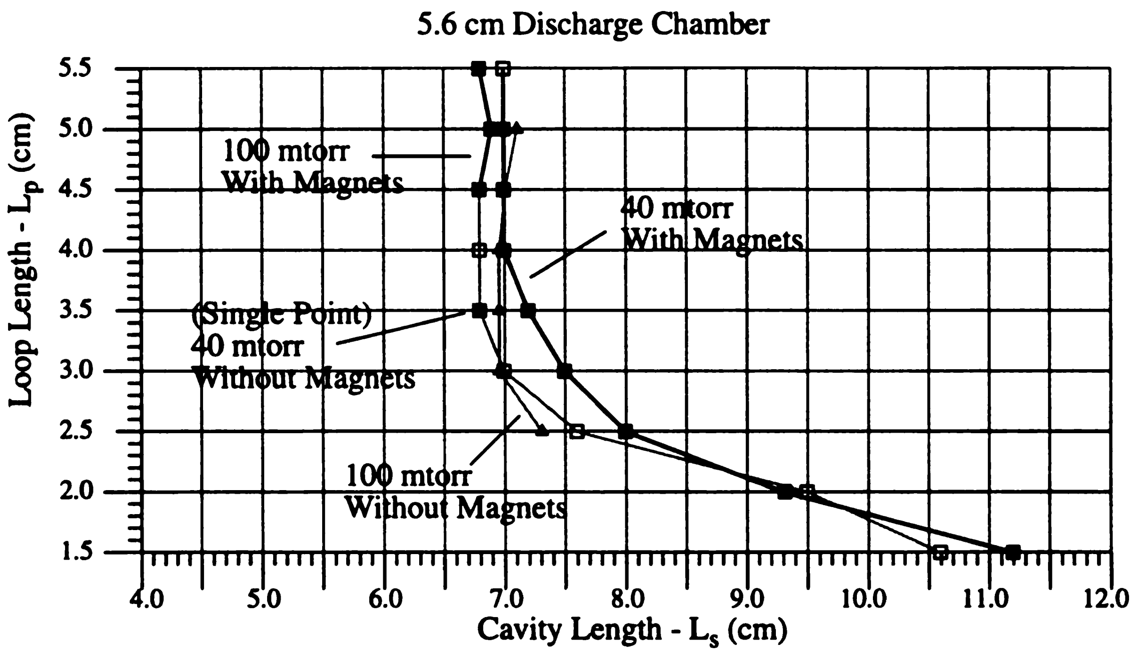

Figure 4.14 - Comparison of Magnetized and Non-Magnetized Low L_s Mode Curves

□ With Magnets   △ Without Magnets

Low L_s mode curves are compared at 100 mtorr we find that the shape and location of both magnetized and non-magnetized mode curves are similar.

4.6.6 Cavity Length Hysteresis in Reflected Power:

Hysteresis can be observed in many of the reflected power curves recorded in Figures 4.5-4.8. The most significant hysteresis is observed for 0.75 mtorr and 40 mtorr for the 6.9 cm discharge with magnets. The reflected power curves for this configuration are shown in Figures 4.6a-c. Some hysteresis is observed at 70 mtorr and 100 mtorr for the 6.9 cm discharge without magnets, in Figure 4.8a-c. Hysteresis is also observable in most of the reflected power curves for the 5.6 cm discharge without magnets, shown in Figures 4.7a-c.

Most of the hysteresis observed follows the same format: the decreasing L_s curve follows a high reflected power path and passes over a well matched point, while the increasing L_s curve follows a much lower reflected power path and at some point achieves an excellent match. In addition most increasing and decreasing curves for an individual graph follow the same path vs. L_s for the highest and lowest regions of L_s, but generally follow separate paths near a minima in the mid L_s range of the curve. This is observed, for example, in Figure 4.6b at a pressure of 0.75 mtorr and loop lengths of L_p = 3 cm, 3.5 cm, and 4.0 cm.

4.7 Summary of Important Observations:

In the investigation presented in this chapter the only internal variable measured was reflected power, P_{ref}. Measurement of reflected power was used to locate and study the behavior of resonant modes in the plasma cavity system. Input parameters varied in this study were: cavity length L_s, loop length L_p, discharge chamber height h, and magnetic field. Two important input parameters were not independently varied: incident power P_{inc}, and flow rate $\dot{r}$. Incident power was held constant at 150 Watts and flow rate was coupled to discharge pressure. Thus the data presented in this chapter should be viewed as a subset of the total data that must be obtained to fully understand the discharge behavior. However, even under the limitations of constant P_{inc} and dependent $\dot{r}$ valuable observations can still be made.

It is important to emphasize that cavity length L_s, the distance between the sliding short and the bottom of the cavity, can be considered the sum of several transmission line sections L_p, L', and L_e. In order to gain further insight into mode behavior and to develop an equivalent circuit (in Chapter 6) it will be necessary to consider L_s and its subsections

A summary of important observations made in the previous section are as follows:

<u>Electromagnetic Modes Found</u>:

- 1) The TE_{11} mode was found in all four source geometry configurations and is present for the entire pressure range investigated.

- 2) A low L_s mode was found in the 5.6 cm discharge chamber at all pressures measured, with and without magnets. In the 6.9 cm discharge the low L_s mode was only found at 0.75 mtorr with magnets, and was not observed at any pressure without magnets.

<u>General Mode Behavior</u>:

- The shape of the TE_{11} mode curve vs. L_p and L_s is different than the shape of the Low L_s mode curve.

- Low L_s mode reflected power minima appear to have more gradual magnitude of $(\Delta P_{ref}/\Delta L_s)$ slope than do the minima for the TE_{11} mode. Many TE_{11} mode minima have a very large magnitude of slope and a "sharp" appearance, while most Low L_s minima have a wider "bowl" shaped appearance.

- For all modes a decrease in loop length leads to a compensating increase in mode cavity length, L_{sm}.

- For the TE_{11} mode an increase in discharge pressure leads to an increase in mode cavity length, L_{sm}. For the Low L_s mode increase in pressure from 0.75 mtorr to 40 mtorr leads to an increase in L_{sm}, but an increase in pressure can also lead to a decrease in L_{sm} for some pressures ranges higher than 40 mtorr.

<u>Mode Behavior vs. Chamber Height</u>:

- For the TE_{11} mode an increase in discharge chamber height always results in a shift in the mode curve to larger cavity length.

- For the Low L_s mode at 0.75 mtorr an increase in discharge chamber height had very little effect on the mode cavity length. Behavior at higher pressures could not be determined conclusively.

<u>Influence of the Multipole Magnet Ring</u>:

- The presence of magnets allowed a discharge to be maintained at 0.75 mtorr (with ECR heating) whereas the lowest pressure a plasma could be maintained without magnets was 40 mtorr (non-ECR heating).

- The presence of magnets improves matching at higher pressures.

- With the magnet ring both 5.6 cm and 6.9 cm discharge chambers sustain a discharge, but without magnets the 6.9 cm discharge sustains the plasma much better than the 5.6 cm discharge.

- Presence or absence of magnets did not have a major influence on the L_s location of the mode curves. Changes in L_s observed were within the margin of experimental error (approximately 2 mm). However, at higher pressures of 40 to 100 mtorr in the 6.9 cm discharge without magnets a "bow" of increased L_s is observed for short loop lengths.

- At 100 mtorr for the 6.9 cm discharge chamber either with or without magnets the measured reflected power is 50 to 70 Watts at low loop lengths in the "off-resonance" L_s regions. For all other pressures and loop lengths the "off-resonance" reflected power is 100 Watts or more.

Hysteresis Effects Observed:

- Hysteresis is observed to a great extent in the 6.9 cm discharge with magnets, and to a lesser extent in both 5.6 cm and 6.9 cm discharges without magnets.

- Hysteresis does not exist in the 5.6 cm discharge with magnets or the 6.9 cm discharge with magnets at 100 mtorr.

- Almost all hysteresis observed is counterclockwise, i.e. the decreasing path follows a high curve while the increasing path follows a lower curve.

Conclusions drawn from the observations listed above as well as observations made in Chapter 5 will be presented in Chapter 6.

Chapter 5

Electromagnetic Evaluation of the ECR Microwave Plasma Cavity

5.1 Introduction:

There were two groups of experiments performed in this chapter. The first group was a measurement of spatial electric field patterns. The field patterns were used in to determine the specific waveguide mode present in the cavity at each resonance. Specifically the spatial electric field patterns of the two modes observed in Chapter 4. The second group of experiments performed in this chapter was a preliminary investigation of the influence of absorbed power on charge density and internal cavity electric field. Absorbed power, relative charge density, and relative electric field strength were all measured as L_s was varied and curves vs. L_s similar to the reflected power curves of Chapter 4 were obtained. Note, however, that in all experiments performed in this chapter the loop length was held constant at $L_p = 3.5$ cm.

5.2. Parameter Space:

As described in Chapter 4 the experimental variables influencing the plasma source were classified as: macroscopic controllable input variables U_1, reactor geometry variables U_2, process variables U_3, internal variables X, and output variables Y. A block

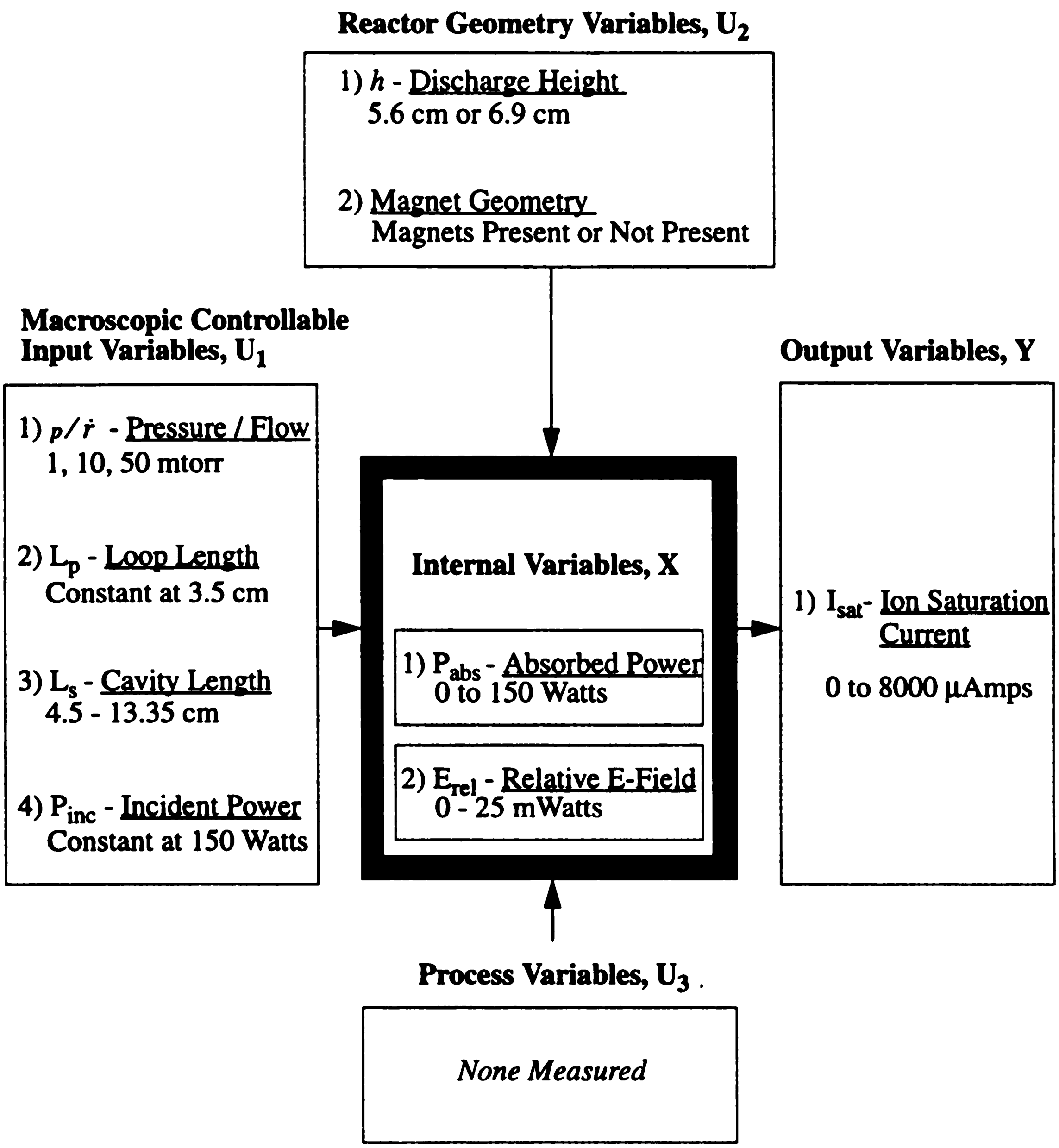

Figure 5.1 - Block Diagram of Experimental Variables

diagram of the experimental variables is shown in Fig. 5.1.

The macroscopic controllable variables were: 1) discharge pressure/flow rate, 2) loop antenna length, 3) cavity length, and 4) incident power. In this chapter discharge pressures investigated were 1, 10, and 50 mtorr where discharge pressure, p, and flow rate, $\dot{r}$, were interdependent, $p/\dot{r}$. The cavity length, L_s, was varied from 4.5 cm to 13.35 cm. The loop length, L_p, was held constant at 3.5 cm. Input power, P_{inc}, was also held constant at 150 Watts.

The discharge geometry variables were: 1) discharge height, and 2) magnet geometry. As discussed in Section 4.2, four discharge geometry configurations were investigated.

Internal variables investigated in this experiment were: 1) absorbed power, P_{abs}, and 2) relative electric field strength, E_{rel}. Absorbed power ranged from close to zero power absorbed to almost complete absorption of 150 Watts. Relative electric field strength was measured using a microwave power meter. Measured power ranged from zero Watts to 25 mWatts.

The only output variable measured in this experiment was ion saturation current, I_{sat}, which is a relative measure of plasma charge density. The currents measured in this experiment ranged from 0 to 8000 microampere. Process variables were not measured in this investigation.

5.3 Start-up Procedure and Experimental Setup:

The experimental start-up procedure for this set of experiments is the same as that discussed in Section 4.3. The basic experimental setup is also similar except that two measurement devices were added. A diagram of the experimental setup is shown in Figure 5.2.

A microcoaxial electric field probe (1) was used to measure relative electric field strength and electric field patterns. Power coupled into to microcoaxial dipole antenna was measured by a Hewlet Packard power meter (2) with a thermistor (3) used to convert microwave power to a DC signal.

A double Langmuir probe (4) was placed approximately 1 cm below the ECR magnet ring (5) at the circular opening of the discharge chamber (6). The Langmuir probe was electrically connected to the measurement circuit (7) through an electrical feed through (8) in the vacuum chamber wall. The measurement circuitry is described in detail in Section 5.4.2.

Microwave power was delivered to the plasma source with the same microwave network (9) as used in Chapter 4 and the same method of measuring reflected power (10) was used.

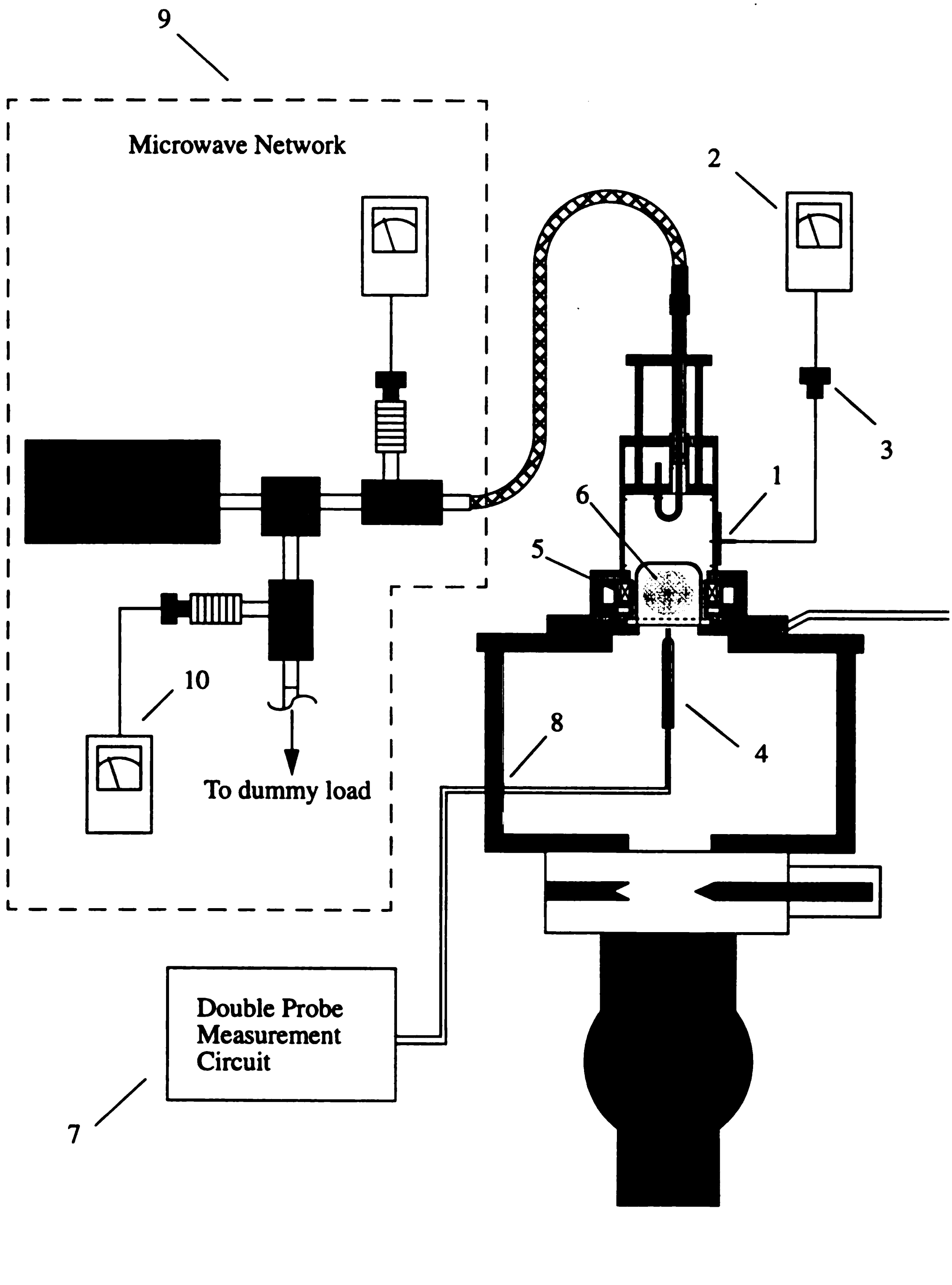

Figure 5.2 - Experimental Setup for Source Evaluation

5.4 Experimental Procedure:

5.4.1 Relative Measurement of Electric Field:

Relative measurements of electric field were taken with a microcoaxial probe. A cross-sectional diagram of an electric field probe is shown in Figure 5.3. It was constructed from 5 to 7 cm sections of 3 mm diameter flexible copper coaxial stock (1) obtained from Pasternack, Inc. One end of each stock section was soldered to an SMA connector (2). Two millimeters of the copper shielding was carefully cut away from the other end. The dielectric (3) surrounding the center conductor was not cut away in order to provide a mechanical shield and prevent the accidental bending of the center conductor (4). The extension of the center conductor into the cavity forms a 2 mm long dipole antenna.

When inserted into small holes in the wall of the cavity this probe acts as a dipole antenna, coupling to the radial time varying fields normal to the wall of the cavity. See Figure 5.4. The microwave power absorbed by the probe was measured by a themistor (1) aided Hewlet Packard microwave power meter (2). Since electric field strength is proportional to the square root of microwave power the measurement of microwave power was used as a relative measurement of radial electric filed strength.

Figure 5.3 - Cross Sectional Diagram of a Microcoaxial Electric Field Probe

As shown in the inset of Figure 5.4, the inner wall of the cavity (3) acts as the ground plane of the dipole (4). In order to maintain consistent depth of extension into the cavity an adjustable brass collar (5) was placed on the probe [18]. This also ensures that the end of the copper outer conductor is flush with the inner wall of the cavity. When a measurement is made the probe is inserted into a probe hole in the cavity until the collar makes full contact with the outer wall of the cavity.

To accommodate the above described E-field probe many 3mm diameter holes were drilled into the side walls of the cavity. In order to measure the ϕ variation of radial E-fields three circumferential rings of holes (with holes spaced 10° apart) were drilled at planes 1 inch (2.54 cm), 2 inches (5.08 cm), and 3 inches (7.62 cm) from the bottom of the cavity. These can be seen clearly in the photograph in Figure 2.5 in Chapter 2. A cross sectional diagram of the circumferential ring of holes at 2 inches from the bottom of the cavity is shown in Figure 5.5. A zero degree reference point is chosen at the center of the screened window (1). The plane of the coupling loop (2) is the plane that passes through both 90° and 270° sampling holes.

In order to measure the variation of radial E-field along the length of the cavity four linear groups of holes were drilled at 0°, 90°, 180°, and 270° around the circumference with reference to the screened window at 0°. These can also be seen clearly in the photograph in Figure 2.5 in Chapter 2. The first hole of each line was placed at 0.75 inches (1.905 cm) from the bottom of the cavity. Holes were drilled at 0.25 inch (0.635 cm) intervals up to 4.25 inches (10.795 cm) from the bottom of the cavity. A 3/16" (0.476 cm) thick stainless steel strip was welded to the outside of the cavity at each line and ring of holes. These strips were used to provide larger hole depth in order to increase electrical contact

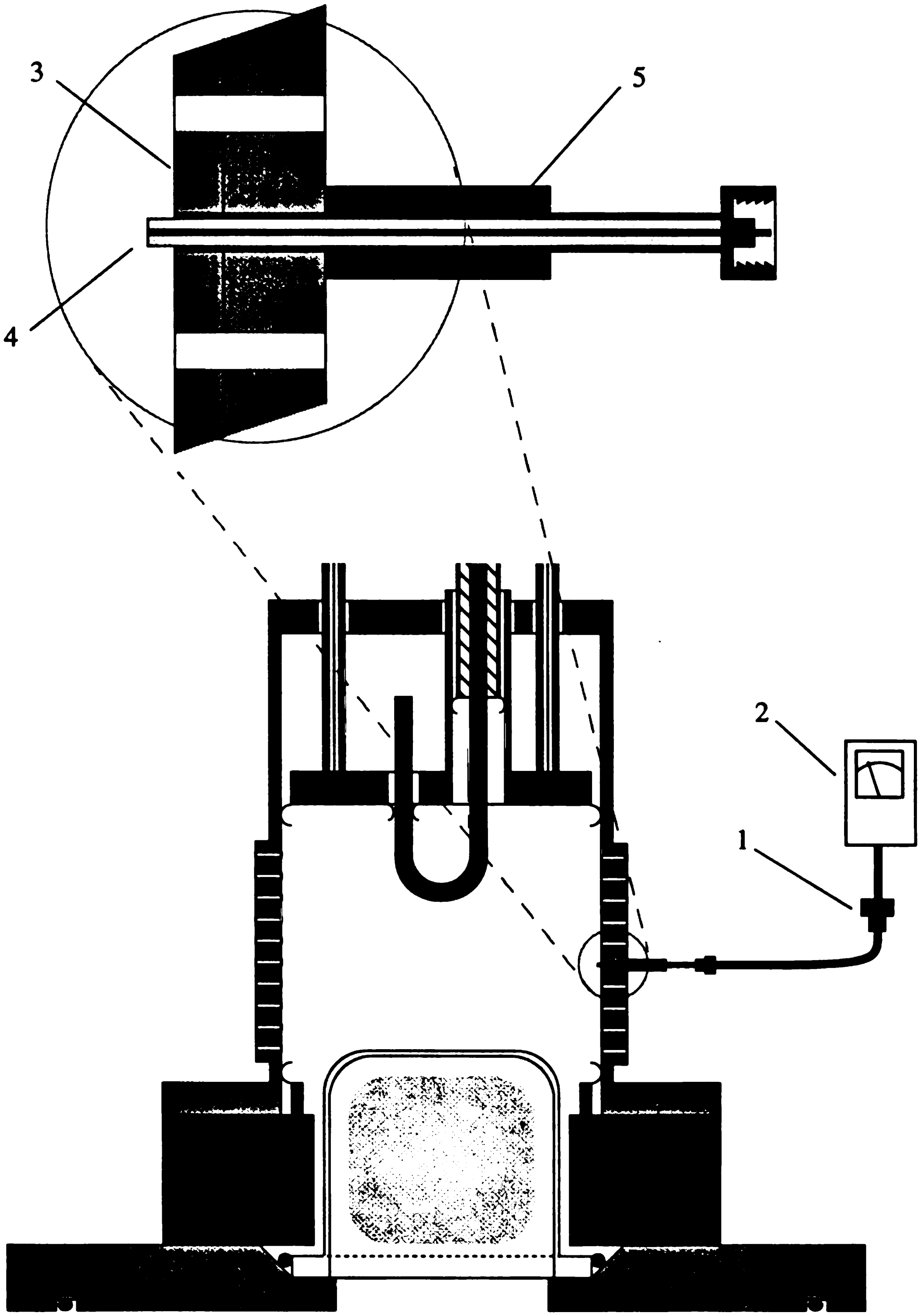

Figure 5.4 - Measurment of Electric Field Strength

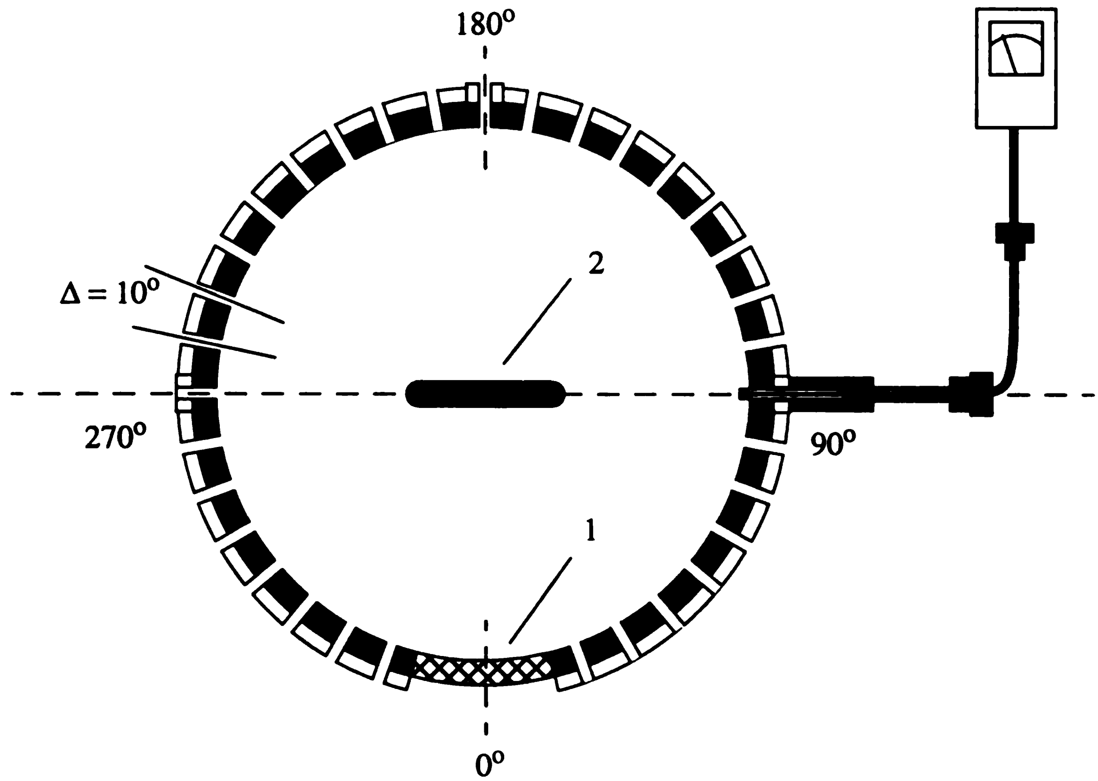

Figure 5.5 - Cross-Section of a Circumferential Ring of E-Field Sampling Holes

and to ensure that the probes would fit securely and not wobble while measurements were performed.

Electric field measurements were taken in two types of experimental procedures. The first procedure was intended to determine cavity mode patterns and the second was to measure relative electric fields in the cavity vs. L_s. This relative electric field measurement was part of the correlated measurement of absorbed power, relative charge density and relative electric field strength vs. L_s.

In order to determine the electromagnetic modes present in the cavity the spatial variation of radial electric fields was investigated. In this procedure all parameters of the plasma source, such as L_s, L_p, input power, and discharge pressure, etc., were held constant. The microwave power (relative electric field strength) was then measured at each probe hole around the cavity. These measurements were then plotted vs. circumferential angle or longitudinal distance. These curves facilitated the identification of the electromagnetic mode present in the cavity.

The second experimental procedure involved the measurement of relative electric field strength as the sliding short position L_s was varied. A microcoaxial electric field probe was placed and kept at one sampling hole 90^o from the center of the screened window and 2 inches from the bottom of the cavity. Periodic readings were taken from the electric field probe at this constant sampling position as the sliding short was lowered and then raised. All input variables other than L_s were held constant. Note, since electric field patterns may be different for different modes accessed by varying L_s one to one comparisons of field strength from one mode to the next may not be possible for this fixed sample. However, the relative E-field vs. L_s curves make it possible to identify positions of L_s where E-field is significant and observable. They also make it possible to make comparisons between absorbed power, relative charge density, and relative electric field strength when all are varied vs. L_S.

5.4.2 Measurement of Absorbed Power:

Power absorbed by the plasma cavity system is calculated from measurements of reflected power. A reflected power curve is first taken by measuring reflected power while varying the cavity length L_S and holding loop length, discharge pressure and forward power constant. An example reflected power curve is shown in Figure 5.6a. The absorbed power curve is obtained by subtracting the reflected power curve from the value of incident power (150 Watts in this investigation). Such an absorbed power curve is shown in Figure 5.6b. The regions of good matching and low reflected power appear as minima in

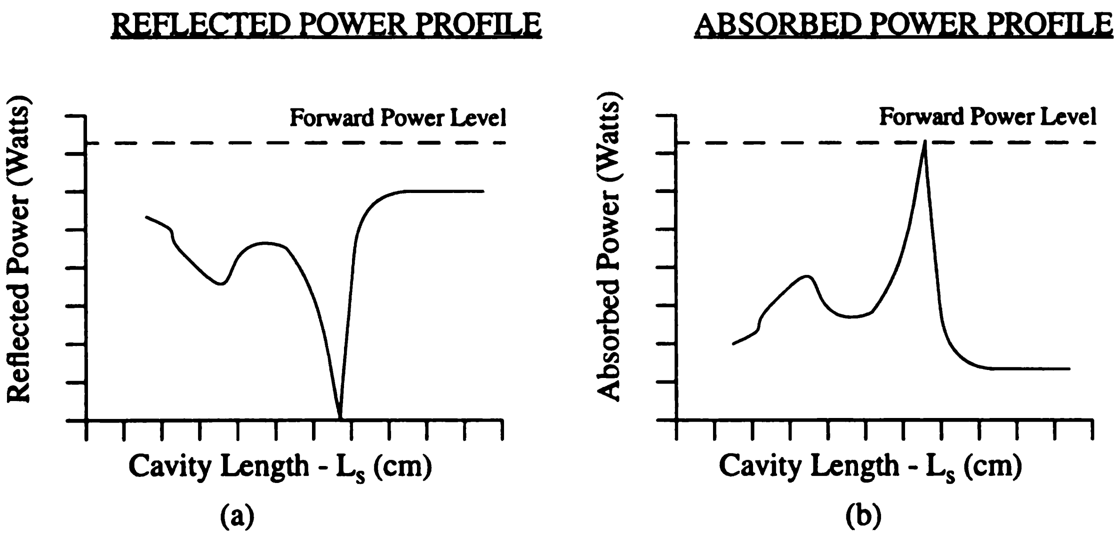

Figure 5.6 - Reflected and Absorbed Power Profiles

the reflected power curve and as maxima in the absorbed power curve. The presentation of reflected power curves as absorbed power curves facilitates their comparison with relative charge density and relative electric field curves vs. L_S. Note the total power absorbed in the plasma source is the sum of the power absorbed by: the cavity walls, the coupling antenna, and the plasma discharge.

5.4.3 Relative Measurement of Charge Density:

Ion saturation current was measured vs. L_s at the same time absorbed power was measured vs. L_S. These simultaneous measurements allowed relative charge density vs. L_s curves to be plotted and compared with absorbed power vs. L_s curves. The ion saturation current vs. L_s curves also indicated the values of L_s for specific discharge geometries and pressures where the charge density was highest.

Ion saturation current measured by a double Langmuir probe at a fixed bias voltage (40 Volts in this experiment) can be used to provide a quick relative measurement of charge species density. Ion saturation current, I_{sat}, is related to charged species density, n_i, through the approximate relation [26]:

$$I_{sat} \cong 0.6 n_i e A \sqrt{\left(\frac{kT_e}{m_i}\right)}$$

where 0.6 is a constant of proportionality, e is the charge on an electron, A is the area of the probe, k is Boltzman's constant, m_i is the mass of an Argon ion, and T_e is the electron temperature. Since e, A, k, and m_i are normally constant then direct proportionality between I_{sat} and n_i is only possible if electron temperature, T_e, is held constant. Electron temperature is controlled by: discharge gas composition, discharge pressure, and discharge geometry. If each of these three parameters are held constant then I_{sat} can be used as an indicator of n_i as other parameters such as input power and microwave matching are varied. Therefore, the measurements of I_{sat} vs. L_s in this experiment strongly indicate the relative variation of n_i vs. L_s. Note that the area of the DC sheath surrounding the probes (i.e. the effective collection area) may change with changing n_i introducing a small source of error into the relative measurements. Nonetheless this method is a good general indicator of relative charge density.

Note also that ion saturation current measurements alone can not be used to determine absolute charge density. A current vs. voltage curve must be obtained to make absolute charge density measurements.

A diagram of the setup used to make ion saturation current measurements is shown in Figure 5.7. The double Langmuir probe (1) was mounted along the central axis of the plasma source with the tips of the probes 1 cm from the bottom of the ECR magnet ring (2). The Langmuir probe was constructed from two 0.95 mm diameter Tungsten rods (3) encased in fused quartz (4) with 0.9 cm of the Tungsten rods exposed to form the probes. The double probe was connected through a electrical vacuum feedthrough (5) to the measurement circuit outside the vacuum chamber. The measurement circuit consisted of two digital multimeters and a floating DC power supply. The power supply was set to 40 Volts and held constant throughout the experiment. DMM #2 was used as a volt meter to monitor voltage produced by the DC power supply. DMM #1 was used as an ammeter and measured the current flowing through the double probe. The current measured by DMM #1 was defined as the ion saturation current.

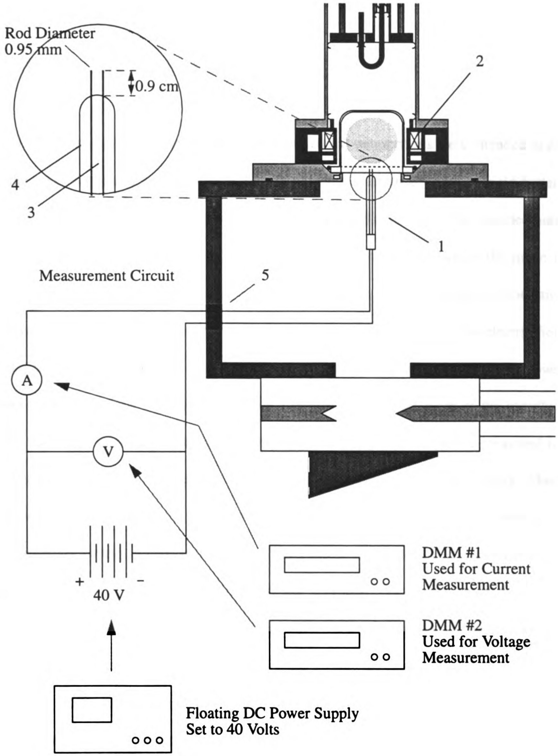

Figure 5.7 - Setup for Measurement of Ion Saturation Current

5.5 Spatial Electric Field Patterns:

5.5.1 Description of the Experiment:

The field pattern measurements presented in the next two sections were intended to aid in the identification of the two mode like phenomena noted in Chapter 4. Field pattern measurements were taken by first striking the discharge and adjusting to the intended pressure. Then the sliding short was tuned to the specific cavity length where the mode in question was observed and the plasma source was perfectly matched. When this condition was reached all input parameters were then held constant. At this point the electric field probe was inserted into each of the appropriate E-field sampling holes and the power absorbed by the probe was recorded. Once a power reading from each of the sampling holes was obtained the field pattern measurement was complete. The power measured for each sampling hole was then plotted vs. circumferential and longitudinal distance. These plots are presented in the next two sections. Field pattern measurements were taken in all four source geometry configurations for the TE_{11} mode, while pattern measurements with the Low L_s mode were only taken in the two configurations with the 5.6 cm discharge.

It is important to note that all field pattern plots display power coupled into the probe. This power is proportional to the square of electric field. Thus these plots should be viewed as plotting the square of relative electric field.

Also, note that the objective of these experiments is to determine relative field patterns and not absolute field strength. At the beginning of each field pattern measurement the depth of the probe was optimized to provide the best resolution of field pattern. This measurement devices were added. A diagram of the experimental setup is shown in Figure 5.2.

A microcoaxial electric field probe (1) was used to measure relative electric field strength and electric field patterns. Power coupled into to microcoaxial dipole antenna was measured by a Hewlet Packard power meter (2) with a thermistor (3) used to convert microwave power to a DC signal.

A double Langmuir probe (4) was placed approximately 1 cm below the ECR magnet ring (5) at the circular opening of the discharge chamber (6). The Langmuir probe was electrically connected to the measurement circuit (7) through an electrical feed through (8) in the vacuum chamber wall. The measurement circuitry is described in detail in Section 5.4.2.

Microwave power was delivered to the plasma source with the same microwave network (9) as used in Chapter 4 and the same method of measuring reflected power (10) was used.

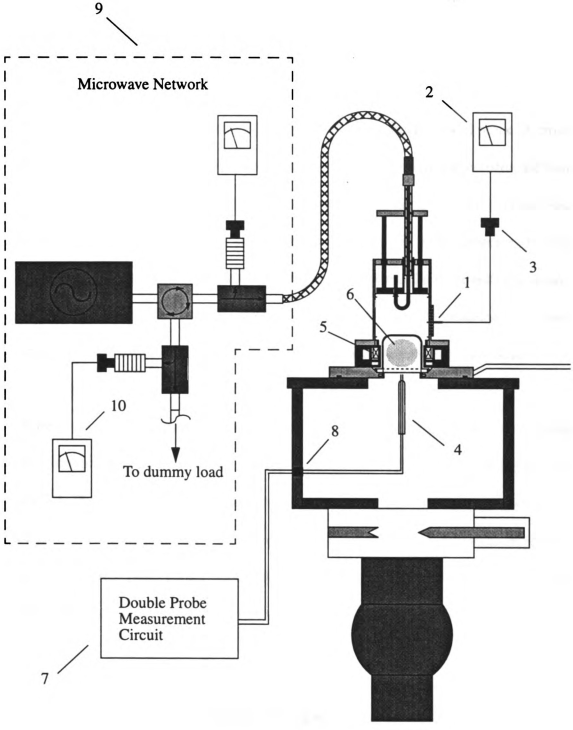

Figure 5.2 - Experimental Setup for Source Evaluation

5.4 Experimental Procedure:

5.4.1 Relative Measurement of Electric Field:

Relative measurements of electric field were taken with a microcoaxial probe. A cross-sectional diagram of an electric field probe is shown in Figure 5.3. It was constructed from 5 to 7 cm sections of 3 mm diameter flexible copper coaxial stock (1) obtained from Pasternack, Inc. One end of each stock section was soldered to an SMA connector (2). Two millimeters of the copper shielding was carefully cut away from the other end. The dielectric (3) surrounding the center conductor was not cut away in order to provide a mechanical shield and prevent the accidental bending of the center conductor (4). The extension of the center conductor into the cavity forms a 2 mm long dipole antenna.

When inserted into small holes in the wall of the cavity this probe acts as a dipole antenna, coupling to the radial time varying fields normal to the wall of the cavity. See Figure 5.4. The microwave power absorbed by the probe was measured by a themistor (1) aided Hewlet Packard microwave power meter (2). Since electric field strength is proportional to the square root of microwave power the measurement of microwave power was used as a relative measurement of radial electric filed strength.

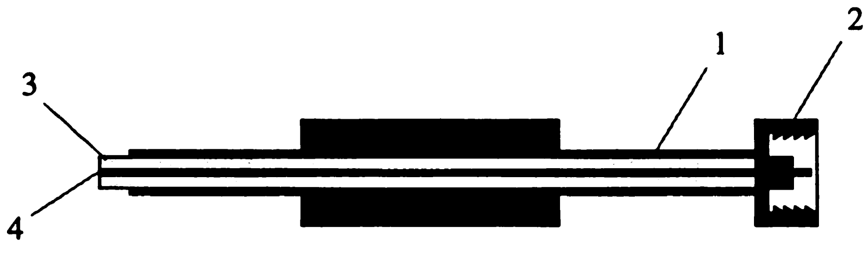

Figure 5.3 - Cross Sectional Diagram of a Microcoaxial Electric Field Probe

As shown in the inset of Figure 5.4, the inner wall of the cavity (3) acts as the ground plane of the dipole (4). In order to maintain consistent depth of extension into the cavity an adjustable brass collar (5) was placed on the probe [18]. This also ensures that the end of the copper outer conductor is flush with the inner wall of the cavity. When a measurement is made the probe is inserted into a probe hole in the cavity until the collar makes full contact with the outer wall of the cavity.

To accommodate the above described E-field probe many 3mm diameter holes were drilled into the side walls of the cavity. In order to measure the ϕ variation of radial E-fields three circumferential rings of holes (with holes spaced 10° apart) were drilled at planes 1 inch (2.54 cm), 2 inches (5.08 cm), and 3 inches (7.62 cm) from the bottom of the cavity. These can be seen clearly in the photograph in Figure 2.5 in Chapter 2. A cross sectional diagram of the circumferential ring of holes at 2 inches from the bottom of the cavity is shown in Figure 5.5. A zero degree reference point is chosen at the center of the screened window (1). The plane of the coupling loop (2) is the plane that passes through both 90° and 270° sampling holes.

In order to measure the variation of radial E-field along the length of the cavity four linear groups of holes were drilled at 0°, 90°, 180°, and 270° around the circumference with reference to the screened window at 0°. These can also be seen clearly in the photograph in Figure 2.5 in Chapter 2. The first hole of each line was placed at 0.75 inches (1.905 cm) from the bottom of the cavity. Holes were drilled at 0.25 inch (0.635 cm) intervals up to 4.25 inches (10.795 cm) from the bottom of the cavity. A 3/16" (0.476 cm) thick stainless steel strip was welded to the outside of the cavity at each line and ring of holes. These strips were used to provide larger hole depth in order to increase electrical contact

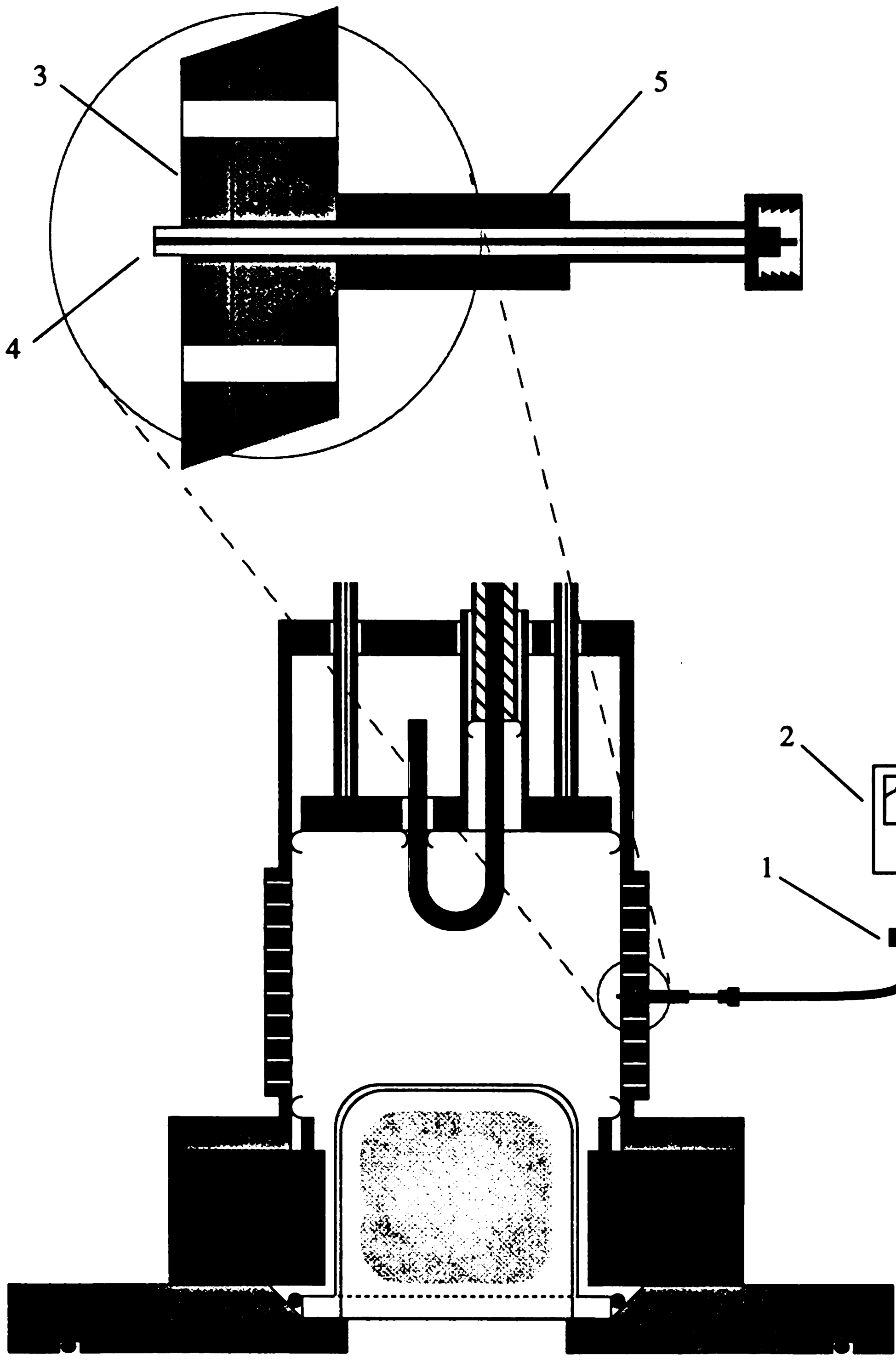

Figure 5.4 - Measurment of Electric Field Strength

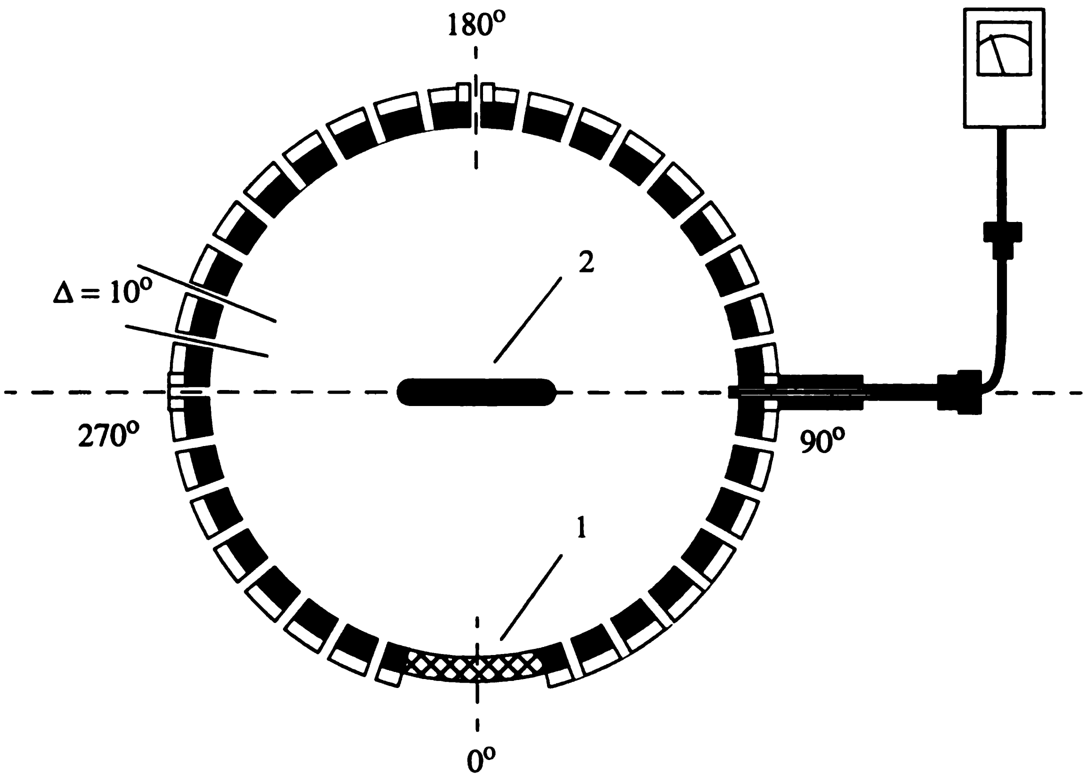

Figure 5.5 - Cross-Section of a Circumferential Ring of E-Field Sampling Holes

and to ensure that the probes would fit securely and not wobble while measurements were performed.

Electric field measurements were taken in two types of experimental procedures. The first procedure was intended to determine cavity mode patterns and the second was to measure relative electric fields in the cavity vs. L_S. This relative electric field measurement was part of the correlated measurement of absorbed power, relative charge density and relative electric field strength vs. L_S.

In order to determine the electromagnetic modes present in the cavity the spatial variation of radial electric fields was investigated. In this procedure all parameters of the plasma source, such as L_s, L_p, input power, and discharge pressure, etc., were held constant. The microwave power (relative electric field strength) was then measured at each probe hole around the cavity. These measurements were then plotted vs. circumferential angle or longitudinal distance. These curves facilitated the identification of the electromagnetic mode present in the cavity.

The second experimental procedure involved the measurement of relative electric field strength as the sliding short position L_s was varied. A microcoaxial electric field probe was placed and kept at one sampling hole 90^o from the center of the screened window and 2 inches from the bottom of the cavity. Periodic readings were taken from the electric field probe at this constant sampling position as the sliding short was lowered and then raised. All input variables other than L_s were held constant. Note, since electric field patterns may be different for different modes accessed by varying L_s one to one comparisons of field strength from one mode to the next may not be possible for this fixed sample. However, the relative E-field vs. L_s curves make it possible to identify positions of L_s where E-field is significant and observable. They also make it possible to make comparisons between absorbed power, relative charge density, and relative electric field strength when all are varied vs. L_S.

5.4.2 Measurement of Absorbed Power:

Power absorbed by the plasma cavity system is calculated from measurements of reflected power. A reflected power curve is first taken by measuring reflected power while varying the cavity length L_S and holding loop length, discharge pressure and forward power constant. An example reflected power curve is shown in Figure 5.6a. The absorbed power curve is obtained by subtracting the reflected power curve from the value of incident power (150 Watts in this investigation). Such an absorbed power curve is shown in Figure 5.6b. The regions of good matching and low reflected power appear as minima in

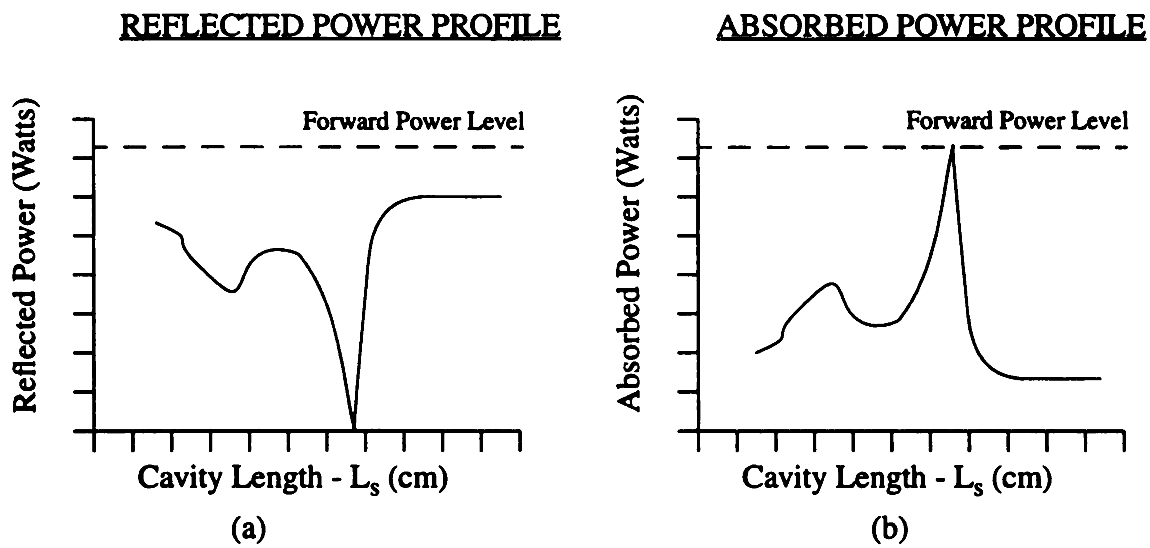

Figure 5.6 - Reflected and Absorbed Power Profiles

the reflected power curve and as maxima in the absorbed power curve. The presentation of reflected power curves as absorbed power curves facilitates their comparison with relative charge density and relative electric field curves vs. L_s. Note the total power absorbed in the plasma source is the sum of the power absorbed by: the cavity walls, the coupling antenna, and the plasma discharge.

5.4.3 Relative Measurement of Charge Density:

Ion saturation current was measured vs. L_s at the same time absorbed power was measured vs. L_s. These simultaneous measurements allowed relative charge density vs. L_s curves to be plotted and compared with absorbed power vs. L_s curves. The ion saturation current vs. L_s curves also indicated the values of L_s for specific discharge geometries and pressures where the charge density was highest.

Ion saturation current measured by a double Langmuir probe at a fixed bias voltage (40 Volts in this experiment) can be used to provide a quick relative measurement of charge species density. Ion saturation current, I_{sat}, is related to charged species density, n_i, through the approximate relation [26]:

$$I_{sat} \cong 0.6 n_i e A \sqrt{\left(\frac{kT_e}{m_i}\right)}$$

where 0.6 is a constant of proportionality, e is the charge on an electron, A is the area of the probe, k is Boltzman's constant, m_i is the mass of an Argon ion, and T_e is the electron temperature. Since e, A, k, and m_i are normally constant then direct proportionality between I_{sat} and n_i is only possible if electron temperature, T_e, is held constant. Electron temperature is controlled by: discharge gas composition, discharge pressure, and discharge geometry. If each of these three parameters are held constant then I_{sat} can be used as an indicator of n_i as other parameters such as input power and microwave matching are varied. Therefore, the measurements of I_{sat} vs. L_s in this experiment strongly indicate the relative variation of n_i vs. L_s. Note that the area of the DC sheath surrounding the probes (i.e. the effective collection area) may change with changing n_i introducing a small source of error into the relative measurements. Nonetheless this method is a good general indicator of relative charge density.

Note also that ion saturation current measurements alone can not be used to determine absolute charge density. A current vs. voltage curve must be obtained to make absolute charge density measurements.

A diagram of the setup used to make ion saturation current measurements is shown in Figure 5.7. The double Langmuir probe (1) was mounted along the central axis of the plasma source with the tips of the probes 1 cm from the bottom of the ECR magnet ring (2). The Langmuir probe was constructed from two 0.95 mm diameter Tungsten rods (3) encased in fused quartz (4) with 0.9 cm of the Tungsten rods exposed to form the probes. The double probe was connected through a electrical vacuum feedthrough (5) to the measurement circuit outside the vacuum chamber. The measurement circuit consisted of two digital multimeters and a floating DC power supply. The power supply was set to 40 Volts and held constant throughout the experiment. DMM #2 was used as a volt meter to monitor voltage produced by the DC power supply. DMM #1 was used as an ammeter and measured the current flowing through the double probe. The current measured by DMM #1 was defined as the ion saturation current.

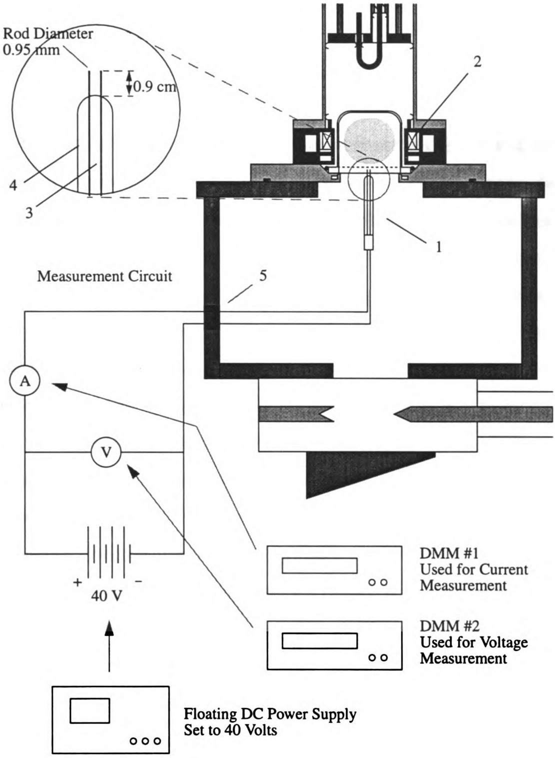

Figure 5.7 - Setup for Measurement of Ion Saturation Current

5.5 Spatial Electric Field Patterns:

5.5.1 Description of the Experiment:

The field pattern measurements presented in the next two sections were intended to aid in the identification of the two mode like phenomena noted in Chapter 4. Field pattern measurements were taken by first striking the discharge and adjusting to the intended pressure. Then the sliding short was tuned to the specific cavity length where the mode in question was observed and the plasma source was perfectly matched. When this condition was reached all input parameters were then held constant. At this point the electric field probe was inserted into each of the appropriate E-field sampling holes and the power absorbed by the probe was recorded. Once a power reading from each of the sampling holes was obtained the field pattern measurement was complete. The power measured for each sampling hole was then plotted vs. circumferential and longitudinal distance. These plots are presented in the next two sections. Field pattern measurements were taken in all four source geometry configurations for the TE_{11} mode, while pattern measurements with the Low L_s mode were only taken in the two configurations with the 5.6 cm discharge.

It is important to note that all field pattern plots display power coupled into the probe. This power is proportional to the square of electric field. Thus these plots should be viewed as plotting the square of relative electric field.

Also, note that the objective of these experiments is to determine relative field patterns and not absolute field strength. At the beginning of each field pattern measurement the depth of the probe was optimized to provide the best resolution of field pattern. This optimization was dictated by two concerns: 1) providing enough probe length to couple to the weakest fields, and 2) ensuring that the highest field measurements did not exceed the power limit of the probe and thermistor (30 mWatts).Therefore in the field graphs presented any apparent increase in coupled power from one discharge pressure or configuration to the next should not be taken as evidence, for example, that E-field strength increases with discharge pressure. This kind of observation can only be made with absolute measurements of electric field strength. These measurements will be made in future investigations of this source.

5.5.2 Identification of the TE_{11} Mode:

Electric field pattern measurements for the TE_{11} Mode were performed for the configurations and pressures listed in Table 5.1 below:

Table 5.1 - Summary of the Discharge Pressures Investigated in the Evaluation of the Spatial Electric Fields of the TE_{11} Mode

5.6 cm Discharge with ECR Magnets	6.9 cm Discharge with ECR Magnets	5.6 cm Discharge without Magnets	6.9 cm Discharge without Magnets
1 mtorr	1 mtorr	--	--
10 mtorr	10 mtorr	--	--
50 mtorr	50 mtorr	50 mtorr	50 mtorr

Note that a discharge could not be maintained at 150 Watts for pressures of 1 mtorr and 10 mtorr for the configurations without magnets.

For the 5.6 cm discharge with magnets at a discharge pressure of 1 mtorr the field pattern measurements taken are shown in Figures 5.8 and 5.9.

In Figure 5.8 circumferential variance of radial electric fields is plotted. The data points marked by squares were taken from the ring of E-field sampling holes 5.08 cm from the bottom of the cavity. Data points marked with diamonds were taken from the ring of sampling holes 2.54 cm from the bottom of the cavity. These rings of sampling holes can be seen clearly in the photograph in Figure 2.5. There are three rings in total: one at 2.54 cm from the bottom of the cavity, the second at 5.08 cm from the bottom (shown interrupted by the screen window), and the third at 7.62 cm from the bottom. Fields could not be sampled from the third ring in Figure 5.8 because the sliding short obstructed the region of these holes.

It can be seen, in Figure 5.8, that both groups of data points follow a double lobe pattern. The peak of the first lobe occurs at 100^o from the center of the screened window. The peak of the second lobe occurs at 280^o a difference of 180^o from the first lobe. This type of circumferential field pattern is strongly indicative of a TE_{111} type cavity mode, shown in Figure 3.10a. The maxima of the lobes are very close to the plane of the coupling loop (the 90^o 270^o plane) which is what would be expected for a TE_{111} mode. In this case, magnetic fields couple through the loop and induce electric fields in the central volume of the cavity that are parallel to the plane of the loop.

Note that the lobes centered at 100^o have a higher peak than the lobes centered at 280^o. This is explained by the fact that the thickness of the cavity wall was found to be 14 mills (or 0.36 mm) thicker in the 280° region than the 100° region. In regions where the wall is thicker the probe does not penetrate as far into the cavity volume. This reduces the amount of power absorbed by the probe and causes field readings to appear lower than for readings taken at thinner areas of the wall.

In Figure 5.9 longitudinal variance of radial electric fields are plotted. These data points were taken from the linear group of sampling holes 90° from the center of the screened window. This linear group of holes can be seen at the right side of the cavity in the photograph in Figure 2.5. This curve shows an approximate half wave sinusoidal dependence that is consistent with the radial electric fields of a TE_{111} cavity mode. Parallel electric fields must approach zero at a conducting surface, and hence the radial electric fields measured at the cylindrical wall must be to zero at each end of the cavity.

Figures 5.10, 5.11, 5.12, and 5.13 show similar field patterns for the same configuration at the higher pressures of 10 mtorr and 50 mtorr. Figures 5.10 and 5.12 display two lobes in the circumferential variation similar to Figure 5.8. Figures 5.11 and 5.13 show a half wave sinusoidal dependence in the longitudinal variation similar to Figure 5.9. These plots are all consistent with field patterns in the TE_{111} cavity mode.

The next six Figures present the field pattern measurements for a different source configuration: the 6.9 cm discharge with magnets. Figures 5.14 and 5.15 present the field patterns for this configuration at 1 mtorr. Figures 5.16 and 5.17 present field patterns for 10 mtorr. Figures 5.18 and 5.19 present field patterns for 50 mtorr. All circumferential plots, Figures 5.14, 5.16, and 5.18, demonstrate a two lobe structure consistent with the TE_{111} mode field pattern. All longitudinal plots, Figures 5.15, 5.17, and 5.19, demonstrate a half wave sinusoidal structure. In Figures 5.20 and 5.21 the field patterns are presented for the

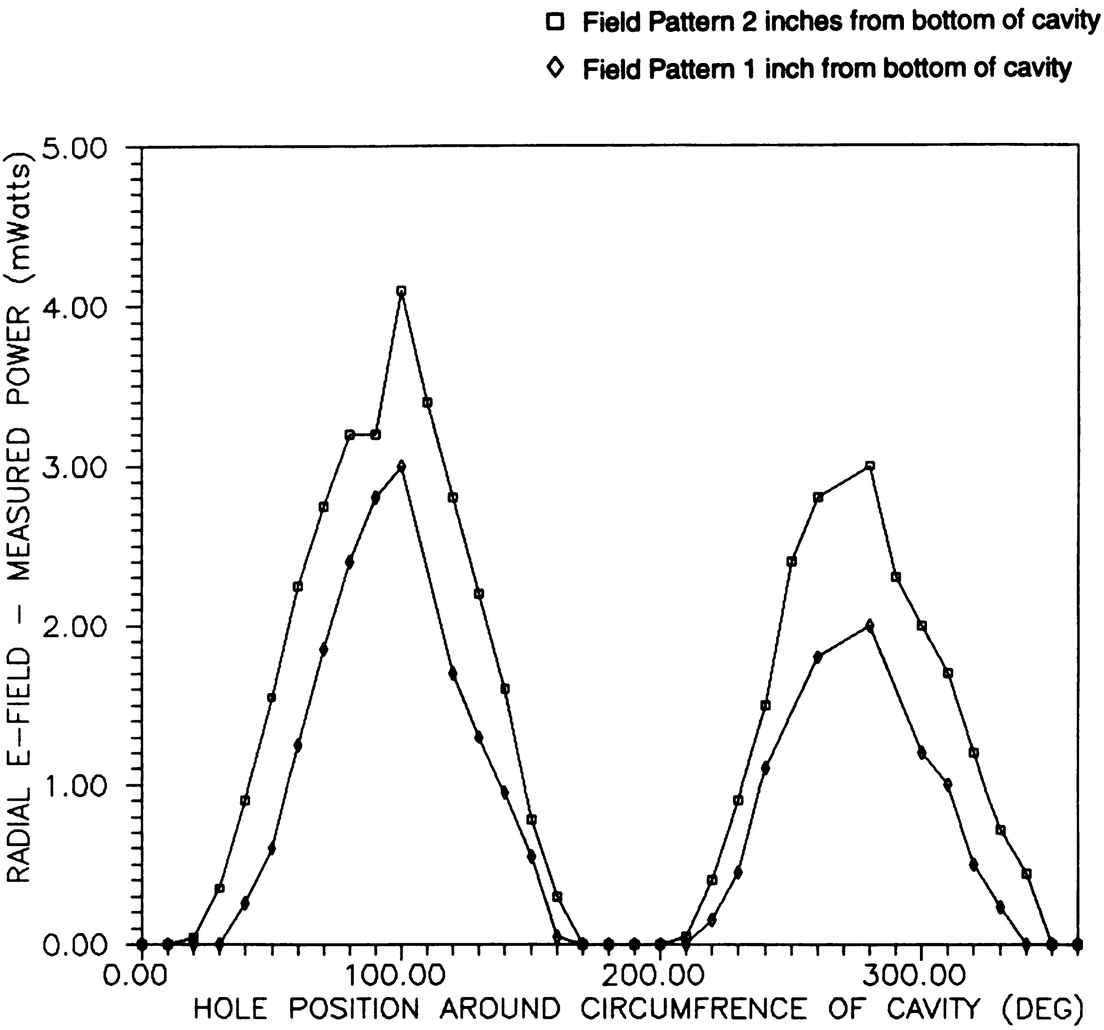

Input Power: 150 Watts
Reflected Power: 4.5 Watts

Discharge Gas: Argon
Pressure: 1 mTorr
Flow Rate: 27.8 sccm

Cavity Length (L_s): 8.45 cm
Loop Length (L_p): 3.45 cm

Discharge Height: 5.6 cm
Extension into Cavity (L_e): 1.4 cm
ECR Magnets: Present

Figure 5.8 - 360° Circumferential Electric Field Profile for TE_{111} Mode at 1 mTorr

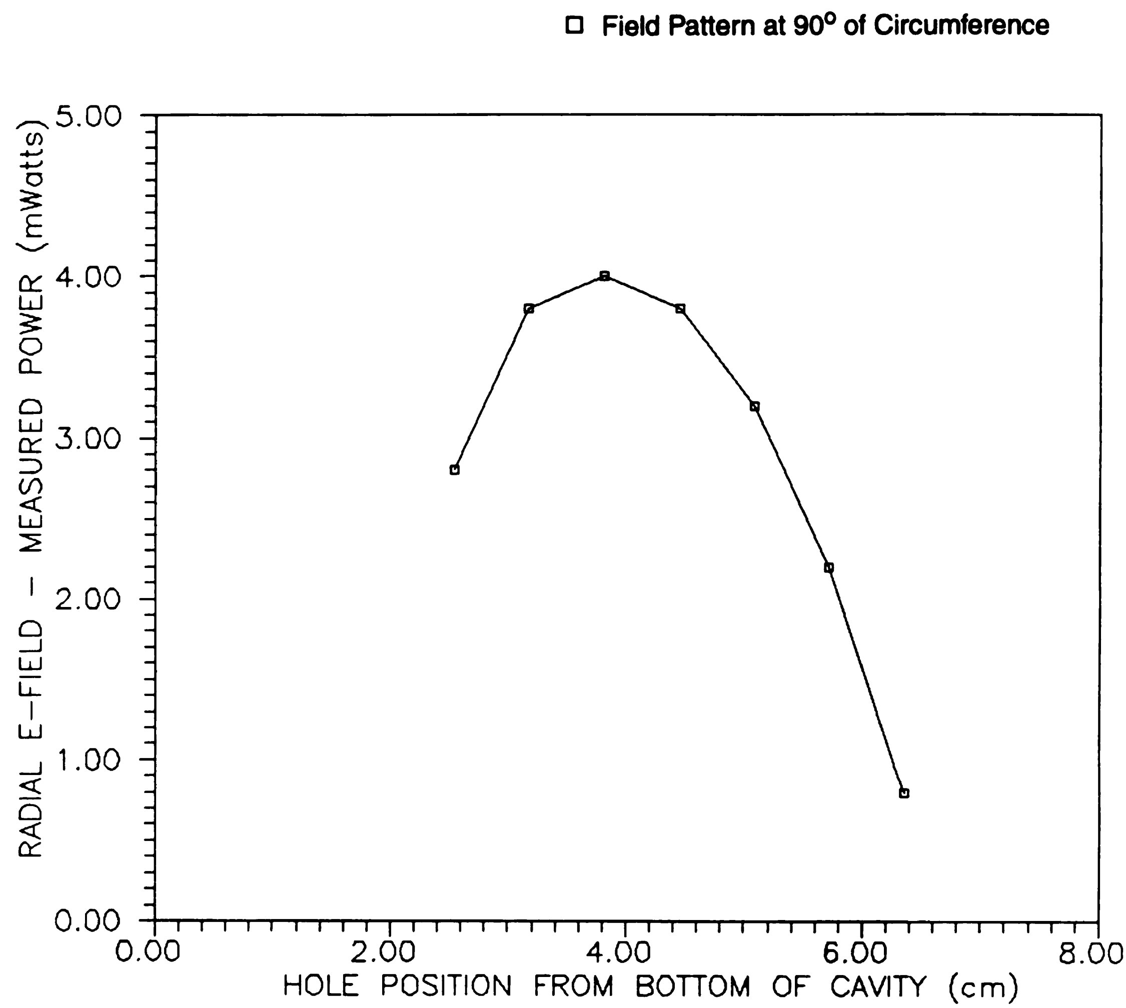

Input Power: 150 Watts
Reflected Power: 4.5 Watts

Discharge Gas: Argon
Pressure: 1 mTorr
Flow Rate: 27.8 sccm

Cavity Length (L_s): 8.45 cm
Loop Length (L_p): 3.45 cm

Discharge Height: 5.6 cm
Extension into Cavity (L_e): 1.4 cm
ECR Magnets: Present

Figure 5.9 - Longitudinal Electric Field Profile for TE_{111} Mode at 1 mTorr

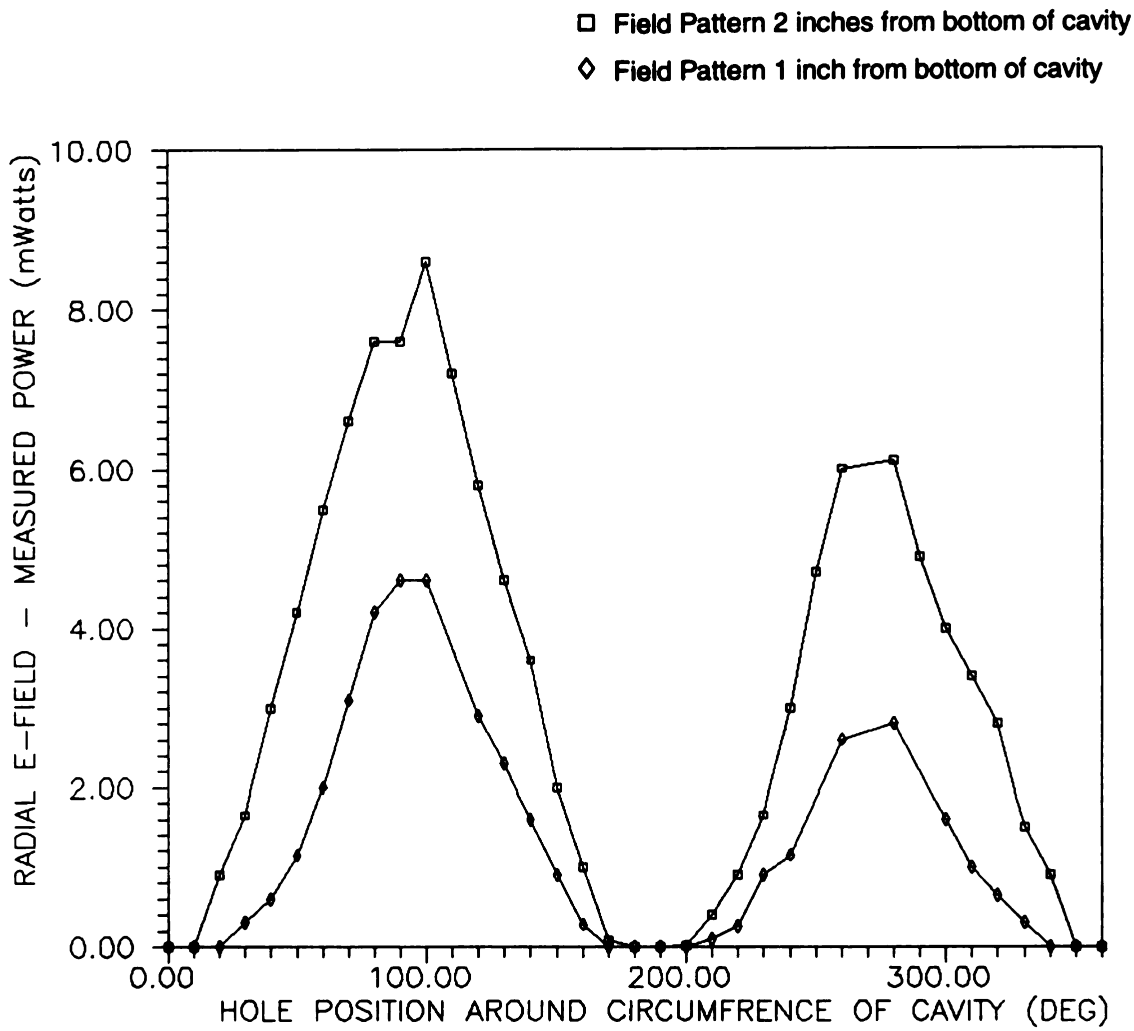

Input Power: 150 Watts
Reflected Power: 19.5 Watts

Discharge Gas: Argon
Pressure: 10 mTorr
Flow Rate: 45.2 sccm

Cavity Length (L_s): 9.05 cm
Loop Length (L_p): 3.45 cm

Discharge Height: 5.6 cm
Extension into Cavity (L_e): 1.4 cm
ECR Magnets: Present

Figure 5.10 - 360° Circumferential Electric Field Profile for TE_{111} Mode at 10 mTorr

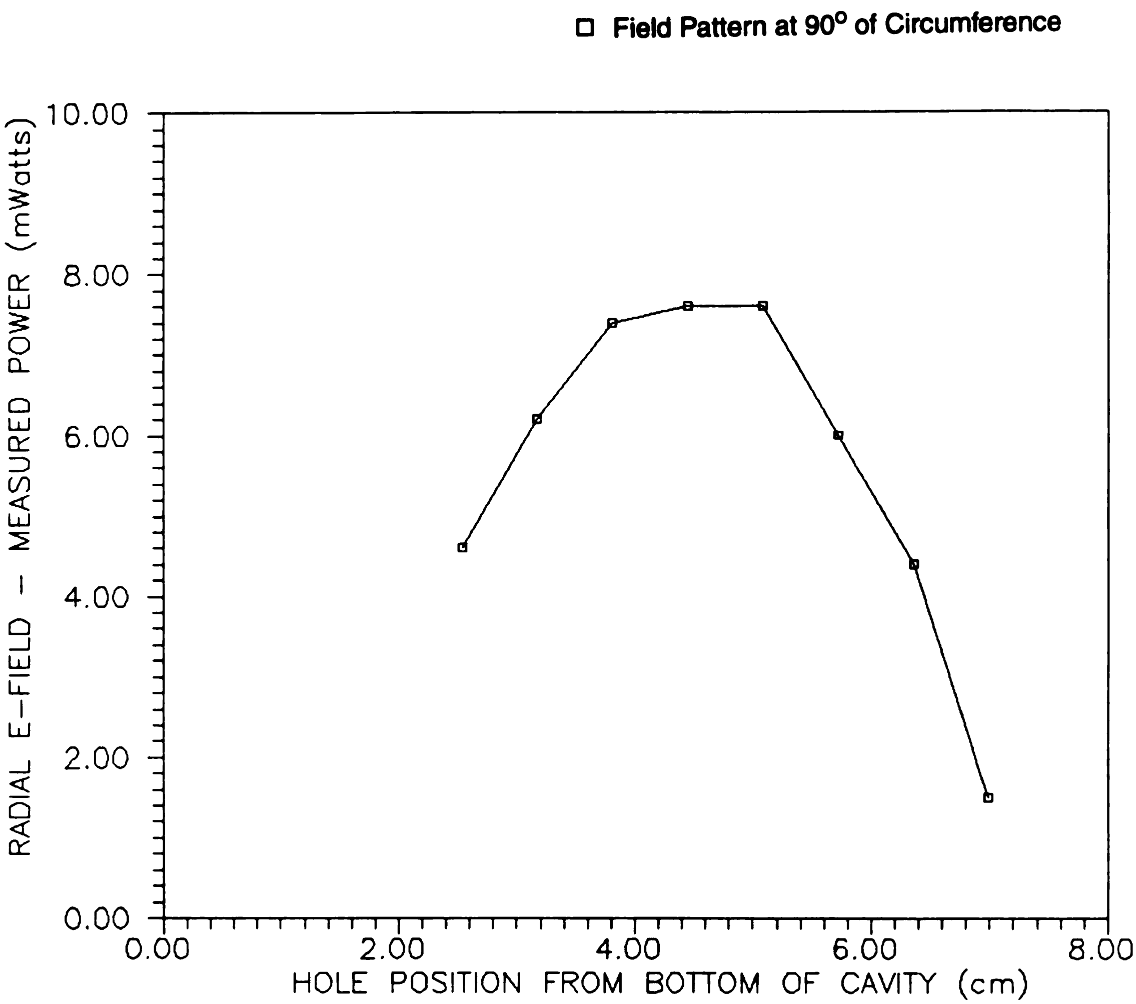

Input Power: 150 Watts
Reflected Power: 19.5 Watts

Discharge Gas: Argon
Pressure: 10 mTorr
Flow Rate: 45.2 sccm

Cavity Length (L_s): 9.05 cm
Loop Length (L_p): 3.45 cm

Discharge Height: 5.6 cm
Extension into Cavity (L_e): 1.4 cm
ECR Magnets: Present

Figure 5.11 - Longitudinal Electric Field Profile for TE_{111} Mode at 10 mTorr

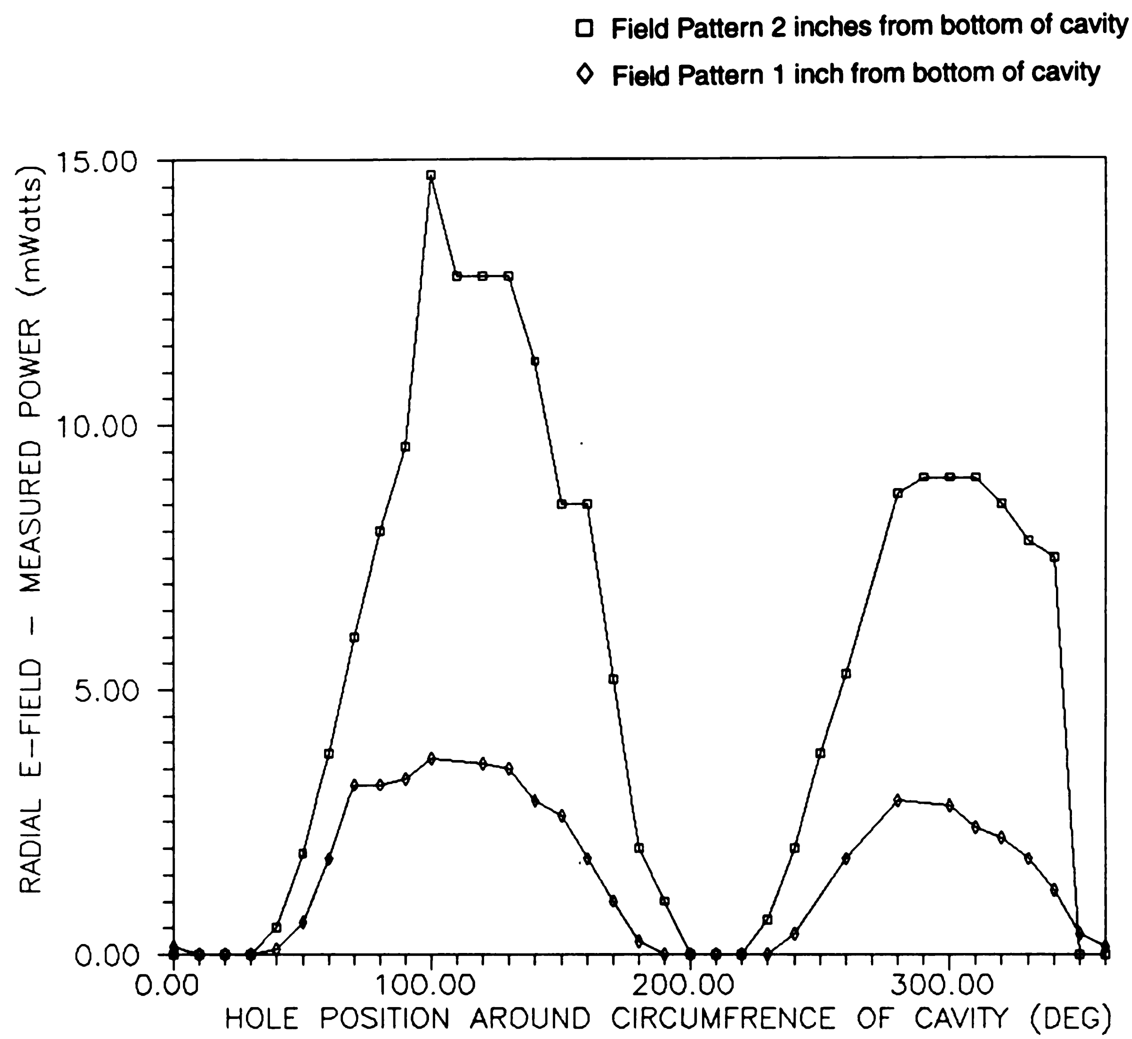

Input Power: 150 Watts
Reflected Power:

Discharge Gas: Argon
Pressure: 50 mTorr
Flow Rate: 95.1 sccm

Cavity Length (L_s): 9.35 cm
Loop Length (L_p): 3.45 cm

Discharge Height: 5.6 cm
Extension into Cavity (L_e): 1.4 cm
ECR Magnets: Present

Figure 5.12 - 360° Circumferential Electric Field Profile for TE_{111} Mode at 50 mTorr

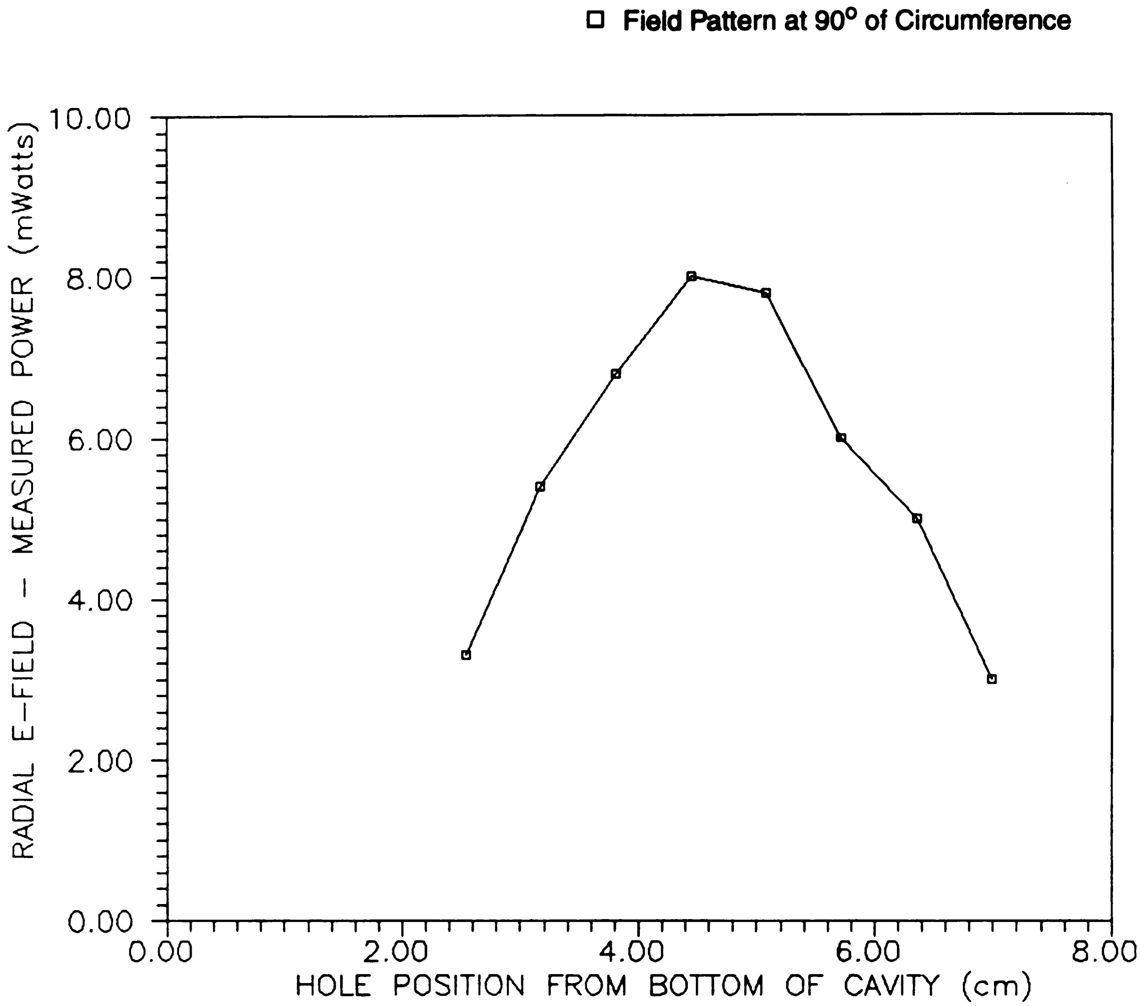

Input Power: 150 Watts
Reflected Power:

Discharge Gas: Argon
Pressure: 50 mTorr
Flow Rate: 95.1 sccm

Cavity Length (L_s): 9.35 cm
Loop Length (L_p): 3.45 cm

Discharge Height: 5.6 cm
Extension into Cavity (L_e): 1.4 cm
ECR Magnets: Present

Figure 5.13 - Longitudinal Electric Field Profile for TE_{111} Mode at 50 mTorr

5.6 cm discharge without ECR magnets at a discharge pressure of 50 mtorr. These plots also indicate a TE_{111} mode field pattern.

The field plots for the 6.9 cm discharge without ECR magnets at 50 mtorr are presented in Figures 5.22 and 5.23. The field plots taken at 5.08 cm and 7.62 cm from the bottom of the cavity show the two lobe pattern. However, the field plot taken at 2.54 cm from the bottom of the cavity, which is the closest to the discharge, shows a possible four lobe pattern. Note that this is a non-magnetic discharge so the impressed electric fields would not be influenced by any magnetically generated anisotropy of the discharge. No indication of this type of four lobe pattern was observed in any of the other field patterns recorded. This type of field pattern would normally be consistent with a TE_{211} type of cavity mode, however TE_{211} is in cutoff for this cavity diameter. It may be possible that an evanescent TE_{21} waveguide excitation exists in the region of the discharge. However, more investigation is necessary in order to determine the exact cause of this anomaly. The longitudinal plot, shown in Figure 5.23, demonstrates a half wave sinusoidal dependence observed in the other longitudinal plots presented for this mode.

It is observed that as pressure is increased from 1 mtorr to 50 mtorr for both 5.6 cm and 6.9 cm discharge that the relative strength of the electric field measured near the discharge (the longitudinal sampling hole at 2.5 cm) is decreased. For example in Figure 5.8 the power measured at the 2.5 cm sampling hole was 68% of the maximum measured along the cavity length. In Figure 5.10 the power measured at the 2.5 cm distance is 58% of maximum. In Figure 5.12 the power measured at this sampling hole is 40% of the maximum. The field plot in Figure 5.12 appears more symmetric on each side of its peak than do the longitudinal plots in Figures 5.8 and 5.10.

Plots taken for the 6.9 cm discharge with magnets display a similar phenomenon. In Figure 5.15 at 1 mtorr the power sampled closest to the discharge is 35% of the maximum power measured in this plot. In Figure 5.17 at 10 mtorr the power sampled at the 2.5 cm sampling hole is zero. In Figure 5.19 at 50 mtorr the power sampled at both 2.5 cm and 3.15 cm was zero.

From the data observed in this section we can conclude with a high degree of certainty that the high L_s mode observed in the data from Chapter 4 is in fact the TE_{111} mode.

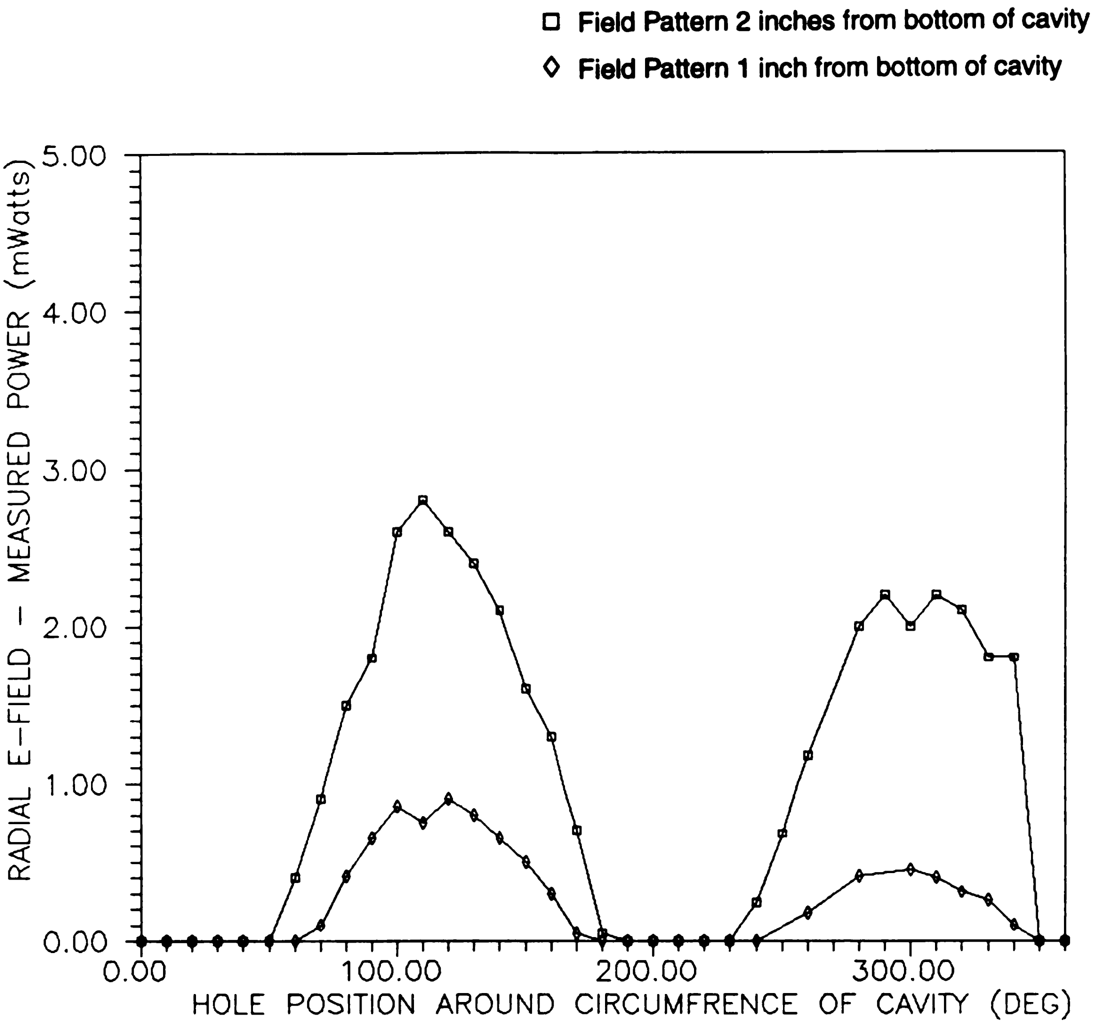

Input Power: 150 Watts
Reflected Power: 13 Watts

Discharge Gas: Argon
Pressure: 1 mTorr
Flow Rate: 23.9 sccm

Cavity Length (L_s): 9.15 cm
Loop Length (L_p): 3.45 cm

Discharge Height: 6.9 cm
Extension into Cavity (L_e): 2.7 cm
ECR Magnets: Present

Figure 5.14 - 360° Circumferentail Electric Field Profile for TE_{111} Mode at 1 mTorr

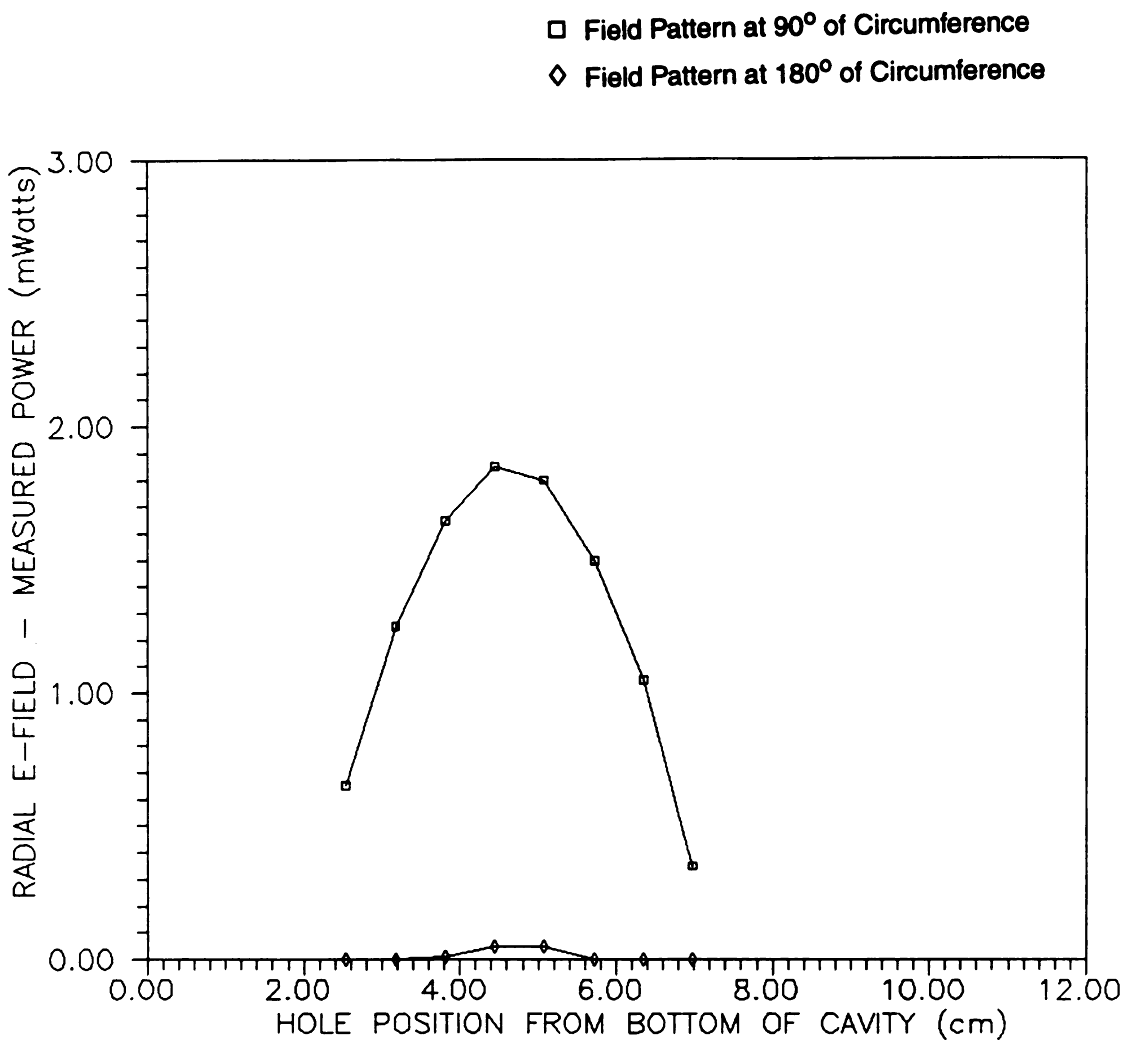

Input Power: 150 Watts
Reflected Power: 13 Watts

Discharge Gas: Argon
Pressure: 1 mTorr
Flow Rate: 23.9 sccm

Cavity Length (L_s): 9.15 cm
Loop Length (L_p): 3.45 cm

Discharge Height: 6.9 cm
Extension into Cavity (L_e): 2.7 cm
ECR Magnets: Present

Figure 5.15 - Longitudinal Electric Field Profile for TE_{111} Mode at 1 mTorr

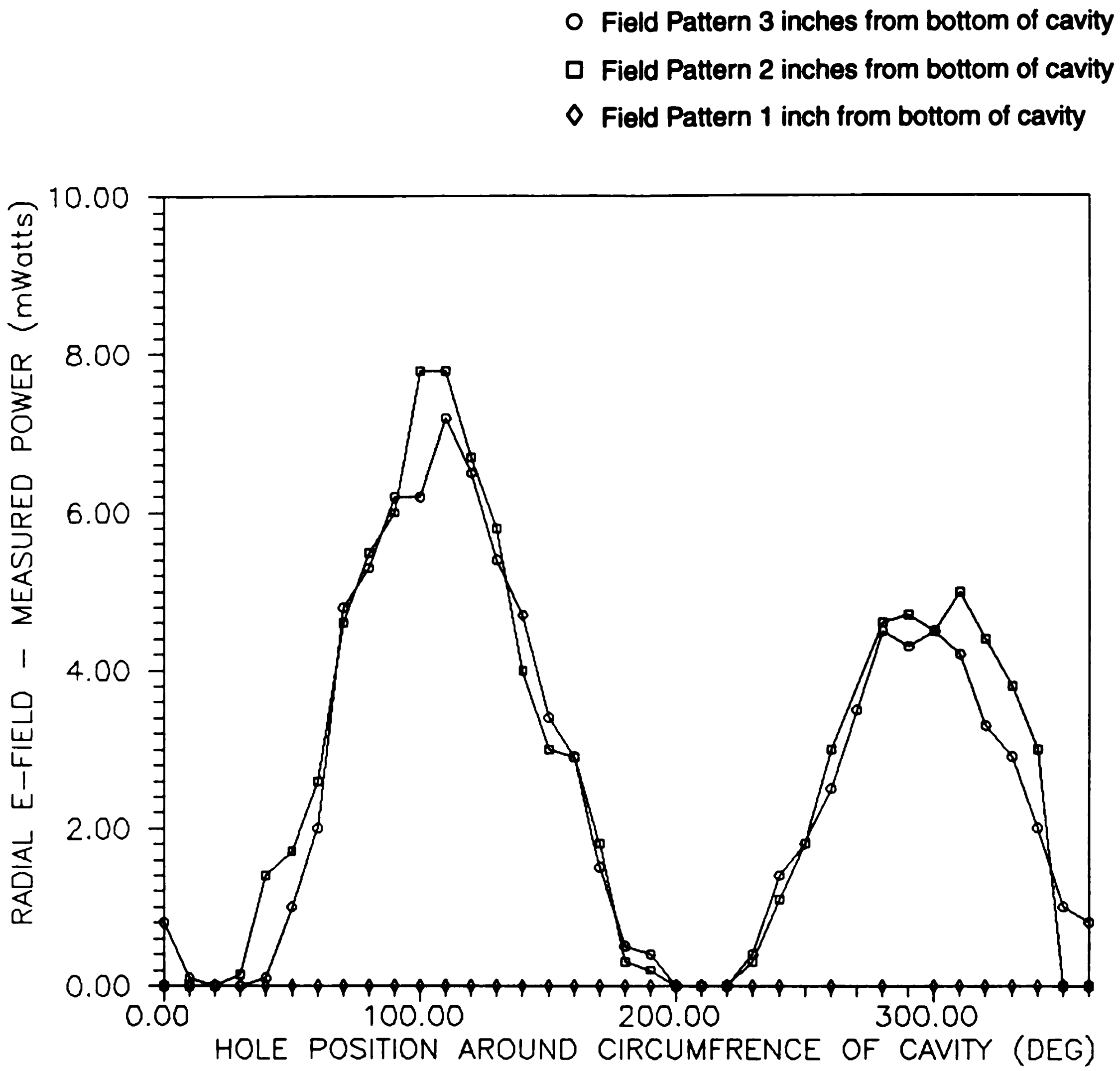

Input Power: 150 Watts
Reflected Power: 17 Watts

Discharge Gas: Argon
Pressure: 10 mTorr
Flow Rate: 45.4 sccm

Cavity Length (L_s): 10.75 cm
Loop Length (L_p): 3.45 cm

Discharge Height: 6.9 cm
Extension into Cavity (L_e): 2.7 cm
ECR Magnets: Present

Figure 5.16 - 360° Circumferential Electric Field Profile for TE_{111} Mode at 10 mTorr

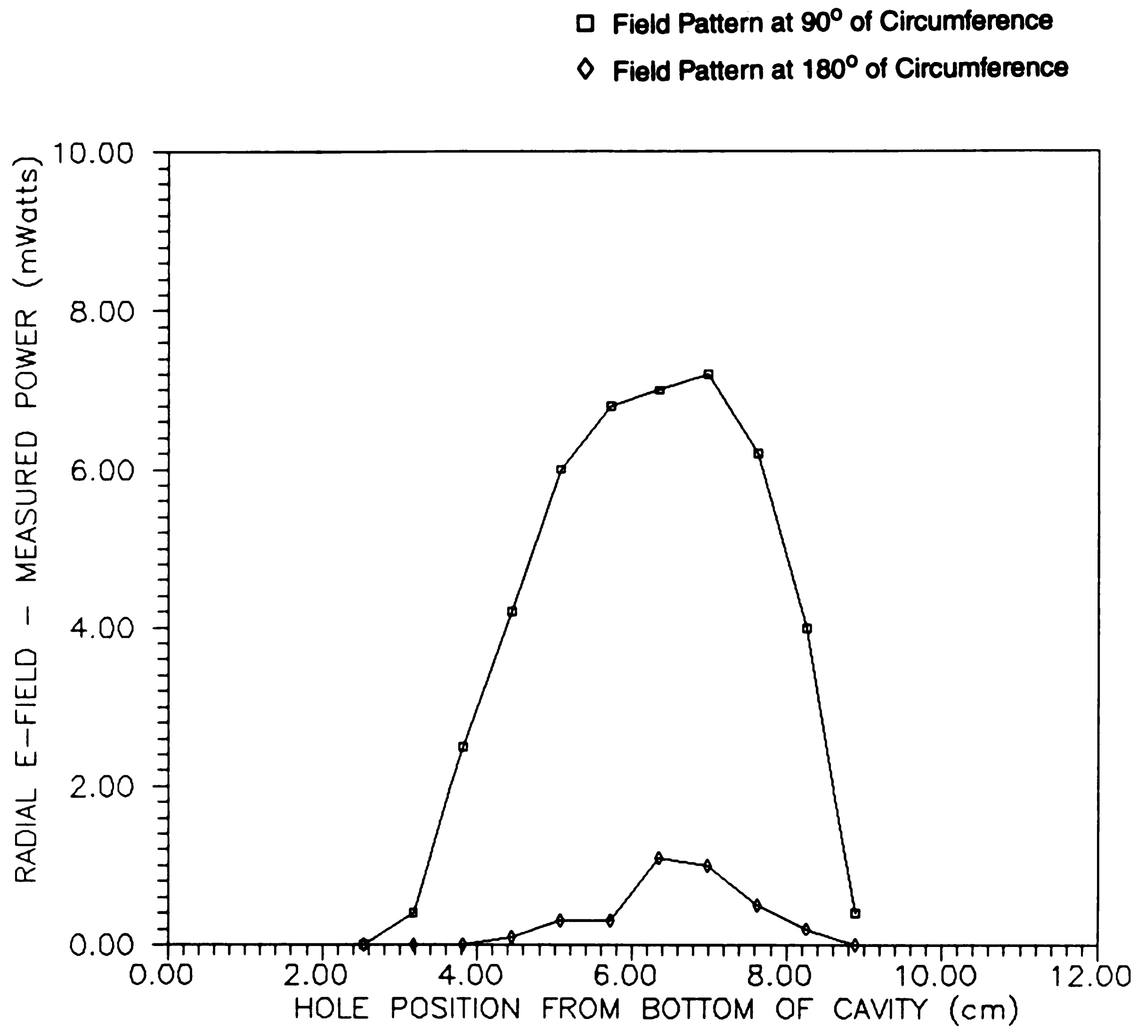

Input Power: 150 Watts
Reflected Power: 17 Watts

Discharge Gas: Argon
Pressure: 10 mTorr
Flow Rate: 45.4 sccm

Cavity Length (L_s): 10.75 cm
Loop Length (L_p): 3.45 cm

Discharge Height: 6.9 cm
Extension into Cavity (L_e): 2.7 cm
ECR Magnets: Present

Figure 5.17 - Longitudinal Electric Field Profile for TE_{111} Mode at 10 mTorr

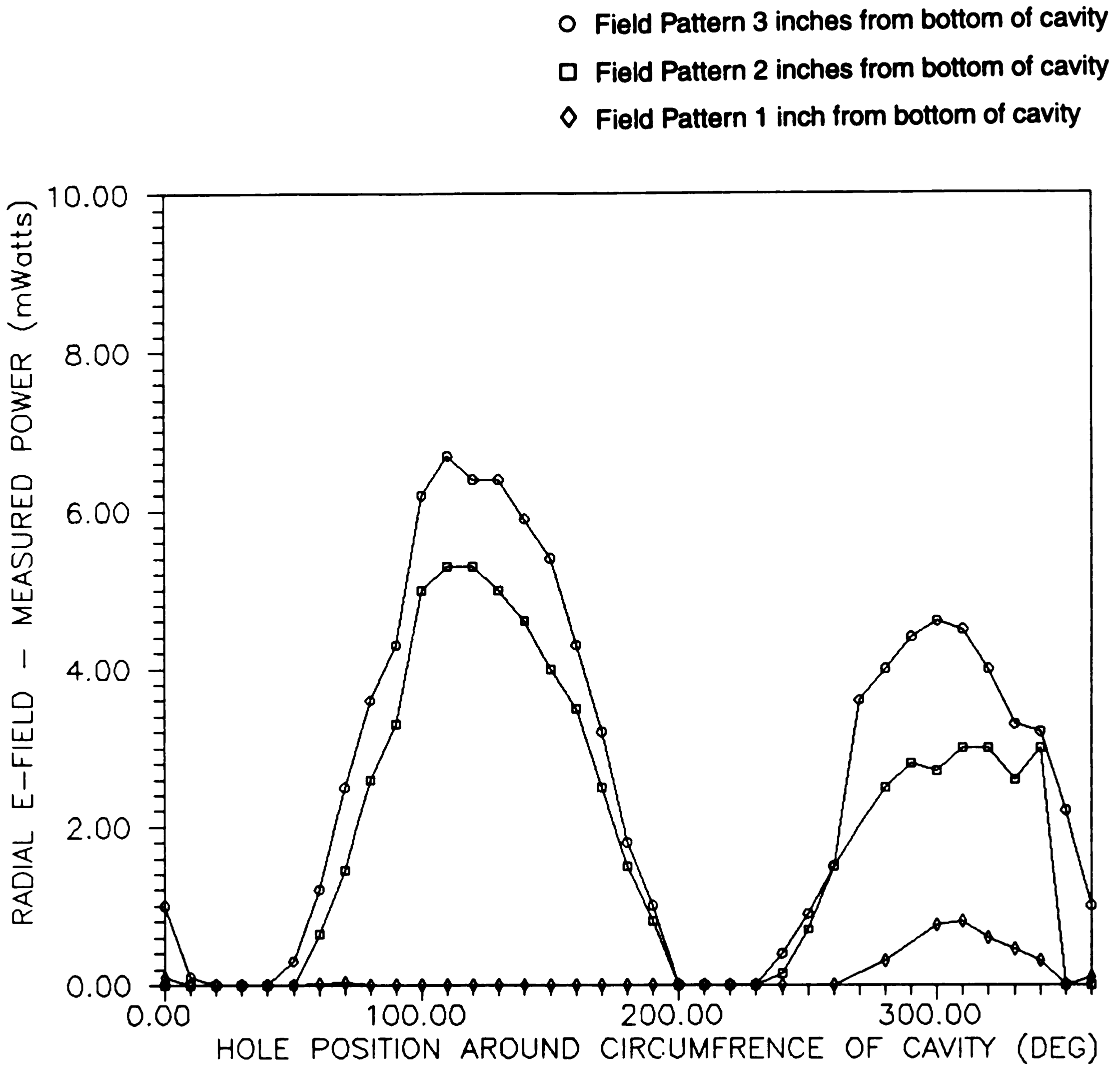

Input Power: 150 Watts
Reflected Power: 8 Watts

Discharge Gas: Argon
Pressure: 50 mTorr
Flow Rate: 87.5 sccm

Cavity Length (L_s): 11.1 cm
Loop Length (L_p): 3.45 cm

Discharge Height: 6.9 cm
Extension into Cavity (L_e): 2.7 cm
ECR Magnets: Present

Figure 5.18 - 360° Circumferential Electric Field Profile for TE_{111} Mode at 50 mTorr

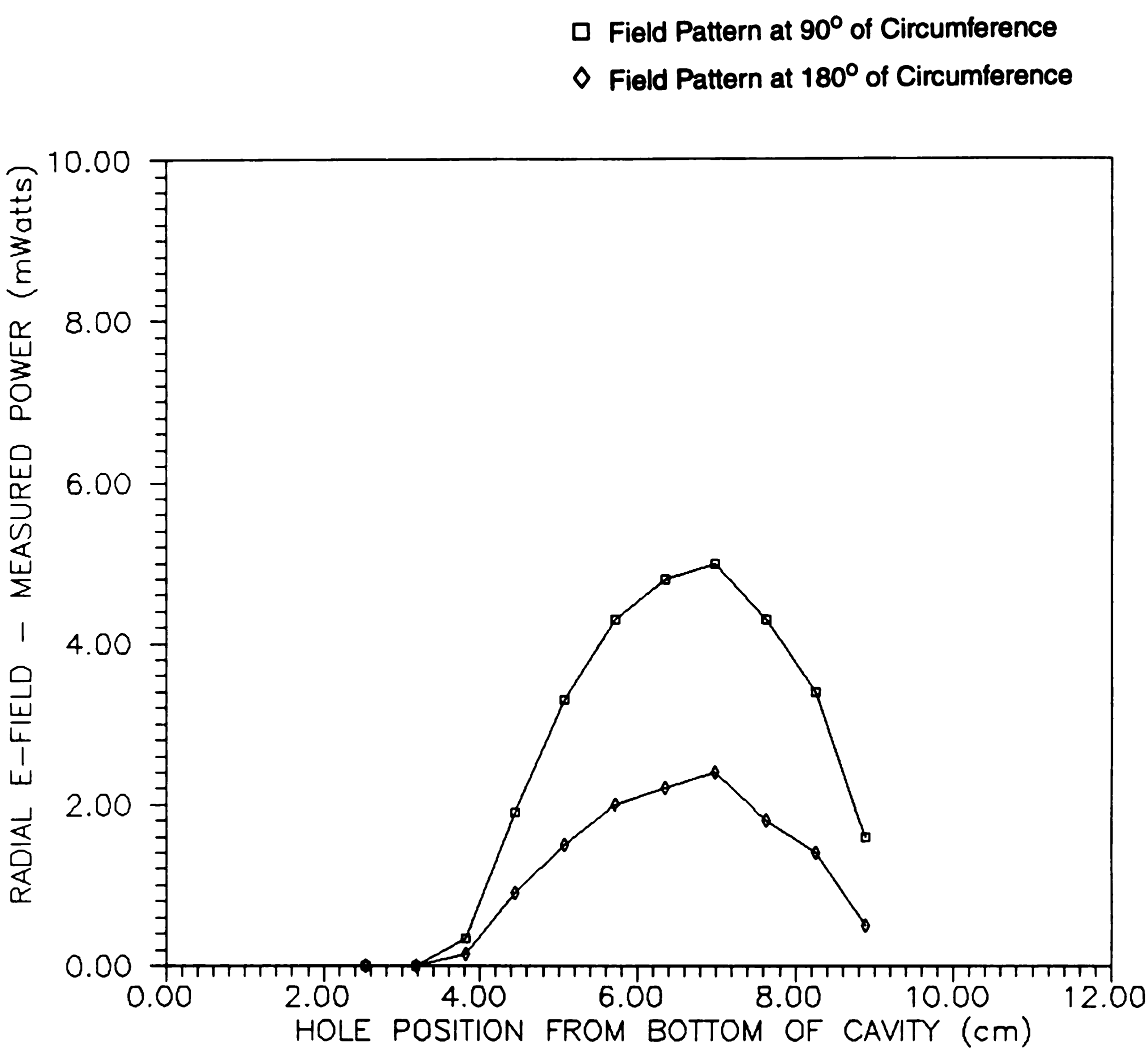

Input Power: 150 Watts
Reflected Power: 8 Watts

Discharge Gas: Argon
Pressure: 50 mTorr
Flow Rate: 87.5 sccm

Cavity Length (L_s): 11.1 cm
Loop Length (L_p): 3.45 cm

Discharge Height: 6.9 cm
Extension into Cavity (L_e): 2.7 cm
ECR Magnets: Present

Figure 5.19 - Longitudinal Electric Field Profile for TE_{111} Mode at 50 mTorr

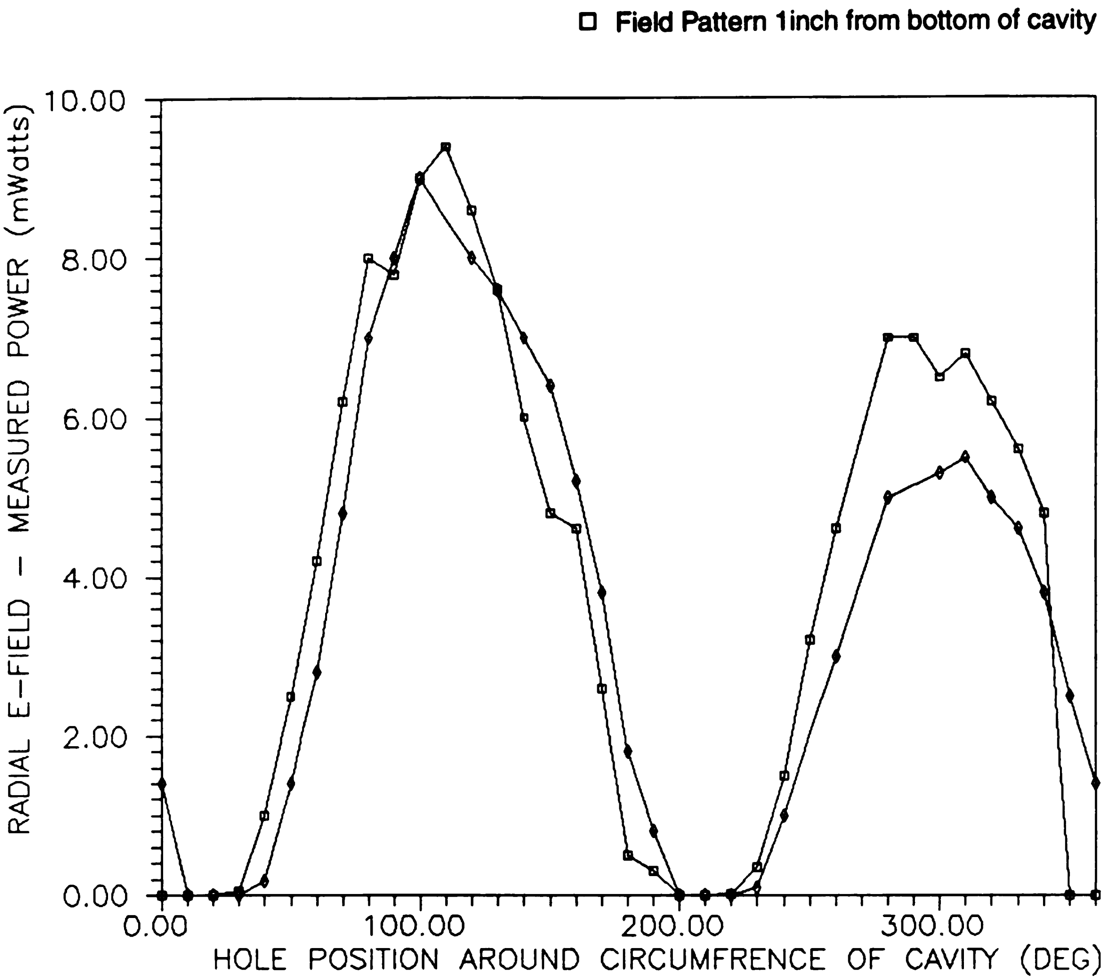

Input Power: 150 Watts
Reflected Power: 30 Watts

Discharge Gas: Argon
Pressure: 50 mTorr
Flow Rate: 96.6 sccm

Cavity Length (L_s): 6.33 cm
Loop Length (L_p): 3.45 cm

Discharge Height: 5.6 cm
Extension into Cavity (L_e): 1.4 cm
ECR Magnets: Not Present

Figure 5.20 - 360° Circumferential Electric Field Profile for TE_{111} Mode at 50 mTorr

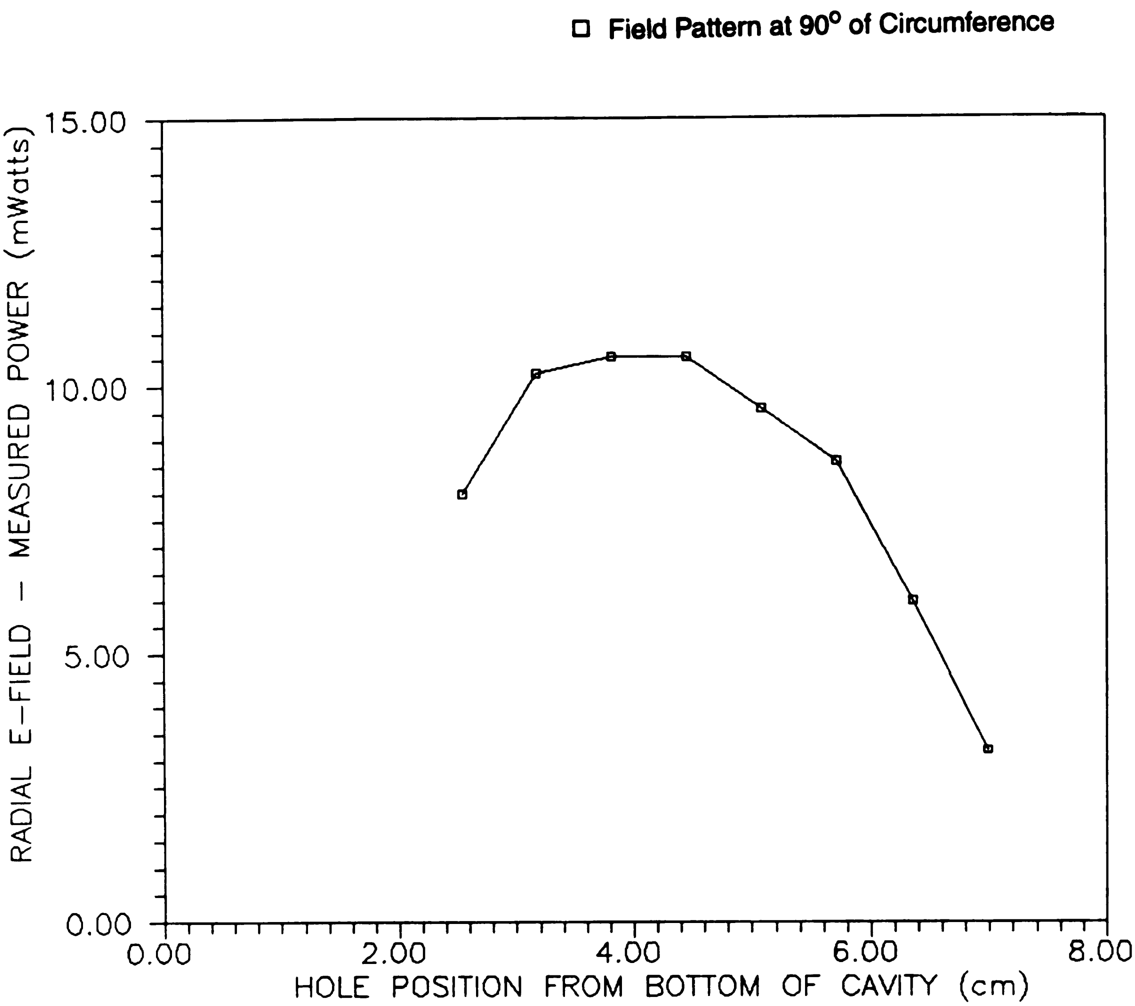

Input Power: 150 Watts	Cavity Length (L_s): 6.33 cm
Reflected Power: 30 Watts	Loop Length (L_p): 3.45 cm
Discharge Gas: Argon	Discharge Height: 5.6 cm
Pressure: 50 mTorr	Extension into Cavity (L_e): 1.4 cm
Flow Rate: 96.6 sccm	ECR Magnets: Not Present

Figure 5.21 - Longitudinal Electric Field Profile for TE_{111} Mode at 50 mTorr

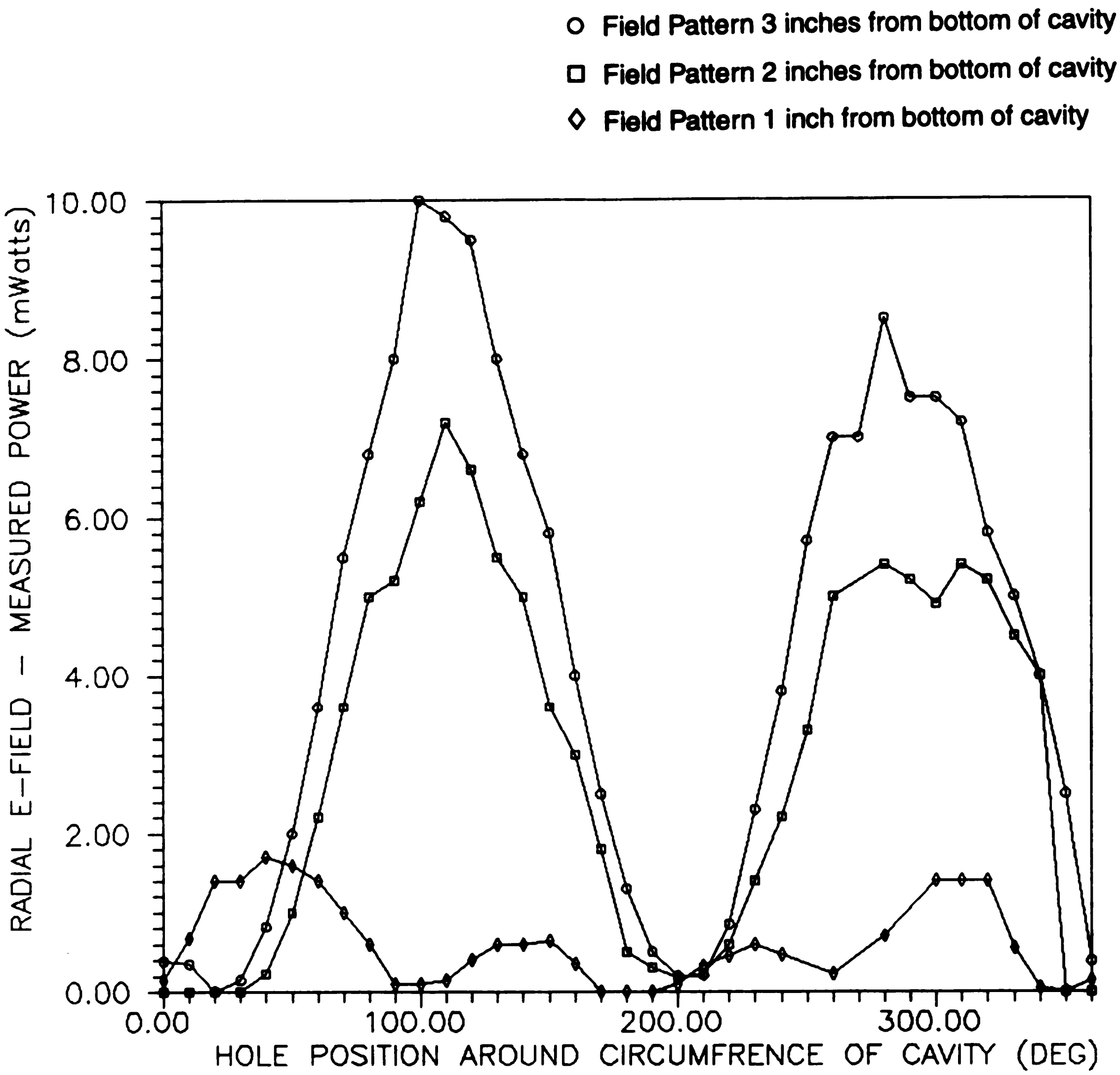

Input Power: 150 Watts
Reflected Power: 15 Watts

Discharge Gas: Argon
Pressure: 50 mTorr
Flow Rate: 91.0 sccm

Cavity Length (L_s): 11.23 cm
Loop Length (L_p): 2.85 cm

Discharge Height: 6.9 cm
Extension into Cavity (L_e): 2.7 cm
ECR Magnets: Not Present

Figure 5.22 - 360° Circumferential Electric Field Profile for TE_{111} Mode at 50 mTorr

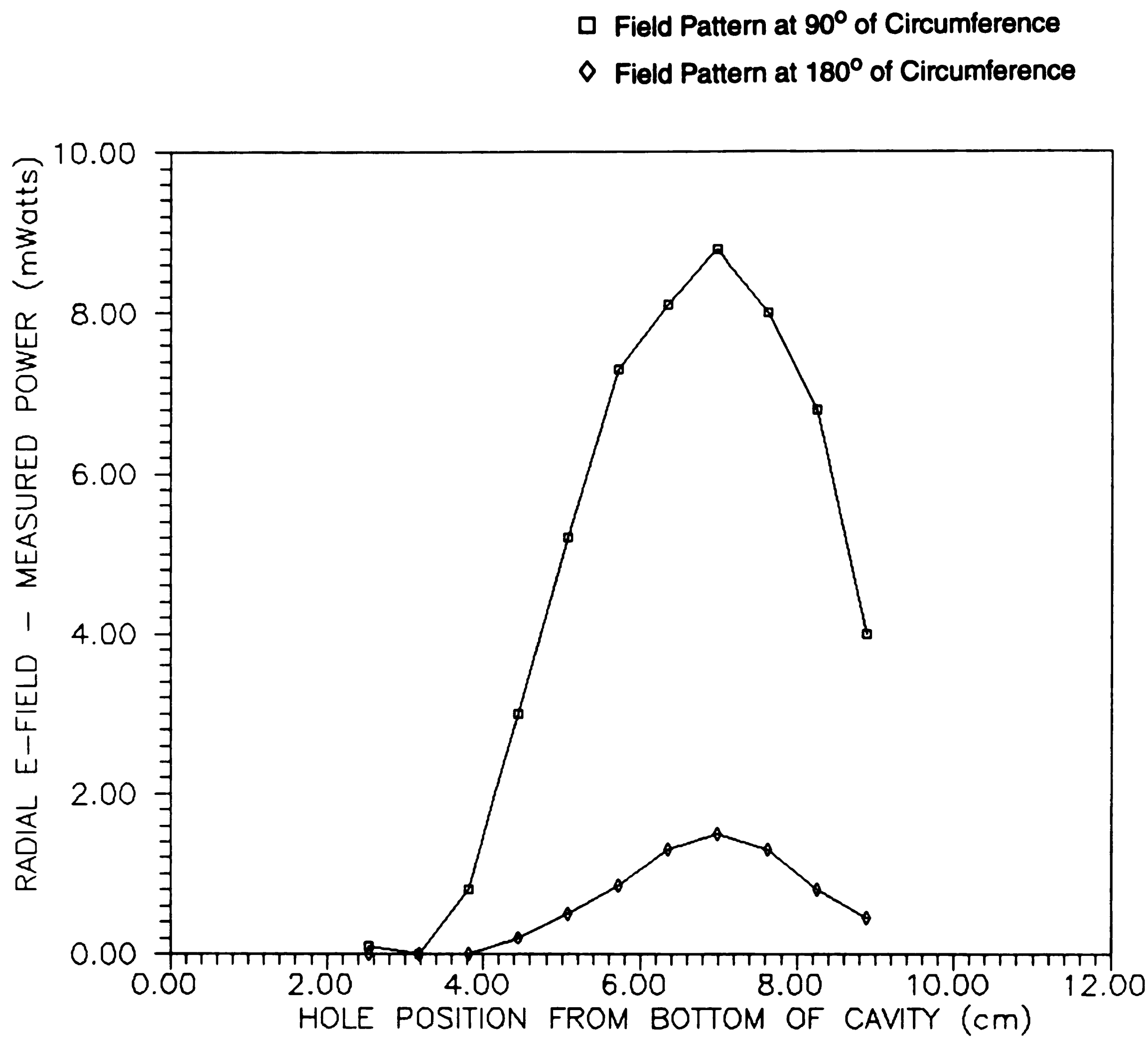

Input Power: 150 Watts
Reflected Power: 15 Watts

Discharge Gas: Argon
Pressure: 50 mTorr
Flow Rate: 91.0 sccm

Cavity Length (L_s): 11.23 cm
Loop Length (L_p): 2.85 cm

Discharge Height: 6.9 cm
Extension into Cavity (L_e): 2.7 cm
ECR Magnets: Not Present

Figure 5.23 - Longitudinal Electric Field Profile for TE_{111} Mode at 50 mTorr

5.5.3 Spatial Field Patterns for the Low L_s Mode:

Electric field pattern measurements for the Low L_s mode were performed for several pressures in the 5.6 cm discharge where the Low L_s mode was known to exist. The power measured by the microcoaxial probe was very low, in the range of 0 to 5 mWatts, compared to power measured for the TE_{111} mode, which was in the range of 0 to 25 mWatts. This reduced power combined with the uneven thickness of the cavity wall made electric field measurements for the Low L_s mode inconsistent and less conclusive. Nevertheless, these preliminary measurements seem to indicate that the Low L_s mode does not have a two lobe circumferential pattern indicative of the TE_{111} mode. Some field plots taken demonstrated a ϕ symmetric field pattern possibly indicative of a TM_{01} waveguide mode. Certainly, more accurate measurements must be performed to conclusively determine the electric field patterns for the Low L_s mode.

5.6 Correlation of Absorbed Power, Charge Density, and Internal E- Fields vs. L_s:

5.6.1 Description of the Experiment:

This was a preliminary experiment designed to investigate the influence of absorbed power on plasma charge density and internal electric field strength. The experimental setup was prepared in the same way as described in Section 4.3. In this experiment three parameters were investigated: 1) absorbed power, 2) ion saturation current, and 3) relative electric field strength. Absorbed power was determined from the reflected power measured with a Hewlet Packard analog power meter (item 10 in Figure 5.2). Ion saturation current was measured with a double Langmuir probe (item 4 in Figure 5.2) centered along the cavity axis 1 cm downstream from the ECR magnets. For all experiments listed in this section the Langmuir probe bias voltage was held constant at 40 Volts. Relative electric field strength was measured with a microcoaxial electric field probe (item 1 in Figure 5.2). Throughout this experiment the microcoaxial probe was kept at a fixed location 1.75" from the bottom of the cavity and 90^o from the center of the screened window.

After the discharge was struck and the correct pressure was selected the experimental measurements were taken. First the sliding short was set to its highest position at L_s = 13.35 cm. Then it was gradually lowered. Simultaneous measurements of reflected power, ion saturation current, and power sampled from the microcoaxial probe were taken at selected points as the short length was decreased. Another set of measurements were then recorded as the sliding short was raised from it's lowest position. These measurements were taken at 1 mtorr for both discharge chamber sizes with ECR magnets present.

5.6.1 Evaluation of a 5.6 cm Discharge with ECR Magnets at 1 mtorr:

Data from each of the three measurement variables taken at a discharge pressure of 1 mtorr are plotted in Figure 5.24. The absorbed power curve is observed to have two maxima. The maxima near L_s = 5.6 cm was shown with field pattern measurements to be the Low L_s mode. The maxima near L_s = 8.5 cm is similarly found to be the TE_{11} mode. The two maxima on the absorbed power curve correlate well with the location of two maxima also found on the ion saturation current curve. Note that the I_{sat} maxima generated by the Low L_s mode at $L_s = 5.6$ cm is approximately twice the value of the maxima generated by the TE_{11} mode. Recall that the microcoaxial probe measures microwave power, thus data plotted from the probe readings is proportional to the square of the impressed electric field. The relative electric field measurements show that there are two electric field maxima present. The E-field maxima measured for the Low L_s mode is very small compared to the E-field maxima found at the TE_{11} mode. Note that there is very little hysteresis observed in any of the curves shown.

5.6.2 Evaluation of a 6.9 cm Discharge with ECR Magnets at 1 mtorr:

In Figure 5.25 each of the measurement parameters are plotted vs. L_s for a discharge pressure of 1 mtorr. Individual plots of P_{abs}, I_{sat}, E_{rel} are shown in Figures 5.26, 5.27, and 5.28, respectively. From Figure 5.25 we see that there is one major maxima for all parameters at approximately $L_s = 9.2$ cm. Using E-field pattern measurements this was found to be the TE_{11} mode. Note that the absorbed power curve shows some indication of another maxima in the region of $L_s = 6$ cm that could possibly be due to the Low L_s mode. However, field pattern measurements need to be made to confirm this.

As seen in Figure 5.26 hysteresis is very pronounced for absorbed power in the range of $L_s = 8$ cm to 10 cm. Notice that the highest maxima was reached while L_s was increased. There is also hysteresis in absorbed power, shown in Figure 5.27, where the highest maxima is also reached while increasing L_s. Finally, hysteresis is shown in relative electric field measurements as well, shown in Figure 5.28.

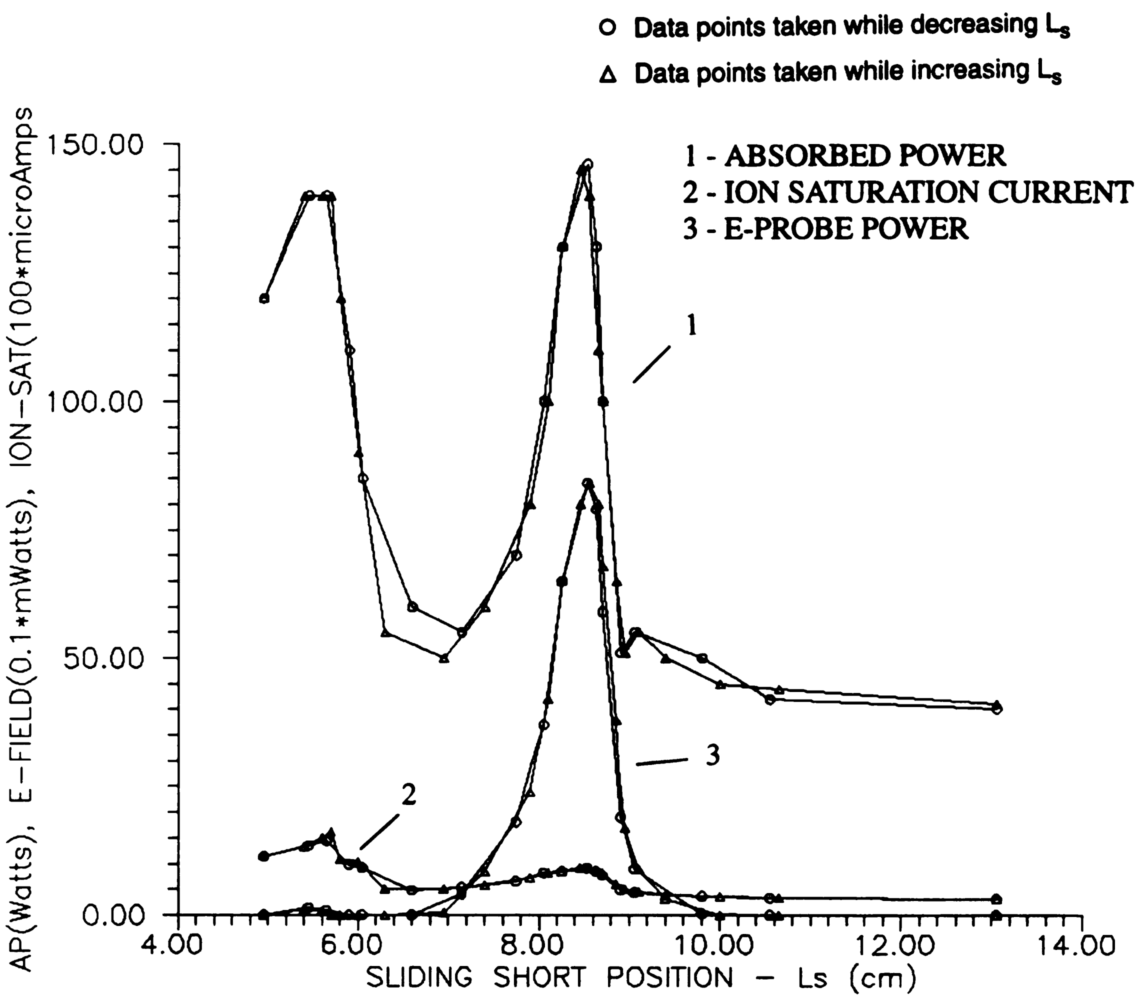

Input Power: 150 Watts
Discharge Gas: Argon
Pressure: 1 mTorr
Flow Rate: 27.8 sccm

Loop Length (L_p): 3.45 cm
Discharge Height: 5.6 cm
Extension into Cavity (L_e): 1.4 cm
ECR Magnets: Present

Figure 5.24 - Absorbed Power, Ion Saturation Current, and Probe Power vs. L_s

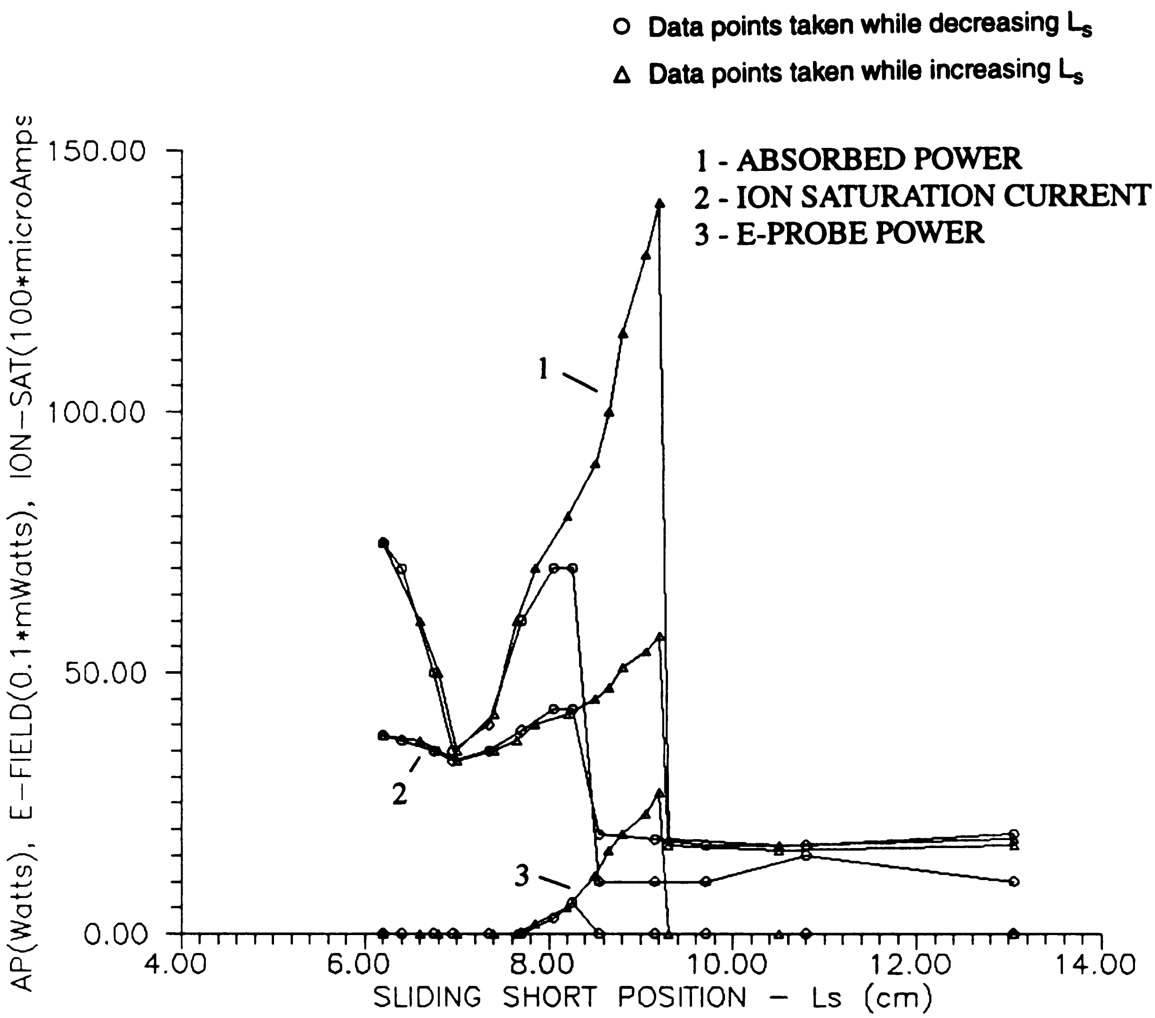

Input Power: 150 Watts
Discharge Gas: Argon
Pressure: 1 mTorr
Flow Rate: 23.9 sccm

Loop Length (L_p): 3.45 cm
Discharge Height: 6.9 cm
Extension into Cavity (L_e): 2.7 cm
ECR Magnets: Present

Figure 5.25 - Absorbed Power, Ion Saturation Current, and Probe Power vs. L_s

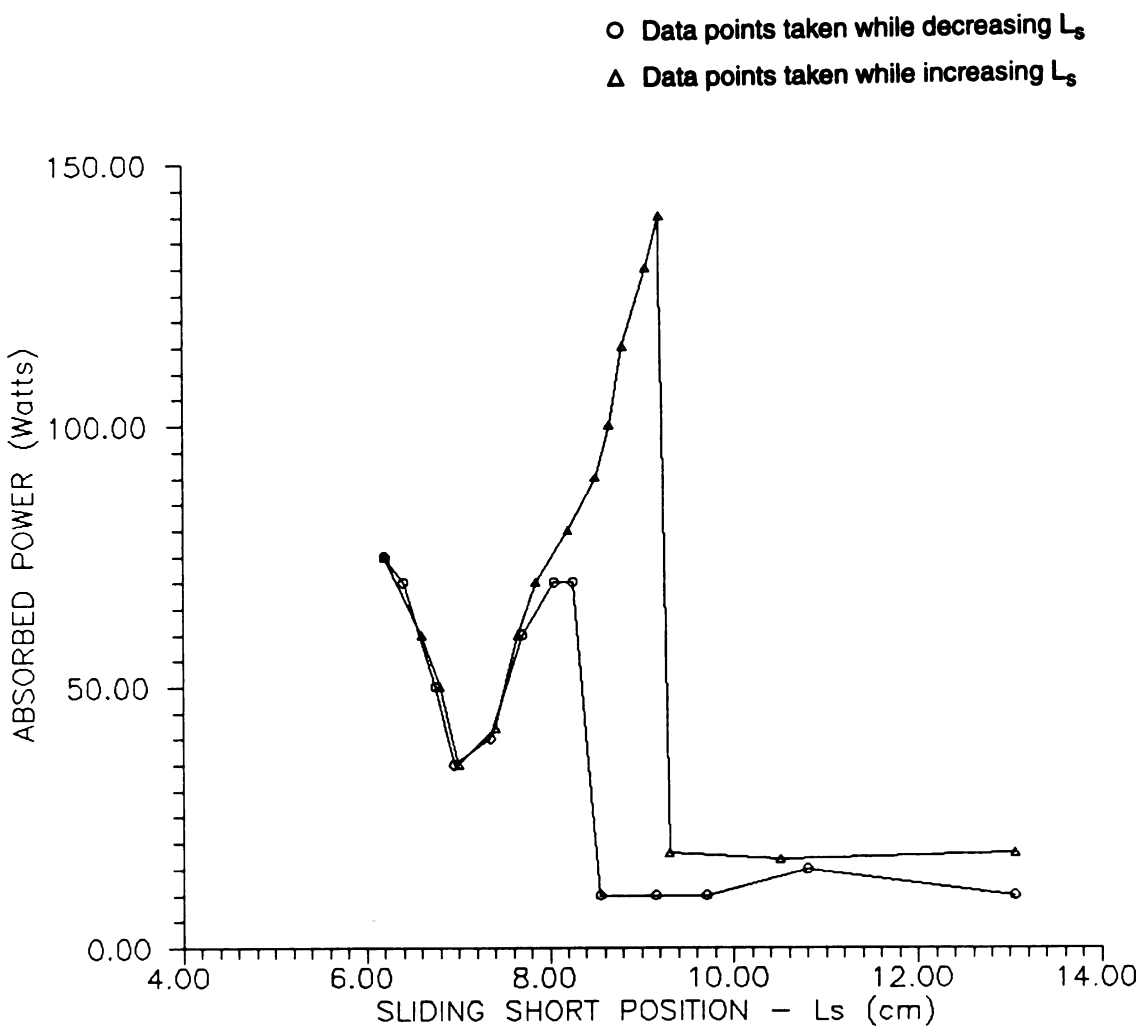

Input Power: 150 Watts
Discharge Gas: Argon
Pressure: 1 mTorr
Flow Rate: 23.9 sccm

Loop Length (L_p): 3.45 cm
Discharge Height: 6.9 cm
Extension into Cavity (L_e): 2.7 cm
ECR Magnets: Present

Figure 5.26 - Absorbed Power vs. L_S for a 6.9 cm Discharge at 1 mTorr

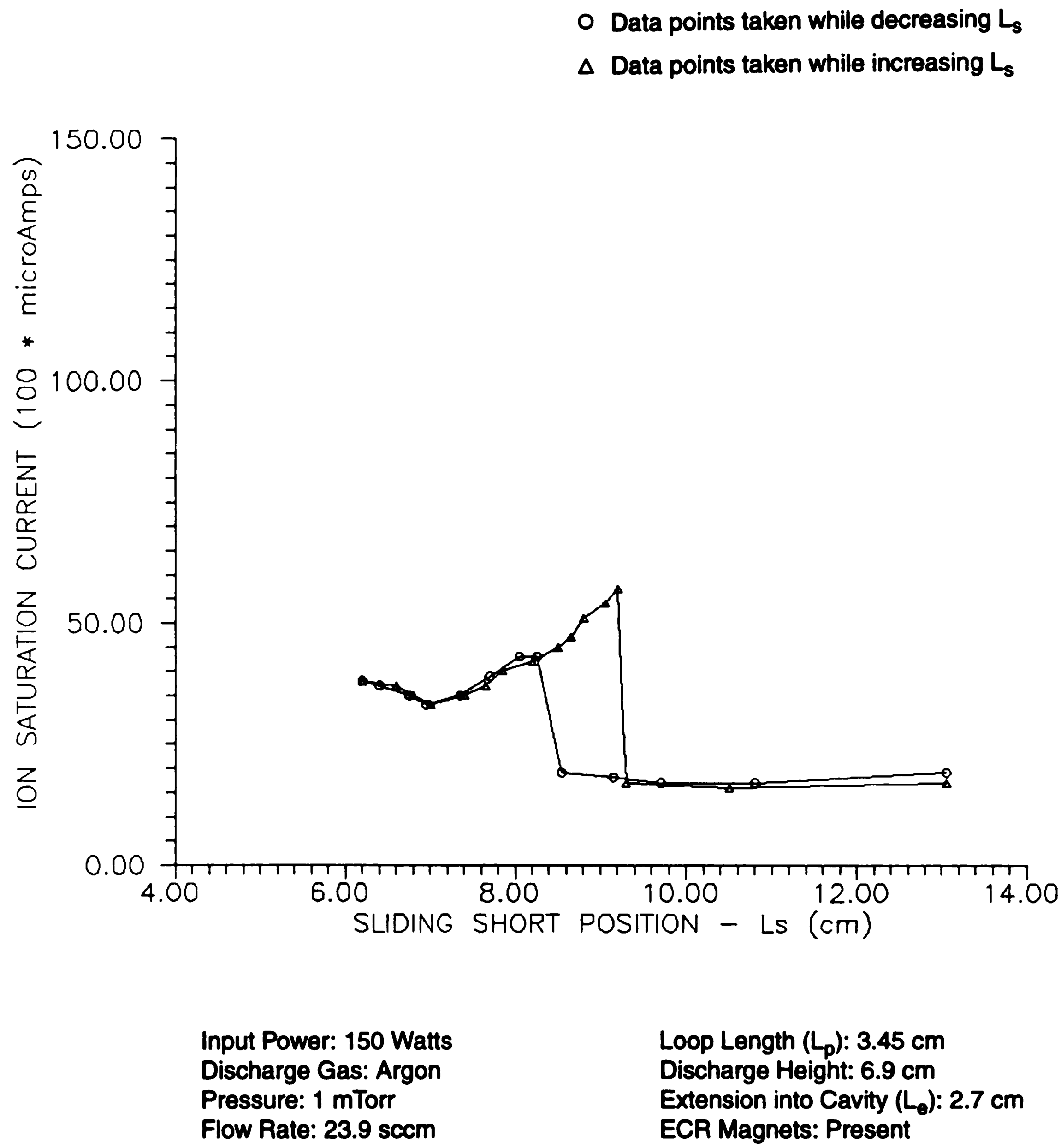

Figure 5.27 - Ion Saturation Current vs. L_s for a 6.9 cm Discharge at 1 mTorr

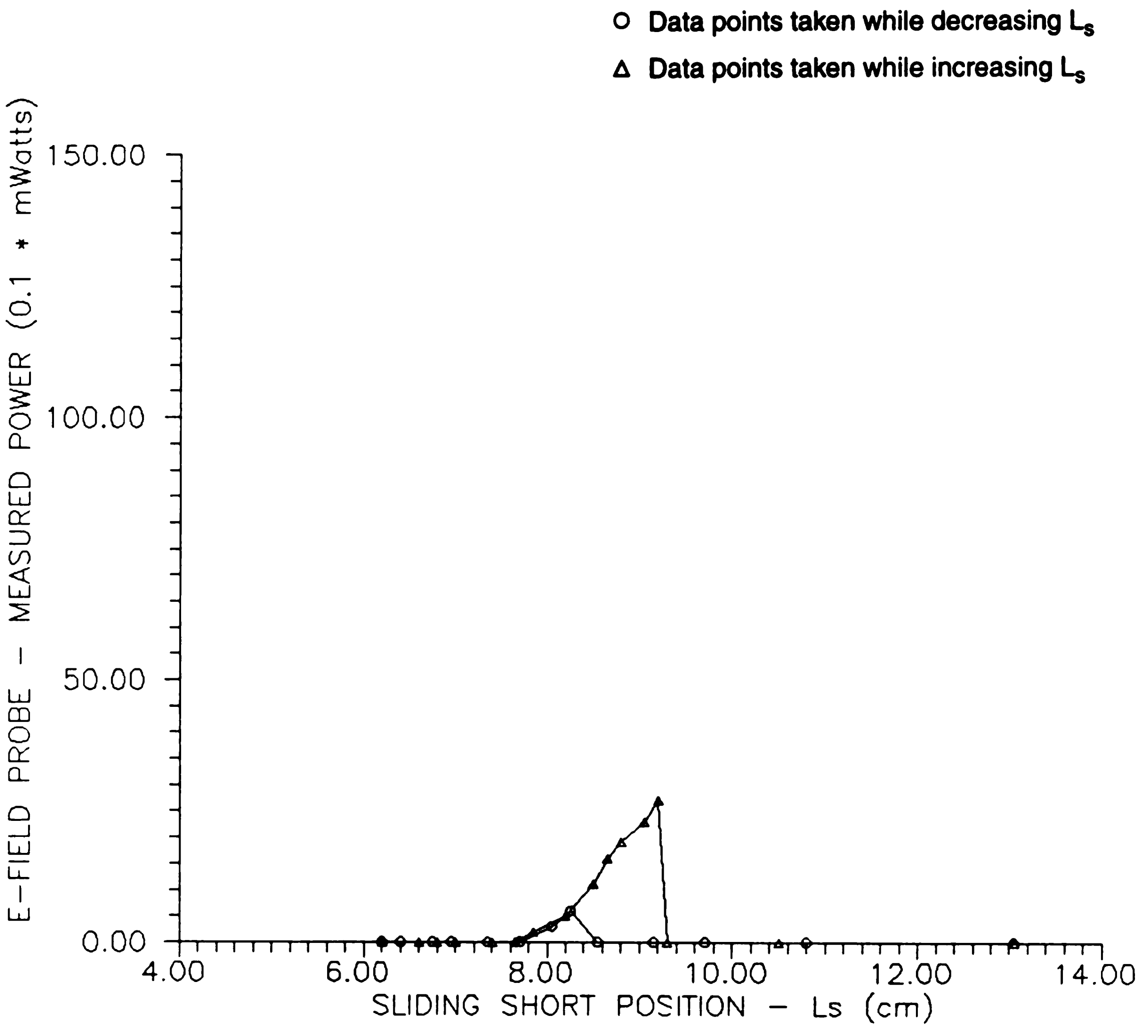

Input Power: 150 Watts
Discharge Gas: Argon
Pressure: 1 mTorr
Flow Rate: 23.9 sccm

Loop Length (L_p): 3.45 cm
Discharge Height: 6.9 cm
Extension into Cavity (L_e): 2.7 cm
ECR Magnets: Present

Figure 5.28 - Electric Field Probe Power vs. L_S for a 6.9 cm Discharge at 1 mTorr

5.7 Conclusions:

In this chapter two sets of experiments were performed: 1) to determine the electric field patterns present for all resonances found in plasma cavity, and 2) to correlate the behavior of absorbed power with that of plasma charge density and internal electric field strength. Conclusions made from these experiments are as follows:

Field Pattern Experiments:

- The higher L_s of the two modes found in the cavity is confirmed to be the TE_{111} cavity mode. The TE_{111} mode was observed to produce similar circumferential field patterns for several configurations and pressures.

- As pressure is increased the ratio of: electric field strength near the discharge to maximum electric field strength along the axis of the cavity, decreases.

- The internal electric fields produced in the Low L_s mode are very low compared to the TE_{111} mode. Preliminary field pattern measurements indicate a ϕ symmetric field pattern for the Low L_s mode possibly indicative of a TM_{01} waveguide mode.

Correlation of Absorbed Power with Charge Density and Electric Field Strength:

- For all conditions investigated the maxima of relative charge density vs. L_s curves are found to correlate with the maxima of the absorbed power vs. L_s curves.

- The maxima in relative charge density vs. L_s is twice the value for the maxima in relative charge density for the TE_{111} mode.

- Maxima in relative electric field strength vs. L_s also correlates with absorbed power curves, however electric field strength for the Low L_s mode appears much less than for the TE_{111} mode.

- Hysteresis is not observed for the 5.6 cm discharge chamber, but is observed for the 6.9 cm chamber. Hysteresis is strongly correlated between absorbed power, relative charge density, and internal electric field strength.

Chapter 6

Conclusions and Recommendations

6.1 Summary and Conclusions for this Investigation:

In this thesis the electromagnetic behavior of a compact ECR microwave plasma source has been investigated over several input parameters. First the electromagnetic mode behavior was mapped by recording reflected power curves vs. L_s for a range of pressures and four different source geometries. From this mapping the existence and location of all resonant modes was determined. Electric field pattern measurements were taken in oder to electromagnetically identify these modes. Relative charge density and internal electric field strength measurements were also taken to provide further information about the modes observed and to better understand the correlation between absorbed power and plasma charge density.

All experiments in this thesis were conducted with the plasma source described in Chapter 2 using argon as the discharge gas. The 2.45 GHz incident microwave power was held constant at 150 Watt for all experiments. The experimental input variables were: cavity length L_s, loop length L_p, discharge pressure p, discharge chamber height h, and presence or absence of the multipole magnet ring. Flow rate was coupled to discharge pressure in the system used. Output variables measured were: reflected power P_{ref}, spatial electric field variation, internal electric field strength, and relative plasma charge density.

The general conclusions for this investigation are as follows:

- The plasma source could be tuned to two distinct resonant modes.

- The first mode was investigated with electric field pattern measurements and was determined to be the TE_{11} mode. This mode was found to exist at all discharge pressures and geometry configurations.

- The second mode (called the Low L_s mode) was more difficult to conclusively identify. Preliminary results suggest a ϕ symmetric field pattern indicative of a TM_{01} mode. This mode had two significant features: 1) it appears to produce twice the charge density of the TE_{11} mode at the discharge pressure of 1 mtorr, and 2) it has a broad L_s profile making it less sensitive to tuning variations than the TE_{11} mode.

- The presence of the multipole magnet ring was shown to have two advantageous effects: 1) it allowed a discharge to be sustained at pressures near 1 mtorr (most likely due to ECR coupling) where the lowest pressure achievable without magnets is 40 mtorr, 2) it improved the ability to sustain and match the discharge at pressures of 40 and 100 mtorr.

- Three important observations were made in the comparison of two different height discharge chambers: 1) The Low L_s mode could always be observed with the 5.6 cm discharge chamber and was not observed for most conditions with the 6.9 cm discharge chamber, 2) significant hysteresis was observed with the 6.9 cm discharge for pressures of 0.75 to 40 mtorr (with magnets) and very little hysteresis was observed for the 5.6 cm discharge in the same range, and 3) at pressures over 40 mtorr without magnets the 6.9 cm discharge was shown to sustain a discharge much better than the 5.6 cm discharge.

- Relative charge density of the discharge is strongly correlated with measured absorbed power. Hysteresis of absorbed power is accompanied by a similar hysteresis in relative charge density and relative electric field strength.

6.2 Transmission Line Model of the Plasma Loaded Cavity:

The microwave plasma source described in Chapter 2 can be divided into four different sections based on the modes of electromagnetic propagation in each section. See Figure 3.11. Section I begins at the z = 0 input plane and consists of a small diameter coaxial feed line ending at the $z = z_1$ plane (the plane of the sliding short). Section II consists of the dual co-axial region formed by the loop antenna from the $z = z_1$ plane to the $z = z_2$ plane. Note that the dual coax is shorted at $z = z_2$. Section III is the section of empty cylindrical waveguide from the $z = z_2$ plane to the beginning of the plasma load at $z = z_3$. Finally, section IV begins at $z = z_3$ and consists of a series of several short waveguide sections of different diameter surrounding the quartz discharge chamber that contains the plasma load.

Section I can be modeled as a transmission line section, shown at the bottom of Figure 6.1, with characteristic impedance $Z_0 = 50\ \Omega$. Section II can be modeled as a transmission line section with $Z_0 = 266\Omega$. The characteristic impedance for section II was calculated [27] assuming a dual coaxial line with outer conductor diameter of 9.8 cm and inner conductor radius of 0.476 cm and inner conductor separation of 2.5 cm using the equation:

$$Z_0 = 120\left\{\ln\left[2p\frac{(1-q^2)}{(1+q^2)}\right] + \frac{-1+4p^2}{16p^4}(1-4q^2)\right\} \qquad \text{Eq. 3.22}$$

where $p = s/d$, $q = s/D$, s is the separation between dual center conductors, d is the diameter of each center conductor, and D is the diameter of the outer conductor.

Section III can be modeled as one individual or two parallel transmission line sections depending on the mode or modes excited in the cavity. This 9.8 cm diameter waveguide is capable of propagating the TE_{11} mode and the TM_{01} mode. Thus, either or both modes of propagation can be represented as transmission lines. The transmission line representing the TE_{11} mode has $Z_0 = 544.44\ \Omega$ calculated with the relation:

$$Z_{TE} = \frac{\eta_0}{\sqrt{1-\left(\frac{\omega_c}{\omega}\right)^2}} \qquad \text{Eq. 3.23}$$

where η_0 is the characteristic impedance of free space, ω is the radian frequency of microwave radiation, and ω_c is the cutoff frequency of the TE mode. Similarly, the transmission line representing TM_{01} has $Z_0 = 109.96\ \Omega$ calculated with the relation:

$$Z_{TM} = \eta_0\sqrt{1-\left(\frac{\omega_c}{\omega}\right)^2} \qquad \text{Eq. 3.24}$$

Section IV, shown in Figure 3.11, the region of the plasma discharge can be modeled as a lumped complex load impedance, Z_{plasma}. The complex impedance of this load is dependent on the properties of the discharge.

Note that this model does not include the effects of the abrupt discontinuities in the propagation of electromagnetic waves from one section to the next. These discontinuities give rise to evanescent modes that store energy in the vicinity of the discontinuity and may in future models be represented by lumped parameter capacitors. However, more analysis is required in order to add such elements to this model.

A few important dimensional variables of the plasma source must be identified. These variables are shown just below the depiction of the plasma source in Figure 3.11. The variable L_s represents the cavity length and is defined as extending from the sliding short to the bottom of the microwave cavity. L_p is the length of the adjustable loop antenna extending from the sliding short to the tip of the loop. L' is the section of empty waveguide extending from the tip of the loop to the quartz dome of the plasma discharge. L_e is the

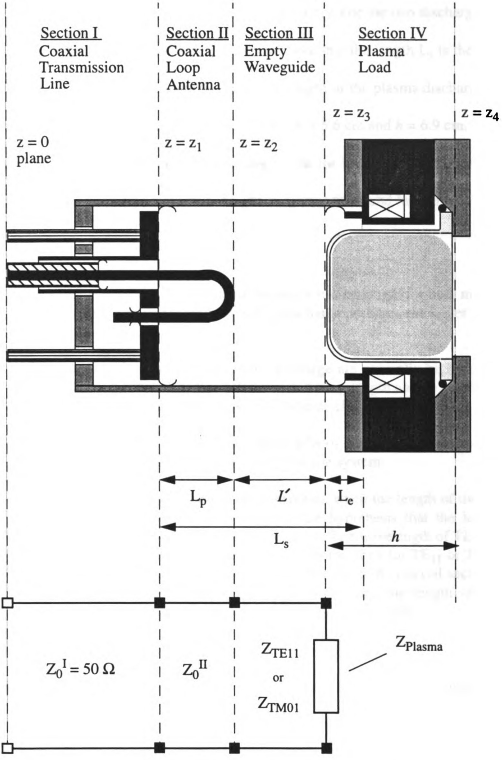

Figure 6.1 - Four Sections of the Plasma Source and Transmission Line Equivalent Circuit

extension of the quartz discharge chamber into the cavity, defined as the distance from the top of the discharge chamber to the bottom of the cavity. For the two discharge chambers used in this thesis L_e = 1.4 cm and L_e = 2.7 cm. Note that the length L_s is the sum of the lengths L_p, L', and L_e. The variable h is the total height of the plasma discharge chamber. For the two discharge chambers used in this thesis h = 5.6 cm and h = 6.9 cm.

Specific observations of the cavity tuning length for both modes under variations of discharge pressure, discharge chamber height, magnetic field, and loop antenna length are given below:

- As discharge pressure is increased the cavity tuning length for both modes generally increases. The larger the increase in discharge pressure, the larger the increase in cavity tuning length.

- Cavity tuning lengths for the 6.9 cm discharge are generally higher than for the 5.6 cm discharge, however the difference in tuning length can be smaller or larger than the 1.3 cm difference in the height of the discharge.

- Very little change in the cavity tuning lengths of both modes was observed when the multipole magnet ring was removed from the system.

- Cavity tuning length for both modes increases when the length of the adjustable loop antenna is decreased. This supports the hypothesis that the loop antenna forms a coaxial section at one end of the cavity. The wavelength of TEM propagation in a coaxial waveguide section is much shorter than for TE_{11} or TM_{01} modes in an empty 9.8 cm diameter waveguide. Thus, when the coaxial section is made shorter by decreasing the length of the loop antenna the length of the empty waveguide section must show a larger increase to compensate.

The transmission line model can be used to explain the observed tuning behavior of the plasma source noted above. Changes in discharge pressure and discharge chamber height change the complex impedance of the plasma load and therefore require a change in length of the transmission line sections (section II ~ L_p or section III ~ L') in order to maintain the conditions for resonance. When discharge pressure and discharge height are held constant a change in L_p will require a compensating change in L' to maintain the conditions for resonance.

6.3 Recommendations for Future Research:

For all experiments in this thesis the input power was held constant at 150 Watts. Plasma properties such as charge density are greatly effected by changes in input power, thus behavior of the plasma source could be much different for input power levels above and below 150 Watts. Any future investigation of this source should include observations of output variables for variation in input power. A variation from 50 Watts to 250 Watts would be a useful range to investigate.

Variation in the flow rate of the discharge gas may also cause a change in the behavior of the plasma source. Therefore, evaluation of this source on a vacuum system where pressure and flow rate can be independently varied may also provide a more complete description of source behavior.

In this thesis an end fed adjustable loop antenna was used to couple micorwaves into the 9.8 cm diameter cavity applicator. For this applicator other types of microwave coupling should be investigated, such as: end fed probe coupling and side fed probe coupling. Smaller diameter applicators that only propagate the TE_{11} waveguide mode should also be investigated with: adjustable end feed loop coupling, end feed probe coupling, and side feed probe coupling.

The primary unanswered question in this thesis is the origin of the Low L_s mode.

Future investigation should be directed at understanding what causes this phenomenon. A primary tool in this investigation will be the detailed measurement of electric field mode patterns and absolute electric field strength. Very sensitive electric field measurement techniques may be needed to determine the field patterns of the Low L_s mode. Absolute electric field strength measurements will also be valuable in assessing the electromagnetic losses in the walls of the cavity applicator and losses in the discharge.

Other experimental measurements that have yet to be performed on this plasma source are: single Langmuir probe electron energy distribution measurements, ion energy analysis, measurement of plasma potential, and measurement of radical flux with a quartz crystal microbalance.

An objective in all MPDR research is to develop a working physical model encompassing both electromagnetic and plasma theory that accurately predicts (qualitatively and quantitatively) the behavior of compact and larger diameter microwave plasma disk reactor designs. Development and testing of the physical model should involve computer simulation of the plasma sources investigated using the proposed model. A fully developed physical model would aid in the operation and control of present microwave plasma systems and also serve as a guide in the design of new microwave plasma sources with improved performance characteristics.

The research presented in this thesis was intended to contribute to this goal of a predictive physical model, however much more investigation will be required to develop and verify a reliable theoretical model.

LIST OF REFERENCES

REFERENCES

[1] O. A. Popov, "Electron Cyclotron Resonance Plasma Sources and Their Use in Plasma-Assisted Chemical Vapor Deposition of Thin Films", Academic Press (1994).

[2] B.Lax, W. P. Allis, and S. C. Brown, J. Appl. Phys. 21, 1297 (1950).

[3] K. Suzuki, S. Okudaira, N. Sakudo and I. Kanomata, Japan. J. Appl. Phys., Vol. 16, No.11, 1979 (1977).

[4] S. Matsuo and M. Kiuchi, Japan. J. Appl. Phys., Vol. 22, No. 4, L210 (1983).

[5] J. Asmussen and J. Root, Appl. Phys. Lett., 44(4), 396, (1984).

[6] Root, J. and Asmussen, J. Rev. Sci. Instrum., 56:1511, (1985).

[7] M. Dahimene, Development of a Microwave Ion and Plasma Source Immersed in a Multicusp Electron Cyclotron Resonant Magnetic Field, Ph.D thesis, Michigan State University, (1987).

[8] J. Asmussen, J. Root, "Ion Generation Apparatus and Method for the Use Thereof", US patent No. 4507588 (March 1985).

[9] Asmussen, J. and Root, J. , U.S. Patent No. 4,507,588 (26 March 1985).

[10] Asmussen, J. and Reinhard, D.K. U.S. Patent No. 4,585,688 (29 April 1986).

[11] Asmussen, J. and Reinhard, D.K. U.S. Patent No. 4,630,566 (23 Dec. 1986).

[12] Roppel, T.A. Asmussen, J., and Reinhard, D.K., U.S. Patent No. 4,691,622 (8 Sept.1987).

[13] Asmussen, J. , Reinhard, D.K., and Dahimene, M., U.S. Patent No. 4,727,239 (23 Feb. 1988).

[14] Asmussen, J. and Hopwood, J. , U.S. Patent No. 5,081,398 (14 Jan. 1992).

[15] Asmussen, J., U.S. Patent No. 4,906,900 (6 March 1990).

[16] J. Hopwood, Macroscopic Properties of a Multipolar Electron Cyclotron Resonance Microwave-Cavity Plasma Source for Anisotropic Silicon Etching, Ph.D thesis, Michigan State University, (1990).

[17] F. C. Sze, Design and Experimental Investigation of a Large Diameter Electron Cyclotron Resonant Plasma Source, Ph.D. thesis, Michigan State University, (1993).

[18] A. K. Srivastava, Properties of Electron Cyclotron Resonance Plasma Sources, Ph.D thesis, Michigan State University, (1995).

[19] S. J. Whitehair, Experimental Development of a Microwave Electrothermal Thruster, Ph.D thesis, Michigan State University, (1986).

[20] L. Mahoney, The Design and Testing of a Compact Electron Cyclotron Resonant Microwave-Cavity Source, M.S. thesis, Michigan State University, (1989).

[21] A. K. Srivastava, J. Asmussen, T. Antaya, and K. Harrison, "The Study of a 2.45 GHz Plasma Source as a Plasma Generator for the SCECR Electron Cyclotron Resonance Ion Source", Rev. Sci. Instrum. 65 (4), April (1994).

[22] A.B. Bronwell, R.E. Beam, Theory and Application of Microwaves, p. 340, McGraw-Hill, (1947).

[23] D.K. Cheng, Field and Wave Electromagnetics, pp. 568-570, Addison-Wesley, (1989).

[24] M. Siegel, B. Wright, "Computerized Mapping of the Electromagnetic Modes of Empty and Dielectric Loaded Single Mode Cavities", private communications.

[25] P. Mak, "Evaluation of an end excited electron cyclotron resonance plasma source", Procedings of the 1994 IEEE Intl. Conf. on Plasma Science, p. 85, (1994).

[26] R. H. Huddlestone, S. L. Leonard, Plasma Diagnostic Techniques, Ch. 4 written by F.F. Chen, Academic Press, New York, (1965).

[27] S. Ramo, J.R. Whinnery, T. VanDuzer, Fields and Waves in Communication Electronics, table 8.09 p. 444, John Wiley & Sons, New York, (1965).